ABSTRACT

Title of Dissertation: SOLUTION PROCESSING OF LONG CARBON NANOTUBES: FROM FUNDAMENTALS TO APPLICATIONS

Peng Wang, Doctor of Philosophy, 2019

Dissertation directed by: Professor YuHuang Wang
Department of Chemistry and Biochemistry

Single-walled carbon nanotubes (SWCNTs) are one of the most intensively studied nanomaterials due to their extraordinary mechanical, electrical, and optical properties. Attaining aqueous solutions of individual SWCNTs is the critical first step for harnessing their outstanding properties and applying them in many applications and further processing, such as sorting, imaging, and sensing. However, the current ultrasonication-then-ultracentrifugation approach inevitably introduces defects to SWCNTs and cuts the nanotubes into smaller pieces, compromising the electrical and mechanical properties of this otherwise remarkable material.

In this dissertation, we introduce an unexpectedly simple approach that completely eliminates the need for ultrasonication, and nondestructively disperses SWCNTs in aqueous solution, so that the synthetic lengths of SWCNTs can be

preserved. The dispersion is achieved by using surfactants to wrap and stabilize the protonated SWCNTs by simple acid-base neutralization reactions. The result is that the protons on SWCNTs are replaced by surfactants, and thus, we name this method "superacid-surfactant exchange (S2E)." In chapters 2-4, we demonstrate the length of dissolved SWCNTs by S2E can be 4-10 times longer than the sonicated controls, thereby significantly improving the optical, electrical and electromechanical properties. We further find that by tuning the concentrations of SWCNTs in this S2E process, short nanotubes can be selectively extracted out, allowing separation of the long carbon nanotubes (>10 μm).

In chapter 5, we show that long SWCNTs can behave like mechanical reinforcing structures that enhance the mechanical strength of graphene through π-π interactions without sacrificing much of the outstanding transparency of graphene. This fact has enabled the fabrication of the mechanically strong yet ultrathin graphene/SWCNTs hybrid structure (G+T) for *operando* probing of the electrical double layer at the electrode-electrolyte interface by X-ray photoelectron. Finally, as a ramification result from the S2E process, chapter 6 describes the scalable synthesis of organic-color-center tailored SWCNTs.

SOLUTION PROCESSING OF LONG CARBON NANOTUBES: FROM FUNDAMENTALS TO APPLICATIONS

by

Peng Wang

Dissertation submitted to the Faculty of the Graduate School of the
University of Maryland, College Park, in partial fulfillment
of the requirements for the degree of
Doctor of Philosophy
2019

Thesis Committee:
Professor YuHuang Wang, Advisor and Committee Chair
Professor Bryan W. Eichhorn
Professor Sang Bok Lee
Dr. Ming Zheng (National Institute of Standards and Technology)
Professor John Cummings, Dean's Representative

Acknowledgments

First, I want to express my deepest gratitude and appreciation to my mentor, Prof. YuHuang Wang, for the opportunity to work on some of the most fundamentally important problems in the field of carbon materials. I gratefully thank him for his numerous advice and guiding me in my scientific research. His enthusiasm, his fearlessness, and his working ethics will inspire me throughout my career and life. Joining Wang's group is one of the best decisions that I have ever made!

My thanks also go to my dissertation committee: Prof. Bryan Eichhorn for relentless supports and encouragements on the graphene window project; Prof. Ming Zheng for his valuable suggestions on the carbon nanotube chirality sorting; Prof. Sang Bok Lee, Prof. John Cumings for their classroom instructions on electrochemistry, electron microscopy respectively, and also for their interests in my research.

I am lucky to work with a group of highly talented and motivated colleagues. I can never achieve this far without their supports. Particularly I thank Dr. Mijin Kim for developing the superacid-surfactant exchange method together with me. It is Mijin who first discovered the photoluminescence of the aqueous surfactant solution after quenching the superacid-carbon nanotube mixture, which made us realize that a simple solution quenching can lead to nondestructive dissolution of carbon nanotubes, a method that researches had been seeking for decades. I thank Dr. Zhiwei Peng and Muxiao Li for separating metallic double-walled carbon nanotubes by density gradient ultracentrifugation. I thank Dr. Karen Gaskell for modifying her XPS chamber for the *operando* XPS measurement; Yunfeng Li for fabricating the robust yet transparent

graphene/nanotube hybrid membrane; Ben Barns for his contributions in e-beam lithography and electrode design; and Hongbin Luo for the collaborations on the functionalization of carbon nanotubes in the superacid media.

I would like to express my appreciation to Prof. Matteo Pasquali and Dr. Robert Headrick from Rice University for the collaboration on ultralong nanotube self-sorting. Prof. Daniel Blankschtein and Dr. Satish Kumar Iyemperumal from MIT for their splendid theoretical modeling. I also thank Dr. Jacek Kłos, Dr. Fu Chen, Dr. Chuanfu Sun, Dr. Chienfu Chen, Dr. Allen Ng, Dr. Xiaojian Wu, Dr. Beibei Xu, Dr. Zhongjie Huang, Dr. Mirihiro Okada, Dr. Shunliu Deng, Jacob Fortner, Nam Kim, Xiyuan Cheng, Haoran Qu, Chiyu Zhang, with whom I have helpful discussions and fruitful collaborations.

I would also like to thank all the funding agencies that have support our researches, including the National Science Foundation (NSF, through award number CHE-1507974 and CHE1626288), National Institute of Health (NIH, through award number R01GM114167), Air Force Office of Scientific Research (AFOSR, through award number FA9550-16-1-0150), Department of Energy (DOE), Energy Frontier Research Center (EFRC, through award number DESC0001160) and Millard and Lee Alexander Fellowship from the University of Maryland.

Finally, my gratitude goes to my family, especially to my wife Ziwei Ouyang. I am truly blessed to meet you. You made me realize that the world outside the lab is such a wonderful place filled with happiness. I can never be this far without your love, sacrifices, and supports.

Table of Contents

List of Figures

List of Abbreviations

S2E: Superacid-Surfactant Exchange
1D: One-dimensional
SWCNT: Single-walled carbon nanotube
DWCNT: Double-walled carbon nanotube
MWCNT: Multi-walled carbon nanotube
PL: Photoluminescence
EL: Electroluminescence
LED: Light Emitting Diode
TFT: Thin Film Transistor
UV: Ultraviolet
vis: Visible
NIR: Near-infrared
DOC: Sodium deoxycholate
SC: Sodium cholate
SDS: Sodium dodecyl sulfate
DNA: Deoxyribonucleic acid
CTAB: Cetrimonium bromide
ATP: Polymer aqueous two-phase separation
DGU: Density Gradient Ultracentrifuge
AFM: Atomic Force Microscopy
SEM: Scanning Electron Microscopy
TEM: Transmission Electron Microscopy
ITO: Indium Tin Oxide
STCF: Stretchable Transparent Conductive Film
PDMS: Polydimethylsiloxane
EDL: Electrical Double Layer
XPS: X-ray Photoelectron Spectroscopy
AAO: Anodic Aluminum Oxide
MD: Molecular Dynamics
OCC: Organic Color Center

1. Introduction

1.1. The Scope of this Thesis

On the single molecular level, single-walled carbon nanotubes (SWCNTs) exhibit extraordinary electrical, mechanical, and optical properties. However, translating these exceptional properties that measured on an individual tube to a macroscopic SWCNTs-based object is still an unmet dream. Among various factors that deteriorate the collective properties of SWCNTs, limited nanotube length is foremost. Individually dissolving SWCNTs in aqueous solution is usually the critical first step for harnessing their extraordinary properties for a broad range of applications. However, the most widely used approach of sonication followed by the ultracentrifugation causes structural damage and cuts the nanotubes into short pieces. As a result, macroscopic objects and devices that are composed of short SWCNTs usually exhibit undesirable properties, such as high sheet resistances, limited carrier mobilities, and low mechanical strength. This thesis is mainly focused on how to preserve the synthetic length of SWCNTs in aqueous solution and characterizing the outstanding properties of these long SWCNTs in terms of the device performances.

Chapter 1 reviews the physical structures, properties and major applications of the SWCNTs materials. The current problems and challenges in the field of SWCNTs research are also summarized. In Chapter 2, I describe the superacid-surfactant exchange (S2E) method we developed in our lab that can non-destructively dissolve carbon nanotubes in aqueous solution without the aid of ultrasonication. Due to the elimination of sonication during the S2E process, the dispersed nanotubes are significantly longer (4-10 times) with lower defect densities compared to the sonicated

controls. They also feature an 8-fold improvement in electrical conductivity and more than 90% brighter photoluminescence. Chapter 3 shows that by utilizing the equilibrium between the nematic and isotropic phase behaviors of SWCNTs in superacid, we can iteratively remove the short SWCNTs and selectively enrich ultralong SWCNTs with lengths exceeding 10 μm. Thin-film-transistors fabricated from ultralong semiconducting SWCNTs exhibit excellent on-off ratios higher than ~1000 and carrier mobilities reaching 90 $cm^2 \cdot V^{-1} \cdot s^{-1}$, approaching that of polycrystalline silicon, which is one of the most widely used semiconductors. Chapter 4 describes the extraordinary electromechanical properties of long metallic nanotubes. Long metallic double-walled carbon nanotubes can simultaneously attain ultrahigh electrical conductivity, mechanical stretchability, and optical transparency, all of which are necessary for achieving high-performance stretchable transparent conductive films. Chapter 5 shows that by spin coating a thin layer of long SWCNTs on graphene, we can fabricate a mechanically strong and optically transparent hybrid thin membrane up to the centimeters-scale area. This membrane can be integrated into an electrical liquid cell as a transparent, yet conductive, electrode that had enabled us to directly visualize the formation of the electrical double layer nanostructures at the electrode-electrolyte interface. Chapter 6 describes some "ramification" projects we did that are interestingly connected to the concept of the S2E. We show that large scale synthesis of organic-color-center tailored SWCNTs (OCC-SWCNTs) can be achieved by simply quenching the superacid-SWCNTs solution with water in the presence of reactant molecules.

In conclusion, we demonstrated that SWCNTs can be non-destructively dispersed in aqueous solutions with their initial synthetic length preserved. These long

tubes are not only valuable to fundamental studies but also have great potential to further improve the performance of SWCNT-based devices and facilitate researches in the fields of energy, electronics, and photonics.

1.2. Physical Structure, Properties and Applications of Carbon Nanotubes

A carbon nanotube (CNT) is a cylindrically shaped carbon allotrope with an ultrahigh aspect ratio up to 10^7 (ref. 1). The structure of a carbon nanotube can be viewed as a sheet of graphene rolled into a seamless carbon cylinder.[2] Based on the number of graphene sheets rolling up, CNTs can be categorized into single-walled carbon nanotubes (SWCNTs), double-walled carbon nanotubes (DWCNTs) and multi-walled carbon nanotubes (MWCNTs; Figure 1-1).[2] This dissertation will only discuss the SWCNTs and DWCNTs since they are the two types of CNT materials mainly used in my Ph.D. research.

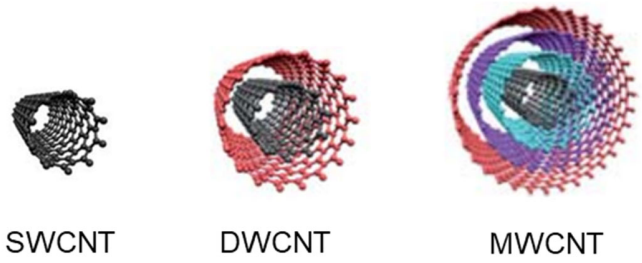

Figure 1-1. Schematics of single-walled carbon nanotube (SWCNT), double-walled carbon nanotube (DWCNT) and multi-walled carbon nanotube (MWCNT). Figure is adapted from ref. 3.

A piece of graphene sheet can be rolled up in a variety of ways and, as a result, the structure of the resulting SWCNT can be different. The unique structure of a SWCNT can be described by a pair of chiral vectors (n,m) that define the roll-up vector (C_h)

$$\overrightarrow{C_h} = n\overrightarrow{a_1} + m\overrightarrow{a_2}$$

where *n* and *m* are both positive integers; a_1 and a_2 are the unit vectors in the lattice of a graphene sheet (Figure 1-2).[4] This nomenclature is very informative as one can directly predict the optical and electrical properties of SWCNTs by their chiral vectors: the SWCNTs will be metallic in nature if (*n*-*m*)/3 is an integer, otherwise the SWCNTs will behave like semiconductors. High-symmetry SWCNTs with (*n*,*n*) and (*n*,0) are named as armchair and zigzag SWCNTs, respectively. Also, the diameter (*d*) of a given SWCNT can be calculated by equation 1:

$$d = 78.3 \times \sqrt{(n+m)^2 - nm}\ \text{pm} \qquad \text{eq.1}$$

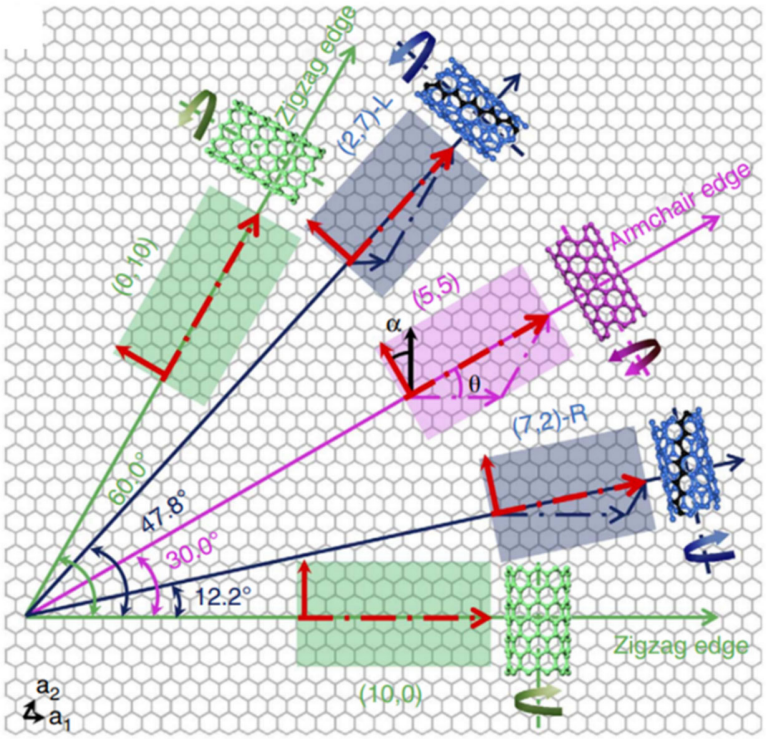

Figure 1-2. Mapping SWCNT chiral indices (*n*,*m*) on a piece of graphene sheet. Depending on the direction of rolling with respect to the graphene lattice, the resulting SWCNTs can be chiral, zigzag or armchair. Figure is adapted from ref. 4.

The unique structure of SWCNT give rise to a combination of extraordinary electrical,[5-9] optical,[10-12] and mechanical[2, 13-15] properties.

The one-dimensional (1-D) structure of a SWCNT significantly reduces phonon scattering in its lattice, therefore extremely high carrier mobilities are possible even at room temperature.[2] For example, an individual metallic SWCNT (m-SWCNT) can exhibit ballistic conductance at room temperature with a resistance of ~1 μΩ/cm, which exceeds that of copper.[5, 8] Thanks to their extraordinary electrical conductivity, SWCNTs have also been used as the transparent conductive films as an alternative to the conventional indium tin oxide (ITO), to meet the growing demand for displays, touch-screen devices and photovoltaics. Also, the flexibility of SWCNT transparent conductor is a major advantage over the brittle ITO for flexible display applications. Semiconducting SWCNTs also display ballistic conductance in room temperature. The charge-carrier mobility of an individual semiconducting SWCNT (sc-SWCNT) can be as high as 79000 $cm^2 \cdot V^{-1} \cdot s^{-1}$.[9, 16] (Figure 1-3a) Accordingly, sc-SWCNTs have been demonstrated as an ideal channel material for the application of the high-performance field-effect transistors (FETs). Nevertheless, when the FET is fabricated using a sc-SWCNT percolative thin film, the mobility decreases significantly below ~100 $cm^2 \cdot V^{-1} \cdot s^{-1}$ due to the carrier scattering at the junctions between different sc-SWCNTs.[17, 18]

The optical properties of SWCNTs were not investigated until Smalley and co-workers discovered the optical and fluorescence spectra of SWCNTs in 2002.[11] The unique optical properties of SWCNTs originates from the van Hove singularities in the nanotube density of states. The formation and subsequent behavior of excitons , which are essentially excited electron-hole pairs that originate from the strong Coulomb interaction in 1-D SWCNTs structure, is one of the most fundamental and interesting optical properties of SWCNTs.[12] An exciton can be generated either optically or electrically, which gives rise to the photoluminescence (PL) and electroluminescence (EL, Figure 1-3b)[19] respectively. Accordingly, SWCNTs have been demonstrated to be the promising candidates for optoelectronic applications including solar cells, light emitting diodes (LEDs) and photodetectors (Figure 1-3c).[20] Additionally, certain types of sc-SWCNTs can photoluminesce beyond the wavelength of 1000 nm and have been demonstrated by Dai and co-workers as promising fluorescent contrast agents for bioimaging applications (Figure 1-3d) owing to the reduced photon scatterings and deep tissue penetration depth.[21, 22]

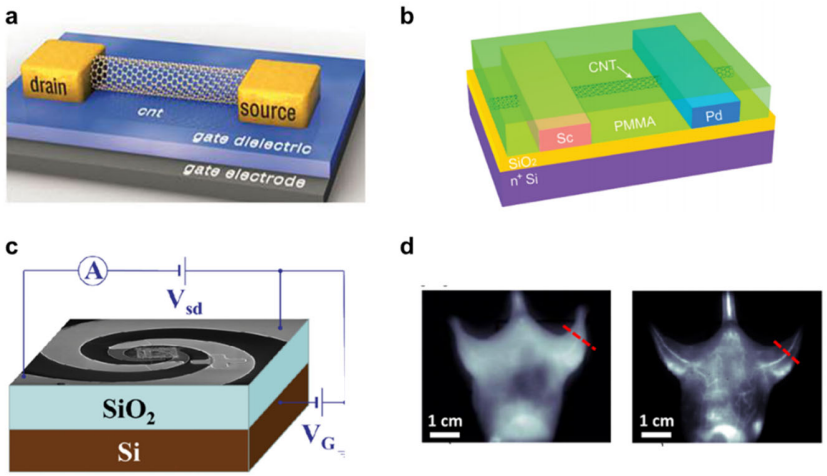

Figure 1-3. Illustrations of SWCNTs applications in the fields of microelectronics, optoelectronics and bioimaging. (a) A FET based on an individual semiconducting SWCNT.[9] (b) An EL device fabricated from an individual semiconducting SWCNT.[19] (c) A SWCNT-based terahertz photodetector.[20] (d) Fluorescence images of a mouse injected with NIR-I dye that emit at a wavelength of 800 nm (left) and with NIR-II SWCNTs that emit at wavelength above 1000 nm (right).[21] The NIR-II window allows visualization of the blood vessels with much higher resolution. Figures are adapted from ref. 9, 19, 20 and 21, respectively.

Mechanically, because of the uniform crystalline structure and high strength of C-C bond, a defect free individual SWCNT is regarded as one of the strongest materials in the world and exhibits ultrahigh tensile strength of ~13-100 Gpa[14, 15] and an average Young's modulus of ~1TPa.[13] SWCNTs can be assembled into a macroscale aligned SWCNTs fibers and reach a tensile strength up to ~9.6 Gpa.[23] Due to such extraordinary mechanical properties, SWCNTs have also been widely used as fillers for polymer and resins to increase the stiffness, strength and toughness. For example, only ~1 wt % SWCNT in the epoxy resin can enhance the resulting composite stiffness and fracture toughness of by 6% and 23%.

1.3. The Critical Role of Carbon Nanotube Length and the Effect of Sonication Cutting

Promising as they are, however, such extraordinary properties only exist on an individual SWCNT level and will be largely compromised on an ensembled level. How to create macroscopic objects by assembling nanotubes while preserving their extraordinary properties is still a grand obstacle in front of the community. Among the various issues to be solved, the limited length of SWCNTs as the building blocks for the macroscale objects is one of the most critical.

The length of SWCNTs plays an important role in governing the properties of SWCNTs and the SWCNT-based macroscale objects and devices: long SWCNTs are usually desirable for electrical, mechanical, and optical applications. For electronic applications, short nanotubes form more tube-tube junctions than long nanotubes when assembled into random macroscale networks, consequently resulting in limited percolating pathways, high sheet resistance, low on-currents, and low mobility in TFTs.[24] The mechanical properties of macroscale aligned objects are determined by inter-nanotube friction, which scales with CNT length and limits the tensile strength far below that of an individual tube.[25,26] Additionally, short nanotubes usually fluoresce less brightly than long nanotubes due to the quenching of excitons at the nanotube ends.[27] In the extreme scenarios, unfunctionalized ultrashort nanotubes with lengths of less than ~100 nm completely loss their intrinsic fluorescence.[28]

Recent breakthroughs in synthetic methods have made the raw SWCNT materials with the length exceeding 10 μm commercially available. However, such

long lengths are extremely hard to preserve during the post-synthesis processes mainly due to the use of ultrasonication as the first step to dissolve SWCNTs.

Ultrasonication inevitably damages SWCNTs, creating defects in tube lattices and cutting them into short pieces.[29, 30] Therefore, after this heavy sonication step, the average length of SWCNTs is usually less than 1 μm and considerable numbers of tubes less are shorter than 500 nm. This short average tube length poses a severe disadvantage in further using them for macroscale applications since short tubes usually feature low electrical conductivity, mechanical strength, and photoluminescence.

Theoretical modeling indicates that the cutting mechanisms is different for SWCNTs of different lengths.[30] Ultrasonication creates air bubbles in the solution and during the bubble growth, short nanotubes tend to align radially along the bubble surface while the long nanotubes remain tangentially and buckled. The collapse of the air bubble exerts strain on the SWCNTs and cause them to break following a power law

$$L \propto t^{-m}$$

where *L, t* and *m* are the length decay of SWCNTs, sonication time and length-dependent scaling factor, respectively. Theoretical modeling indicates that short nanotubes decay by a power law of $m = 0.41$-0.5, while long tubes decay by $m = 0.205$-0.25 (Figure 1-4). These modeling results are corroborated by the experimental results.[31] Therefore, long tubes are more easily cut into short fragments, making the usage of sonication highly undesirable for individually dissolving long tubes.

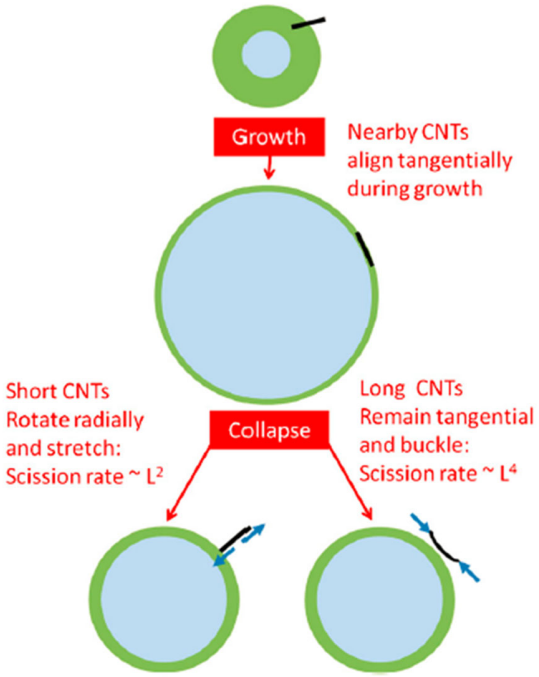

Figure 1-4. Schematic illustrations of breakage of CNTs under sonication.[31] CNTs near the bubble nucleus (green) align tangentially during bubble growth (blue). During collapse, CNTs may rotate radially and stretch or buckle depending on their length. Figure is adapted from ref. 31.

1.4. Solution Processing of Carbon Nanotubes

Individual dispersal in certain solvent is usually the first step to sort SWCNTs by their structures and building SWCNT-based macroscopic objects. Although covalent side wall functionalization can imbue SWCNTs with high solubility in aqueous or organic solutions, the functionalization always destroys the outstanding electronic and optical properties of SWCNTs, and thus will not be discussed.[32, 33]

1.4.1. Dispersion and Sorting of Carbon Nanotubes in Water and Organic Solvent

Alternatively, non-covalent surfactant or polymer wrapping of the exterior sidewall has been proven to be the most successful route to disperse SWCNTs while maintaining most of their attractive properties. To disperse SWCNTs in water or organic solvent like toluene, ultrasonication is usually required to overcome the strong Van de Waals interactions between nanotubes such that individual SWCNTs can be wrapped by either DNA, surfactant molecules or polymers.

SWCNTs can be individually dispersed in aqueous solution by the wrapping of different molecules such as single strand DNA, sodium dodecyl sulfate (SDS), sodium cholate (SC) and sodium deoxycholate (DOC).[34, 35] Since SWCNTs of different types feature different electron density and tube curvatures, their affinities with surfactants are different. Such subtle difference lead to variances of surfactant micelle coverage around SWCNTs and becomes the basis for the SWCNTs sorting techniques including gel column chromatography,[36, 37] density gradient ultracentrifugation (DGU)[38, 39] and aqueous two-phase extraction (ATPE)[40-43].

Gel column chromatography consists of a mobile sample solution that moves downward through a column filled with gels.[36] Due to the different size, charge density, and many other parameters from different particles, their travel speed is different. Therefore, by carefully tuning the composition of cosurfactants (such as molar ratio between SDS and SC surfactants), SWCNTs of different types can be eluted sequentially and get separated (Figure 1-5a). A large-scale, single chirality SWCNTs separation by the gel column chromatography was first demonstrated by the Kataura group in 2011.[37]

DGU based SWCNTs sorting relies on SWCNTs' different buoyant densities.[39] By mixing SWCNTs with density gradient media, the SWCNTs will migrate to different layers whose density matches the SWCNTs buoyant density under strong centrifugal force. DGU was first demonstrated by Hersam and co-workers to achieve metallic and semiconducting SWCNTs separation in 2006.[39] Shortly after in 2010, by engaging a non-linear density gradient media, up to ten chiralities of SWCNTs were successfully separated in a single step by Weisman and co-workers (Figure 1-5b).[38]

ATPE was firstly reported by Zheng and co-workers.[43] A general ATPE system is composed of two water soluble polymers such as polyethylene glycol (PEG) and dextran. Above certain a concentration threshold (usually ~7% by weight percent), these two polymers spontaneously form two immiscible phases: the top phase is mainly composed of PEG polymer, and is more hydrophilic, while the bottom phase is composed of dextran polymer, and more hydrophobic (Figure 1-5c). On the other hand, SWCNTs with different coverage of surfactant micelles, which is based on their chirality, feature slightly different hydrophilicity and tend to partition into the phase

that match. Therefore, by iterative adjusting the surfactants in the solution, single chirality enrichment can be achieved. ATPE is easy to handle and can achieve single chirality nanotube separation in a short time (few minutes to tens of minutes).[40, 41] Also, it does not require expensive facilities and special instruments.

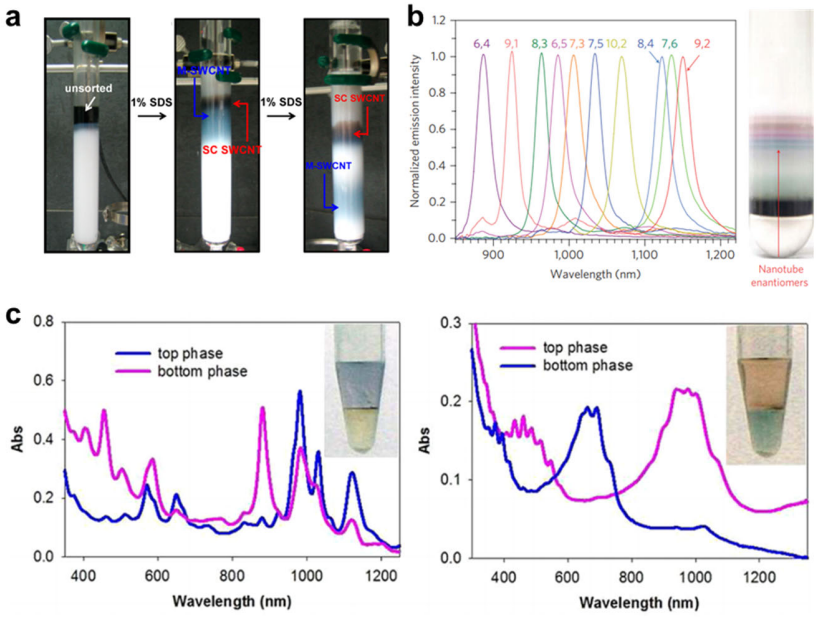

Figure 1-5. Sorting surfactants-stabilized SWCNTs into chirality enriched portions in aqueous solutions. (a) Sorting SDS and SC dispersed SWCNTs via gel column chromatography.[36] (b) Sorting of DOC dispersed SWCNTs into single chirality via nonlinear DGU.[38] (c) Sorting SC dispersed SWCNTs with different diameters (left: SWCNTs with smaller diameters; right: SWCNTs with larger diameters) via ATPE.[43] . Figures are adapted from ref. 36, 38 and 43, respectively.

Polymer wrapping is an alternative approach that has been successfully demonstrated to dissolve and sort SWCNTs. DNA and π-conjugated polymers are the two major polymers commonly used.

First demonstrated by Zheng and co-workers, DNA of specific sequence can wrap around SWCNTs of particular chirality to form DNA-SWCNTs hybrid structures with different surface charge densities (Figure 1-6a).[44, 45] Such DNA-SWCNTs hybrids can be further separated by either gel column chromatography,[45] DGU[46] or ATPE[40] methods. One of the biggest advantages for DNA based sorting is that DNA with any specific sequence can be designed and synthesized. Therefore, it offers an effectively infinite number of possibilities to form DNA-SWCNTs hybrid structures. So far, certain SWCNT chiralities such as (10,0) and (11,0) are only separated by DNA-based sorting techniques.[40] However, a main problem with this method is the high cost for DNA synthesis, which limits its applications to small scale practices.

Semi-flexible conjugated polymers have been used to dissolve and sort SWCNTs in organic solvents such as toluene or chloroform (Figure 1-6b). As first introduced by Nish and co-workers,[47, 48] a number of conjugated polymers (mainly based on polyfluorene derivatives) have been explored to sort SWCNTs with specific types. Simplicity is one of the advantages of this polymer dissolution and sorting method. Researchers just need to sonicate the SWCNTs together with a specific polymer and centrifuge to remove the undissolved bundles. The supernatant is enriched with certain diameter or chirality, depending on the chosen polymer. Nevertheless, once the polymers wrap the SWCNTs, they are generally hard to remove due to the

strong π-π interactions, causing problems in the subsequent SWCNT-based device fabrication process and reducing the device performances.[49]

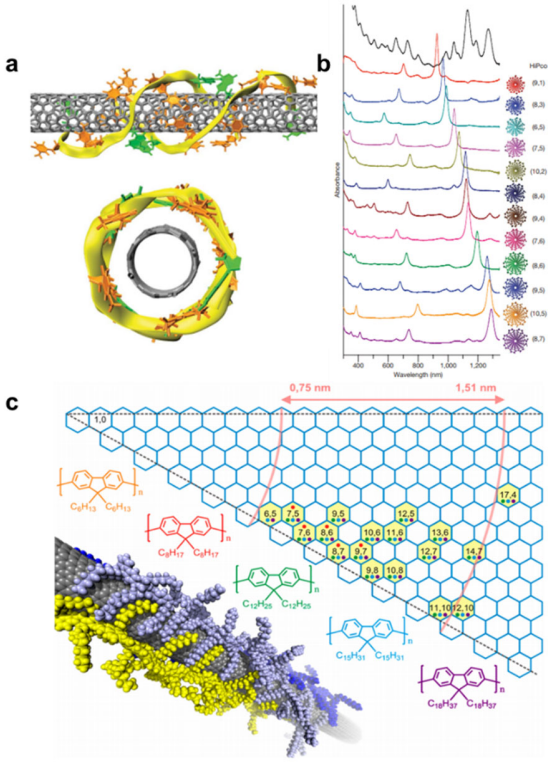

Figure 1-6. Sorting polymer-stabilized SWCNTs. (a) Molecular simulation of a DNA wrapped SWCNT.[45] (b) Absorption spectra of sorted single-chirality enriched SWCNTs by DNA recognition. (c) Chirality map of polyfluorene-wrapped SWCNTs, chemical structure of polyfluorene derivatives and the structure of SWCNT-polymer hybrids obtained from molecular dynamics simulations.[48]. Figures are adapted from ref. 45 and 48, respectively.

1.4.2. Dispersion of Carbon Nanotubes in Chlorosulfonic Acid

Although SWCNTs are difficult to dissolve in aqueous solution, Pasquali and co-workers have found that SWCNTs can spontaneously dissolve in chlorosulfonic acid (superacid) by the surface protonation effect.[50, 51] The superacid protonates the sidewall of SWCNTs, which can be described by the following equation:

$$(CNT)_{bundled} + H^+ \leftrightarrow (CNT)_{individual}H^+$$

Once the SWCNTs are protonated, the positive charges on SWCNTs are delocalized and can migrate freely along the SWCNTs surfaces. Comparing with dissolving SWCNTs in aqueous or organic solutions, SWCNTs can be dissolved in superacid at a concentration up to ~45 mg/mL to form an optically homogenous solution, which is ~1000 times higher than the SWCNTs concentration in aqueous solution.[50] Pasquali and co-workers have also demonstrated that the positive charge per carbon can be monitored by the shift of Raman G-peak after dissolving SWCNTs in superacid media.[51] In resonance Raman Spectroscopy, the D peak of carbon materials, occurring at ~1350 cm^{-1}, arises from structural defects (e.g., atomic vacancies or sp^3 hybridized bonds). Meanwhile, the G peak (~1590 cm^{-1}) corresponds to sp^2 bond stretching. The charge per carbon for SWCNTs fully dissolved in superacid is ~0.078. It is important to note that the protonation of SWCNTs sidewalls does not introduce any functionalization, as evidenced by the identical D/G ratio (intensity of D peak to G peak, directly correlating with the density of defects within the carbon lattice) after the acids have been quenched away. Therefore, the superacid is considered as the only "true" solvent to dissolve the SWCNTs materials.[51]

The discovery of this true solvent has led to the fabrication of high-quality SWCNT fibers[26, 50, 52] and thin films.[53] The state-of-art highly aligned SWCNT-fibers

can simultaneously reach an extraordinary conductivity of 8.5 $MS \cdot m^{-1}$ and a tensile strength over ~2.4 Gpa.[52]

Although the superacid solvent can nondestructively disperse SWCNTs with their synthetic length preserved, the fact that the superacid is highly acidic (its acidity is even higher than that of the oleum), corrosive and reactive[54] prevent its usage in wider a range of applications such as in biological systems. Moreover, up to date, no SWCNTs chirality sorting methods have ever been demonstrated in the superacid.

In a nutshell, a method that can disperse SWCNTs in their full-length and allows further chirality separation is highly needed.

2. Nondestructive Dispersion of Full-Length Carbon Nanotubes in Water by Superacid-Surfactant Exchange

This chapter is adapted from a published manuscript:[55]

Wang, P.; Kim, M.; Peng, Z.; Sun, C.; Mok, J.; Lieberman, A.; Wang, Y. *ACS Nano*. **2017**, 11, 9231.

P.W. and M.K. contributed equally to this work. Y.W., P.W., and M.K. conceived and designed the experiments. P.W., M.K., C.S., J.M., and A.L. performed the experiments. Z.P. performed the TEM characterization. Y.W., P.W., and M.K. wrote the manuscript with inputs from all authors.

This work was partially supported by NSF (CHE-1507974), NIH/NIGMS (R01GM114167), and AFOSR (MURI FA9550-16-1-0150). We also gratefully acknowledge the DOE Advanced Research Projects Agency−Energy (DEAR0000527) for partial support of the solution processing. P.W. and C.S. are partially supported by the Nanostructures for Electrical Energy Storage (NEES), an Energy Frontier Research Center funded by the U.S. Department of Energy, Office of Science, Office of Basic Energy Sciences under award no. DESC0001160.

2.1. Introduction

The remarkable optical, electrical, and mechanical properties of SWCNTs come with an important caveat: they only occur in long, low-defect, and individually dispersed nanotubes. However, SWCNTs have an inherent tendency to bundle together due to cumulatively strong van der Waals interactions, with the resulting, less exceptional material properties being more representative of the agglomerated bundle than of the individual tubes.[56] To overcome this limitation, in 2002, O'Connell *et al.* introduced a method of dispersing surfactant-stabilized individual SWCNTs in aqueous solutions via ultrasonication followed by ultracentrifugation.[11] This technique and its variants are foundational to many fundamental and applied studies as they allow SWCNTs to be analyzed at the single nanotube level[22, 57] and even further isolated into pure single chirality SWCNT structures.[38-41, 43, 45]

However, ultrasonication damages SWCNTs, creating defects and cutting them into short pieces,[29, 30] which dramatically degrade the electrical conductivity,[24] weaken the mechanical strength,[25] and in the case of semiconducting SWCNTs, quench the photoluminescence[28, 58]. Furthermore, both ultrasonication and ultracentrifugation require costly equipment, and the methods are time consuming and energy intensive, all of which present significant challenges to large-scale production. As such, many current studies that make use of individually dispersed SWCNTs are largely limited to the short version (typically 300-500 nm) of this extraordinary material.

To overcome these issues, alternative methods have been actively pursued. For instance, it has been shown by Subbaiyan *et al.*[59] that gentle stirring of SWCNTs in aqueous surfactant solutions can scratch off loose nanotubes from the surface without causing measurable damage to their carbon bonding structure. However, the procedure takes several weeks and the yield is extremely low, limiting it to microscopic sample preparation. Graf *et al.*[60] recently demonstrated high-speed shear mixing as a way to successfully disperse SWCNTs in toluene, but the method also is energy intensive and time consuming (96 h of high speed shear mixing is required). Moreover, toluene is incompatible with common SWCNT sorting processes that are aqueous based and is a less environmentally friendly solvent compared to water.

Here we introduce a new and unexpectedly simple method, which we call superacid-surfactant exchange (S2E), to achieve aqueous solutions of full-length individually dispersed SWCNTs, without causing structural damage. Using just two solution-mixing steps, S2E involves the direct neutralization of a SWCNT-superacid solution in the presence of a surfactant. Unlike ultrasonication, this new method yields

individual nanotubes within minutes without causing structural defects or cutting the nanotubes into short pieces. The processed SWCNTs feature an extremely low density of defects, bright and homogenous PL in the near infrared, and more than an order of magnitude improvement over sonicated controls in the electrical conductivity of transparent thin-films. We further demonstrated that using established sorting techniques, long SWCNTs of pure single chirality can be separated, highlighting the ability of S2E to produce full-length, chirality-sorted SWCNTs via scalable aqueous solution processing for a wide range of potential applications.

2.2. Experimental Section

2.2.1. Superacid-Surfactant Exchange Procedures

Raw HiPco SWCNT materials (Rice University, Lot #194.3) were dissolved in chlorosulfonic acid (Sigma Aldrich, 99.9%) at a concentration of ~0.5 mg/mL (the concentration varied from ~0.1 to ~0.5 mg/mL for different SWCNT sources). This SWCNT-superacid mixture was added drop-by-drop to an aqueous solution of 0.5 M NaOH and 1 wt/v% DOC (Sigma Aldrich, ≥97%) until the solution pH increased to ~11. (**Note**: the neutralization process is very aggressive; a significant amount of heat and acidic smog can be generated. Personal protective equipment, including goggles/facial mask, lab coats, and acid-resistant gloves are necessary. The neutralization should be performed in a fume hood.) Undissolved particulates were removed using a low-speed benchtop centrifuge at 6,000 g for 30 min. All dispersion and characterization experiments were performed at room temperature. This S2E procedure was applied to various carbon materials from major commercial sources.

Table S1 provides an overview of the sources and batch numbers of graphene and the four types of SWCNTs studied.

As controls, sonic-SWCNTs were prepared by the ultrasonication plus ultracentrifugtion approach from 1 mg/mL solutions of raw SWCNT material in deuterium oxide (D_2O, Cambridge Isotope Laboratories, Inc. 99.8%), following an established protocol, using DOC as the surfactant (tip sonication at 15 W, Qsonica S-4000) at increasing sonication times.

After the superacid-surfactant exchange, an aqueous solution of 1.5 wt/v% CTAB was added to the DOC-stabilized SWCNT solution, such that the final concentrations of CTAB and DOC were 0.5 wt/v% and 0.67 wt/v%, respectively. This mixing caused a phase separation to occur, with S2E-SWCNTs collecting in the bottom surfactant-rich phase, which appeared quite dark in color. This phase separation process can be accelerated by centrifugation at 2000 g for 2 min using a low-speed benchtop centrifuge (Eppendorf Centrifuge 5810R). The collected S2E-SWCNTs were then diluted to the desired concentration for further electrical and optical measurements.

2.2.2. SWCNT Length Characterization

The individually dispersed SWCNTs were deposited on (3-aminopropyl) triethoxysilane functionalized SiO_2/Si substrates. In order to totally remove the surfactants and other possible organic solvents, the coated wafers were annealed in air at 300 $^{\circ}$C for 1 h. All AFM images were recorded in tapping mode on a Veeco Multimode AFM with conical AFM probes backside-coated with gold (Tap300GD-G, with a force constant of 40 N/m, Ted Pella).

2.2.3. ATP-Sorting of S2E-SWCNTs

The ATP separation method was used to isolate (6,5)-SWCNTs from the S2E- and sonic-SWCNT samples.[59] Three major sources of SWCNTs, including HiPco, CoMoCAT SG76, and CoMoCAT SG65i, were used in this experiment to demonstrate the general compatibility of S2E. Since ATP separation is sensitive to the surfactant type and pH of the solution, we performed an extra step to remove the CTAB by centrifugal ultrafiltration (Amicon Ultra-15, PLHK Ultracel-PL Membrane, 100 kDa) and adjusting the pH to ~8.

2.2.4. Fabrication and Characterization of Transparent Conductive Film (TCFs)

Dispersed S2E-SWCNTs and sonic-SWCNTs were filtered through a 0.025 μm nitrocellulose membrane (Merck Millipore Ltd). The membranes were placed in a vacuum oven at room temperature for 12 h. After drying in a vacuum oven at room temperature, the nitrocellulose membrane with the attached SWCNT film was cut into 3 cm × 1 cm strips and transferred onto a glass slide.[61] Prior to transferring, the glass slides were cleaned in piranha solution at 90 °C for 45 mins, followed by rinsing in Nanopure water and blow-drying with argon. Then in order to fully remove the remaining surfactants and residues from the nitrocellulose membrane, the thin films were immersed in 40% nitric acid solution for 0.5 h and then immersed in Nanopure water for 2 h. We used a four-point probe method to measure the electrical conductivities of the films. The electrodes were deposited on SWCNT strips at equal spacing by thermally evaporating silver (80 nm thickness) using a Metra Thermal Evaporator. *I-V* curves were measured on a Cascade probe station using a Keithley

S4200 semiconductor parameter analyzer. Each data point was the average of at least 3 measurements.

2.2.5. Spectroscopic Characterization

The PL of the SWCNT solutions was characterized with a Horiba Jobin Yvon NanoLog spectrofluorometer using a liquid-N_2 cooled InGaAs array.[62] Note that for PL spectroscopy measurements, D_2O was used in place of Nanopure water as the solvent. UV-Vis-NIR absorption spectra were measured with a spectrophotometer equipped with a broadband InGaAs detector (Lambda 1050, PerkinElmer). For TCFs, an integrating sphere (Labsphere Model No. 150MM RSA ASSY) equipped with a broadband InGaAs detector installed to the UV-Vis-NIR spectrophotometer was also used. Raman scattering was measured from thin film samples using a LabRAM ARAMIS Raman microscope (Horiba Jobin Yvon) in duo scan mode, which averaged spectra from a 30×30 μm^2 area. Each sample was measured from at least 10 different regions and averaged to ensure the data are statistically meaningful.

2.2.6. Near IR photoluminescence Microscopy

Small aliquots of S2E-SWCNT and 2h sonic-SWCNT solutions in 1 wt/v% DOC-D_2O were physisorbed on poly D-lysine coated glass slides (Part No. P35GC-0-10-C, MatTek Corporation). Single tube PL imaging was performed on an inverted fluorescent microscope custom-built from a Nikon Eclipse Ti-U equipped with an oil immersion objective (UAPON 150XOTIRF, NA = 1.45, Olympus) to improve the collection efficiency in the NIR. SWCNTs were excited with a collimated, 730 nm diode laser (Shanghai Dream Lasers Technology) at 1 kW/cm^2 power density. The PL emission was collected using a liquid-N_2 cooled two-dimensional InGaAs detector

(Cougar 640, Xenics, Inc.) in Integrate Then Read mode. To achieve low dark current levels, broadband PL images were also obtained using Read While Integrate modes. The integration time was 4 s.

2.3. Results and Discussion

2.3.1. Aqueous Dispersion of Individual SWCNTs by Superacid-Surfactant Exchange

We found that the addition of HiPco SWCNTs dissolved in superacid to a basic aqueous solution of sodium deoxycholate (DOC) resulted in a homogeneous, black aqueous solution of SWCNTs (Figure 2-1a-d). This process takes just minutes to complete. UV-Vis-NIR absorption spectra (Figure 2-2e) and PL excitation-emission maps (Figure 2-2f) of the supernatant unambiguously confirm sharp absorption peaks and bright fluorescence that are characteristic of individually suspended semiconducting SWCNTs.

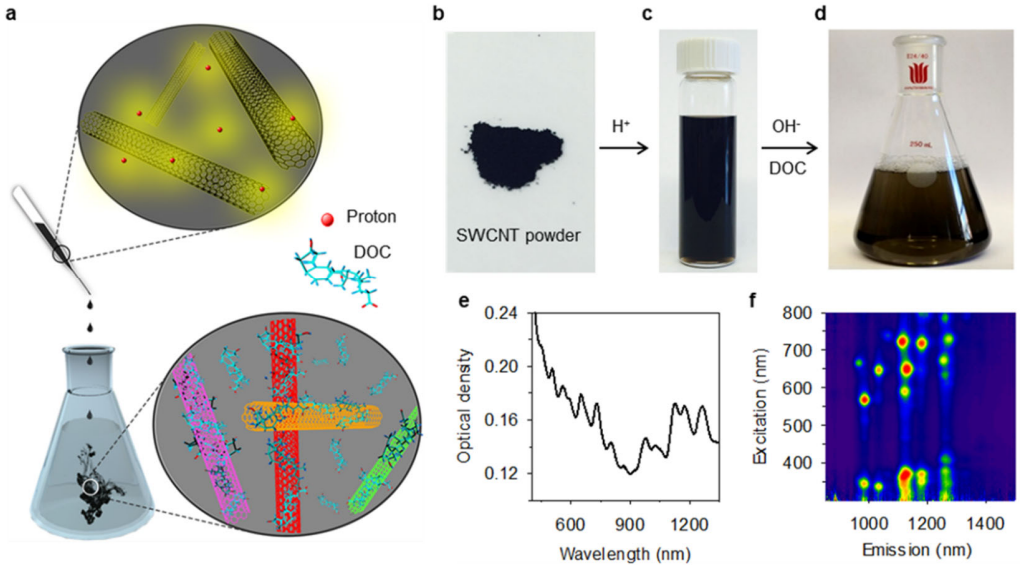

Figure 2-1. Superacid-surfactant exchange procedures. (a) Schematic illustration of the neutralization of a SWCNT-superacid suspension with NaOH aqueous solution in the

presence of the surfactant DOC. Photographs of (b) raw SWCNT powder, (c) SWCNT-superacid solution, and (d) aqueous solution of SWCNTs stabilized by 1 wt% DOC. (e) UV-Vis-NIR absorption spectrum and (f) excitation-emission PL map of 1 wt% DOC stabilized SWCNTs in D_2O, showing the optical fingerprints characteristic of individually dispersed SWCNTs.

Unlike ultrasonication and other previous SWCNT dispersion methods, our S2E technique is driven by two acid-base reactions that are chemically reversible:

$$(CNT)_{bundled} + H^+ \rightarrow (CNT)_{individual}H^+$$

$$(CNT)_{individual}H^+ + OH^- + DOC \rightarrow (CNT)_{individual}@DOC + H_2O$$

Crystalline SWCNTs can spontaneously dissolve in superacid, as established by Pasquali and co-workers. The superacid protonates the weakly basic nanotubes, exfoliating the bundled material into individual structures due to the Coulombic repulsion between the positively charged nanotubes. Our experiments suggest that as hydroxide anions neutralize the protonated SWCNTs in the second step, the "naked" nanotubes are then immediately encapsulated by the surrounding DOC molecules and thus stay as individual particles in the aqueous solution. This superacid-surfactant exchange process is sensitive to the solution pH. At pH ~11, the solution was stable for more than 6 months (Figure 2-2a-c). Further addition of the SWCNT-superacid solution can cause the pH to drop below ~7, at which point the nanotubes coagulated and precipitated (Figure 2-2d). We attribute this pH dependence to the fact that DOC has a pKa of ~6.7, therefore at low pH it loses its solubility and hence efficacy as a surfactant. Interestingly, adding cetrimonium bromide (CTAB) to the neutralized solution, the suspension can be concentrated easily to a high final concentration of ~80

mg/L (Figure 2-3). The addition of this second surfactant caused the solution to phase separate, which might have occured due to the specific molecular packing arrangement of CTAB and DOC on the SWCNT surfaces induced by Coulombic attractions, causing the materials to become more hydrophobic and collect in the surfactant-rich bottom phase.

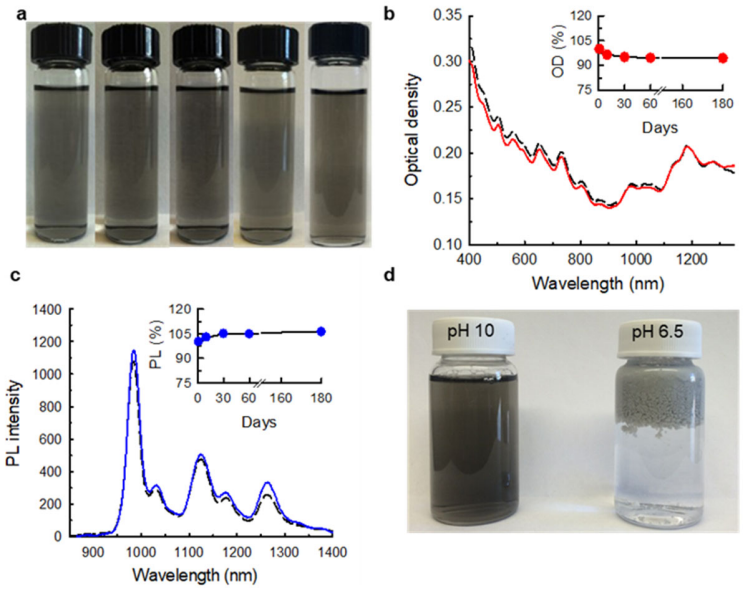

Figure 2-2. Stability of DOC-suspended HiPco SWCNTs by S2E. (a) Photographs of the stable S2E-SWCNT solution over a 6-month period. (b) UV-Vis-NIR absorption and (c) PL spectra at 565 nm excitation of the S2E-SWCNT solution after 1 h (dashed line) and 3 months (solid line). The inset plots present the relative changes of the optical density and PL intensity over time. (d) The pH dependence of DOC-dispersed SWCNTs. Note that at pH below ~7, the DOC begins to coagulate out of solution, losing its ability as a dispersant.

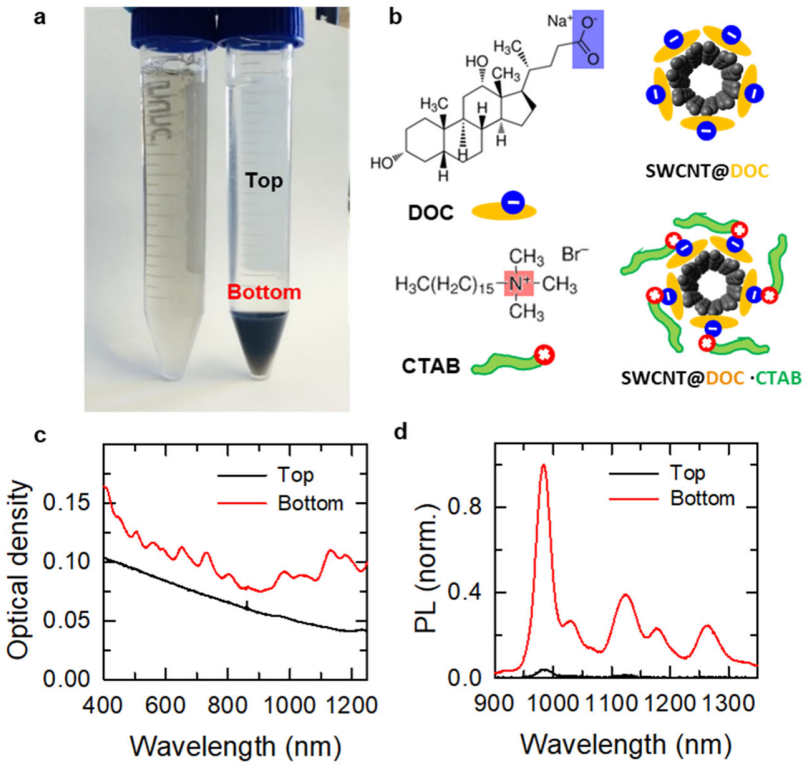

Figure 2-3. Extraction of SWCNTs in the DOC-CTAB-SWCNT system. (a) Photograph of the prepared solutions before (left) and after (right) phase separation, which shows SWCNTs concentrated in the bottom phase. (b) The molecular structures of CTAB and DOC, and the proposed surfactant packing on SWCNTs before and after the addition of CTAB. In the absence of CTAB, the hydrophobic parts of DOC interact more directly with SWCNTs while the negatively charged headgroups (blue circles) protrude outward. After the addition of CTAB, Coulombic attractions between the cationic heads of CTAB and the anionic heads of DOC shield the ionic groups, making the surfaces of the SWCNT/DOC more hydrophobic and triggering phase separation. (c) The UV-Vis NIR absorption and (d) PL emission spectra (at 565 nm excitation) of the separated top and bottom phases. The bottom fraction was diluted 4 times using 1

wt/v% DOC in D2O solution for spectral characterization. Note the significant enrichment (over 200-fold) of SWCNTs in the bottom phase.

We note that adding surfactant directly into the superacid-SWCNT solution does not work to suspend the nanotubes individually in water because the surfactant molecules are chemically unstable in the superacid. Although HiPco materials, the most studied source of SWCNTs, were used here for demonstration purposes, other sources of SWCNTs, including CoMoCAT SG65i, CoMoCAT SG76, and MEIJO eDIPS EC1.0, were similarly successful at individual dispersal (Figure 2-4). Our experiments further suggest that S2E is an effective and general method for dispersing other carbon nanomaterials, including graphene in water.

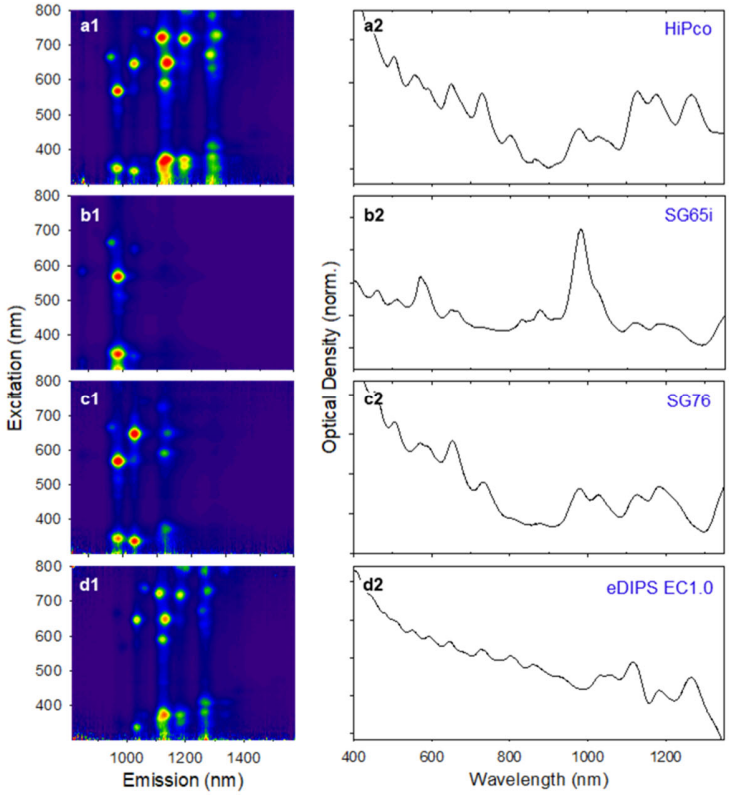

Figure 2-4. Aqueous dispersions of SWCNTs from four different sources using the S2E method. (a) HiPco, (b) CoMoCAT SG65i, (c) CoMoCAT SG76, and (d) MEIJO eDIPS EC 1.0 SWCNTs were dispersed in 1 wt/v% DOC-D_2O for excitation-emission PL mapping (1, left column) and absorption measurements (2, right column).

2.3.2. The Nondestructive Nature of S2E Enable Retention of the SWCNTs' Full Length

The S2E-SWCNTs were significantly longer than controls prepared using ultrasonication (sonic-SWCNTs; Figure 2-5a-c). After only 2 h of sonication, HiPco sonic-SWCNTs were cut into pieces with an average length (L_{avg}) of just 0.35 μm. In contrast, the L_{avg} of the S2E-SWCNTs was 1.18 μm, which was 237% longer than the sonic-SWCNT control. The average length of the sonic-SWCNTs continued to decrease with increasing sonication time (Figure 2-5d). Similar trends were observed for the three other sources of SWCNTs studied, including CoMoCAT SG65i, CoMoCAT SG76, and MEIJO eDIPS EC1.0. L_{avg} for the corresponding S2E-SWCNTs was 1.64 μm, 1.75 μm, and 2.96 μm, respectively, which was more than 460% as large as the sonicated controls (Figure 2-6).

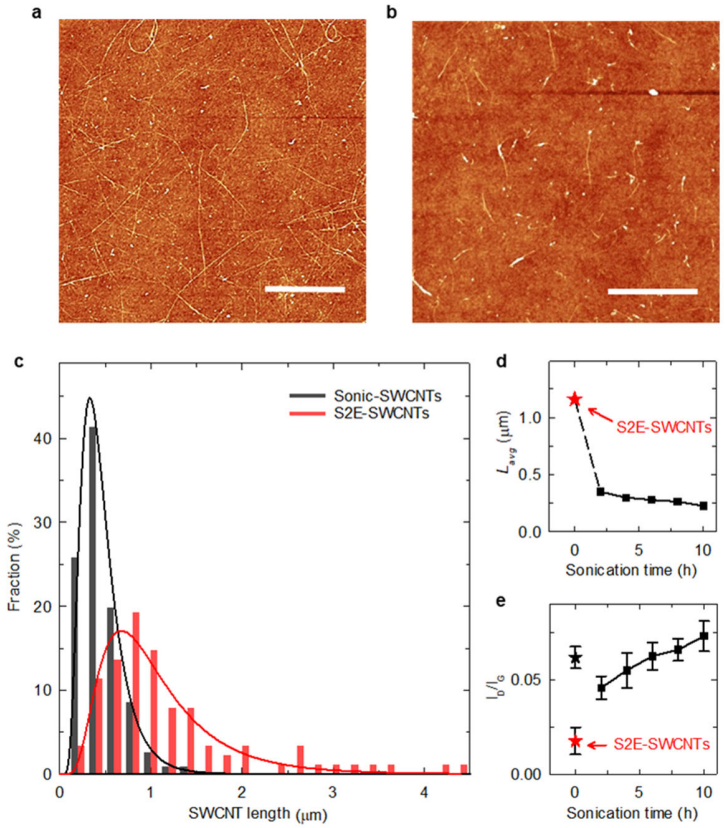

Figure 2-5. The nondestructive nature of superacid-surfactant exchange. Representative AFM topography images of (a) S2E-SWCNTs and (b) sonic-SWCNTs on a Si substrate. Scale bars: 1 μm. (c) Length distributions of S2E-SWCNTs (red) and sonic-SWCNTs (black). The length distributions are fitted by log-normal functions (red and black lines). (d) The average SWCNT length (L_{avg}) and (e) Raman I_D/I_G ratio as a function of sonication time. The red stars and black squares represent S2E-SWCNTs and sonic-SWCNTs, respectively. The black star in **e** represents the raw HiPco SWCNT material.

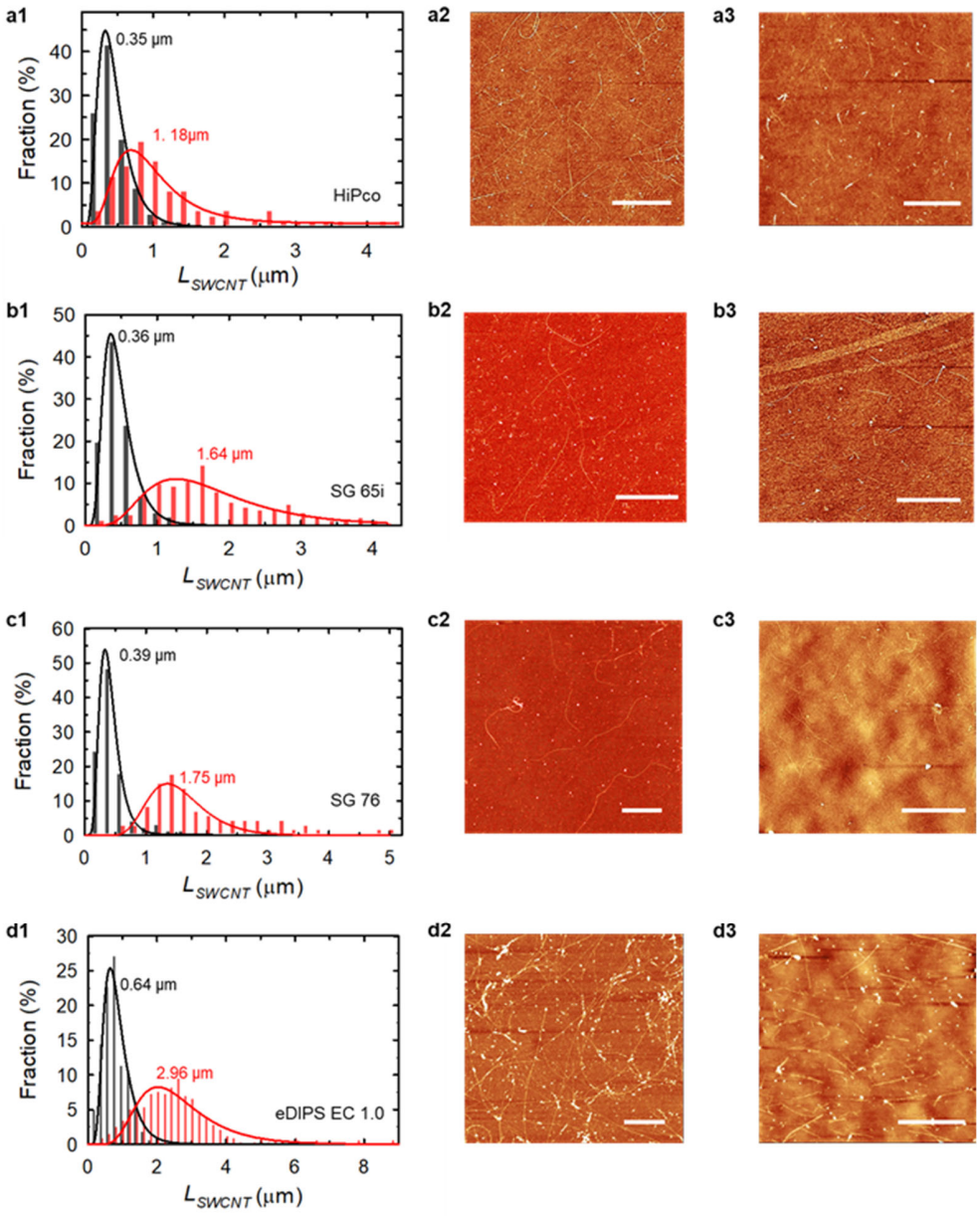

Figure 2-6. AFM imaging and length distribution characterization of S2E-SWCNTs and sonic-SWCNTs prepared from four sources of SWCNTs. (a) HiPco. (b) CoMoCAT SG65i. (c) CoMoCAT SG76. (d) MEIJO eDIPS EC1.0. (a-d1), Length distribution histograms of the S2E-SWCNTs (red) and sonic-SWCNTs (black) as measured by AFM. Log-normal distribution functions (solid lines) were used to fit the length

distributions. (a-d2) AFM images of the corresponding S2E-SWCNTs. (a-d3) AFM images of the respective sonic-SWCNTs. Scale bars are 1 μm.

We further confirmed the nondestructive nature of S2E by monitoring the presence of nanotube defects using Raman spectroscopy. We found that S2E-SWCNTs had the lowest I_D/I_G ratio at ~0.02 for HiPco materials. In contrast, the I_D/I_G for HiPco sonic-SWCNTs increased, ranging from ~0.05 to ~0.08 with increasing sonication time. Interestingly, I_D/I_G is roughly proportional to $1/L_{avg}$, suggesting that the defects introduced by sonication are mainly located at the nanotube ends (i.e., end defects) which define the length of the tube (Figure 2-5e). I_D/I_G of the S2E-SWCNTs was even lower than the starting raw HiPco material, possibly due to the purification effect of the superacid. Only nanotubes with a highly crystallized structure can be fully protonated by the superacid, while amorphous carbon and highly defective tubes cannot dissolve well, causing these materials to remain as solids that precipitate out of solution, thus lowering the total defects in the S2E-processed samples.

2.3.3. Enhanced Electrical Conductivity in Transparent Conductive Films from Long SWCNTs

Transparent conducting films (TCFs) are an emerging application of carbon nanotubes. The sheet resistance (R_S) of a nanotube TCF is dominated by the junction resistance. The longer the nanotubes, the fewer the junctions that are encountered by the current traversing the film, and as a result, the conductivity of a nanotube film scales with nanotube length by a power law. Based on four-point probe measurements, we found that TCFs made from S2E-SWCNTs showed an R_S as small as 66 Ω/sq at 75%

optical transmittance at 550 nm, which was 11.5-times more conductive than the sonic-SWCNT control TCF (760 Ω/sq; Figure 2-7a,b).

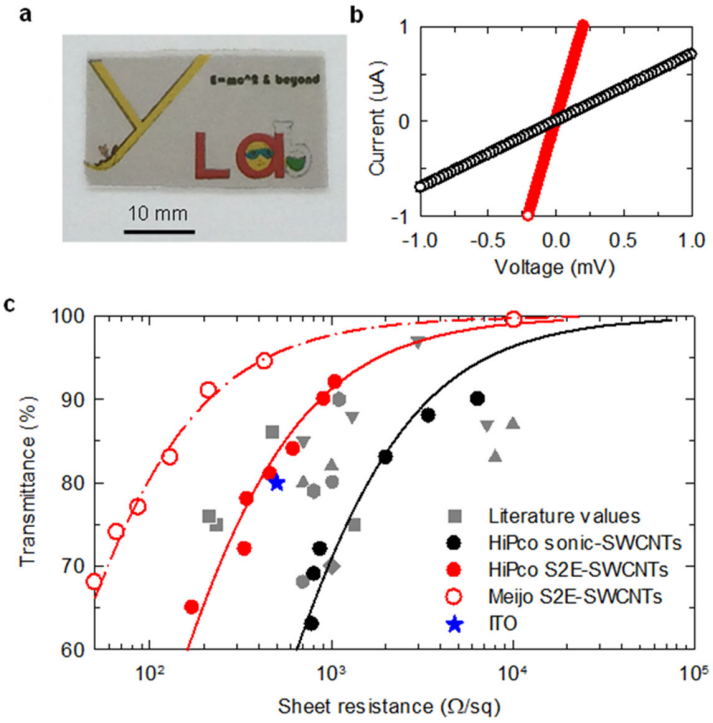

Figure 2-7. Electrical and optical properties of S2E-SWCNT TCFs benchmarked against sonic-SWCNT controls and ITO. (a) Photograph of a TCF fabricated from S2E-SWCNTs. (b) *I-V* curves of TCFs made from S2E-SWCNTs (red) and sonic-SWCNTs (black) at 75% transmittance at a wavelength of 550 nm. (c) Sheet resistance versus optical transmittance for TCFs made from S2E-SWCNTs (red circles) and sonic-SWCNTs (black circles). The sources of SWCNTs used were MEIJO eDIPS EC1.0 (open red circles) and HiPco (closed red circles). The blue star indicates the typical sheet resistance of an ITO film at ~80% transmittance. Other data points (grey) shown are literature values of HiPco TCFs as cited in the text.

We further evaluated the performance of these TCFs using the ratio of the optical (σ_{op}) and current (σ_{dc}) conductivity, which is correlated to the sheet resistance (R_S) and the optical transmittance (T), according to the following equation:

$$\frac{\sigma_{op}}{\sigma_{dc}} = \left(\frac{1}{\sqrt{T}} - 1\right) \times \frac{R_S}{188}$$

A lower $\frac{\sigma_{op}}{\sigma_{dc}}$ value indicates better opto-electronic performance of the TCF (i.e., higher conductivity at higher optical transparency). Figure 2-7c shows the sheet resistance-transmittance curves of TCFs fabricated from HiPco S2E-SWCNTs in comparison with the sonic-SWCNT control and other HiPco TCFs reported in the literature. At 550 nm, the HiPco S2E-SWCNT TCFs had a $\frac{\sigma_{op}}{\sigma_{dc}}$ of 0.26, which was 3.4-times more conductive than the sonicated controls. The conductivity of these HiPco thin films is comparable with the best reported in the literature.

In the case of MEIJO eDIPS EC1.0 SWCNTs, the enhancement was even more pronounced, with a $\frac{\sigma_{op}}{\sigma_{dc}}$ value of 0.06 for S2E-SWCNTs and 0.54 for the sonication control, which is an 8-fold improvement in the conductivity (Figure 2-7c). The conductivity of the MEIJO eDIPS EC1.0 S2E-SWCNTs (130 Ω/sq at 83% transmittance) was also significantly better than that of indium tin oxide (ITO), the most widely used transparent conducting film (blue star in Figure 2-7c).

2.3.4. Enhanced Photoluminescence of Long SWCNTs

Separating SWCNTs by chirality is important for taking full advantage of the remarkable optical and electrical properties of these low dimensional materials, as well as to enable important fundamental studies.[63, 64] Nearly all established separation

techniques are based on aqueous solution processing methods. However, the cutting effects of ultrasonication and the limited scalability of ultracentrifugation have created major obstacles to obtaining long, chirality-pure SWCNTs at reasonably large quantities.

To demonstrate that our S2E dispersion method is compatible with established sorting techniques, we applied aqueous two phase (ATP) separation. Although ATP has been successfully used to purify single chiralities from a SWCNT mixture, the sorted nanotubes are typically short (< 500 nm) due to the need for sonication in order to prepare the starting aqueous solution of individually dispersed nanotubes. Applying ATP separation to S2E dispersed nanotubes is straightforward since the aqueous S2E-SWCNT solution can be directly used as a starting material for the separation method.

Figure 2-8a shows the UV-Vis-NIR absorption spectra of (6,5)-SWCNT sorted from S2E-SWCNT solutions of HiPco materials that initially contained an assortment of different chiralities. The successful separation is clearly evident by the sharp absorption peaks characteristic of the (6,5) chirality, including its first (E_{11} at 987 nm) and second (E_{22} at 571 nm) optical transitions. Consistently, the PL map (Figure 2-8b) also presents a single excitation-emission feature of (6,5)-SWCNT, thus unambiguously confirming the separation of a single chirality from the heterogeneous starting material.

Notably, we observed that the NIR PL of the S2E-SWCNTs was significantly brighter than the sonication control. Using PL imaging, we could quantitatively analyze the fluorescence at the individual particle level. In Figure 2-8c,d we compared the NIR PL images of S2E (6,5)-SWCNTs to the sonic (6,5)-SWCNT control, which was also

sorted to pure single chirality via ATP. Although the absorption spectra for the sorted S2E-SWCNTs and the sonicated control are nearly identical, the individually resolved fluorescent nanotubes exhibit significant differences in both length distribution and PL intensity. More than 50% of the fluorescent nanotubes from the sonication control were shorter than the spatial resolution of our microscope (0.56 μm) and therefore displayed as "dots" in the image. In contrast, 80% of the S2E-SWCNTs can be spatially resolved to reveal their lengths, which ranged from 0.6 μm to 7.44 μm in consistence with AFM measurements (Figure 2-8e).

The PL down the length of these S2E-SWCNTs was homogeneous, both in terms of emission wavelength and intensity, which excludes the existence of quenching sites. Since the exciton diffusion length at room temperature is significantly lower than 500 nm in defect-free nanotubes, the PL intensity is not expected to vary significantly along the length of SWCNTs that are longer than the diffraction limit. However, we observed a correlation between the PL intensity per unit length and the length in the S2E (6,5)-SWCNTs. For longer SWCNTs (> 1.2 μm), the average PL intensity per unit length was 96% brighter than that of the sonicated control. Even for those nanotubes within the same length range (0.6–1.2 μm), S2E nanotubes were still 45% brighter than the sonication control (Figure 2-8f,g). This intensity difference suggests that besides cutting, ultrasonication also introduces quenching defects, which causes excitons to decay non-radiatively. Eliminating the need for sonication, as made possible through S2E, avoids cutting nanotubes and the introduction of structural defects, opening the possibility of scaled solution processing of long, chirality pure, individual SWCNTs that are largely free of defects.

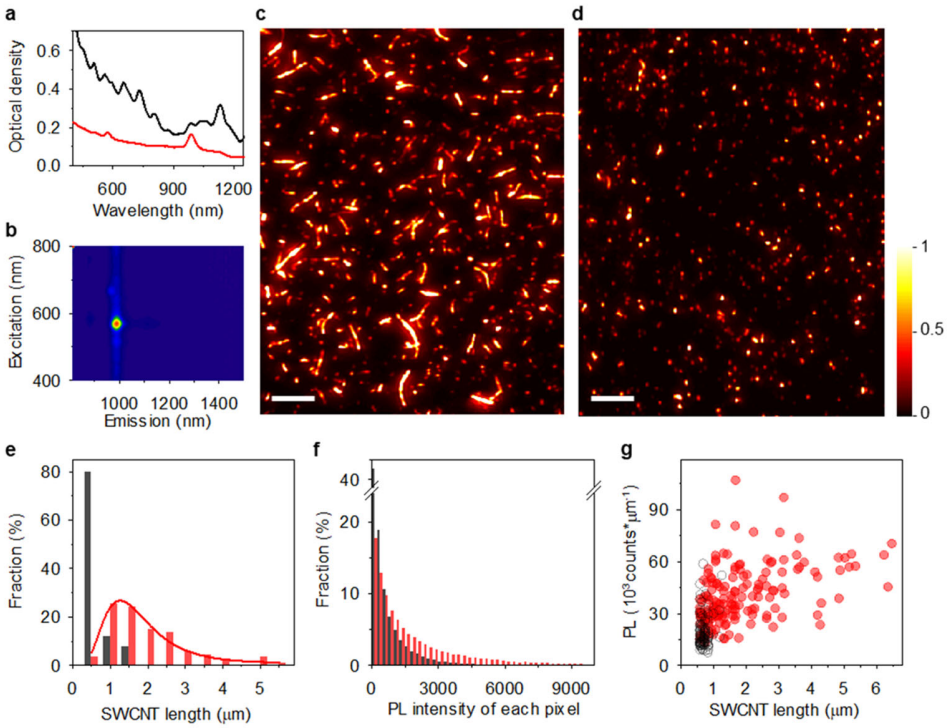

Figure 2-8. Bright NIR PL from long, single chirality-pure (6,5)-SWCNTs sorted from S2E-SWCNTs and sonic-SWCNTs. (a) UV-Vis-NIR absorption spectra of HiPco S2E-SWCNT starting material (black) and (6,5)-SWCNTs sorted from S2E-SWCNTs via ATP (red). The absorption spectra are offset for clarity. (b) Excitation-emission PL map of the sorted S2E (6,5)-SWCNTs in 1 wt/v% DOC-D_2O. Broadband (900–1600 nm) PL images of (c) the sorted S2E (6,5)-SWCNTs and (d) the sonicated (6,5)-SWCNT control. Scale bars are 10 mm. (e) The length distributions of the S2E (6,5)-SWCNTs (red) and sonicated (6,5)-SWCNT control (black). (f) Histogram of the PL intensity of each pixel. Intensity counts lower than 100 were attributed to background noise and rejected from the statistics. (g) Correlation between PL intensity per unit length and the SWCNT length for S2E (6,5)-SWCNTs (red) and the sonicated (6,5)-SWCNT control (black).

2.4. Conclusions

We have demonstrated a nondestructive method to address the long-standing challenge of dispersing full-length SWCNTs in water by directly neutralizing SWCNT-superacid solutions in the presence of a surfactant. This novel method is unexpectedly simple, producing aqueous solutions of individually-dispersed nanotubes in minutes and completely eliminating the need for ultrasonication and ultracentrifugation. It is also fully compatible with established chirality sorting techniques, allowing long, individual semiconducting nanotubes to be scalably separated for the first time. The processed nanotubes retain their full lengths and are nearly defect-free, demonstrating significantly improved optical and electrical properties compared to sonicated controls. Because of its nondestructive nature, S2E can reveal the true distributions of diameter, chirality, and length of a sample, and hence may be adapted as a powerful metrology method to provide valuable feedbacks to guide nanotube synthesis and processing. This nondestructive processing method can be readily applied to other carbon nanomaterials, including graphene, thus paving the way for scalable aqueous solution processing of high quality carbon nanomaterials for many fundamental studies and practical applications where high quality, long, and defect-free carbon nanomaterials are actively sought after.

3. Impact of SWCNT/superacid concentration on S2E: Self-Sorting of 10 μm long SWCNTs

This chapter is adapted from a published manuscript:[65]

Wang, P.; Barnes, B.; Wu, X.; Qu, H.; Zhang, C.; Headrick, R.; Pasquali, M.; Wang, Y. *Adv. Mater.* **2019**, 1901641.

Y.W. and P.W. conceived and designed the experiments. P.W. performed the major experiments. B.B. and C.Z. fabricated the electrodes and deposited the CNT films for transport measurements. X.W. and H.Q. performed photoluminescence microscopy measurement. R.H. conducted the capillary thinning experiments. Y.W. and P.W. wrote the manuscript with inputs from all authors.

This work is not directly supported by a grant. However, the authors wish to acknowledge the University of Maryland and federal funding agencies for providing student supports to B.B. and C.Z. (NIH/NIGMS R01GM114167), and H.Q., who was supported by the Center for Enhanced Nanofluidic Transport (CENT), an Energy Frontier Research Center funded by the U.S. Department of Energy, Office of Science, Basic Energy Sciences under Award # DE-SC0019112). R.J.H. and M.P. were supported by the Air Force Office of Scientific Research (AFOSR) grant FA9550-15-01-0370, the Robert A. Welch Foundation grant C-1668, and the Department of Energy (DOE) award DE-EE0007865. AFM images were obtained using a shared system supported by the NSF MRI program (CHE1626288). P.W. gratefully acknowledges the Millard and Lee Alexander Fellowship in Chemistry from the University of Maryland.

3.1. Introduction

We have demonstrated the non-destructive dissolution of SWCNTs in aqueous solution by S2E. However, due to the polydispersity of SWCNT length in the starting raw materials, there is still a large portion of short SWCNTs (<500 nm) exist in the resulting solution after S2E, even no ultrasonication is used (see the Figure 2-5c, red line). In this context, thus, how to selectively remove those short tubes (<500 nm) and collect valuable long tubes (>10 μm) represent an important step to fully harness the potential of electrical, mechanical, and optical properties of these remarkable nanomaterials.

Several length sorting techniques including size exclusion chromatography,[66] density gradient ultracentrifugation,[67, 68] cross-flow filtration,[69] and polymer precipitation[70] have been reported. However, the sorted nanotubes are still short due to the ultrasonication at the initial sample preparation step, which cuts long SWCNTs into smaller pieces. The longest portion attained thus far has an average length (L_{avg}) less than ~1.5 μm[68] and a considerable population (~35% to ~75%) are short nanotubes (<500 nm). Moreover, all of these length sorting methods have relatively low throughput. Therefore, it remains an unmet challenge to obtain long SWCNTs in a scalable manner and study their collective properties.

Here, we demonstrate that the sorting of ultralong nanotubes (>10 μm) can be realized by "self-sorting" in aqueous solutions. In contrast to other reported mechanisms, which all rely on SWCNT interactions with other media, such as gels,[66, 71] density gradients,[67, 68] porous membranes,[69] or polymers,[70] the separation here occurs solely due to the length-dependent interactions between the SWCNTs themselves. This process is highly scalable, yielding a significant fraction of ultralong nanotubes featuring a narrow distribution. Importantly, the sorted SWCNTs are individually stabilized in water without additives, such as density gradient media, making them well compatible with established aqueous-based SWCNT sorting (e.g., by diameter, electronic type, or chirality) and other processing methods, allowing us to produce aligned thin films from long SWCNTs with high semiconducting purity (>99%). We further demonstrate that thin film transistors (TFTs) fabricated from these films exhibit a current ON/OFF ratio of more than 1000 with the carrier mobility exceeding 90 $cm^2 \cdot V^{-1} \cdot s^{-1}$, which is ~10 times better than short tube controls, exceeding the

conventional TFT materials such as organic semiconducting polymers (<1 $cm^2 \cdot V^{-1} \cdot s^{-1}$),[72] nanocrystalline silicon (~50 $cm^2 \cdot V^{-1} \cdot s^{-1}$)[73] and approaching that of polycrystalline silicon TFTs (~100 $cm^2 \cdot V^{-1} \cdot s^{-1}$)[74, 75].

3.2. Experimental Section

3.2.1. SWCNT Dispersion by S2E and Iterative Length Self-Sorting

EC 1.5 SWCNTs were obtained from Meijo Nano Carbon Co., Ltd. The SWCNTs (20 mg) and $ClSO_3H$ (20 mL; Sigma Aldrich, > 99%) were mixed and stirred at 1200 rpm with a magnetic stir bar for 3 days or until fully dissolved in a 100 mL round-bottom flask equipped with a ground-glass joint to prevent moisture from the air from entering the system. Prior to the S2E step, the mixture was diluted to the desired concentration using pure $ClSO_3H$. The SWCNT/CSA mixtures with various concentrations were then added dropwise into an aqueous solution of NaOH (0.75 M) and DOC (~0.08 wt/v%) (Sigma Aldrich, > 97%) with vigorous stirring so that the pH decreased to ~7-8. To achieve this pH condition, typically ~65 parts of NaOH-DOC are needed to neutralize one part of SWCNT/CSA mixture. (*Safety note: the neutralization process is aggressive and should be performed in a fume hood as a significant amount of heat and acidic smog can be generated. Personal protective equipment, including goggles/facial mask, lab coats, and acid-resistant gloves are also necessary.*) The solution was further stirred, followed by the addition of several drops of HCl (1 M) aqueous solution to protonate the DOC molecules, causing them to coalesce into dark grey/black precipitates along with the SWCNTs. A 47 mm sized polyvinylidene fluoride filtration membrane was used to filter and collect the precipitates. The dark grey/black precipitates were then mixed with nanopure water and

NaOH (1 M) was used to tune the pH to ~7 to 8, and stirred for 1-3 days. The resulting black solution was then centrifuged at 20,000 rpm for 1.5 h in a SW 41 Ti rotor using an Optima XE-90 ultracentrifuge (Beckman Coulter) to remove undissolved SWCNT bundles. For iterative S2E processes, the precipitated bundles were collected and sequentially rinsed with Nanopure^{TM} water and isopropanol several times to remove the DOC surfactants. After drying in vacuum at 80 ºC for overnight, the clean SWCNT bundles were weighed and re-dissolved in CSA to the desired concentrations (typically at ~70% concentration of the preceding cycles), followed by additional cycles of sorting. The last step of the length sorting process usually involves dissolving the longest nanotube precipitates in CSA at a sufficiently low concentration of ~0.1 mg/mL followed by S2E. Note that ~0.1 mg/mL was chosen as a tradeoff between the long length of SWCNTs with the final aqueous solution concentration.

3.2.2. Capillary Thinning Extensional Viscosity Measurement

The diameter of the SWCNTs d was measured to be 1.52 ± 0.28 nm based on TEM measurements (JOEL JEM 2100). SWCNT mass fraction was converted to volume fraction by calculating the theoretical density of the SWCNTs (1.34 g/cm^3). The initial SWCNT length distribution was estimated by following a previously described study.[76] Briefly, the extensional viscosity of the CNTs dissolved in CSA at 117 and 181 ppm by volume was measured four times with capillary breakup extensional rheology using a Cambridge Trimaster capillary thinning rheometer. The extensional viscosity measurement was used to calculate the SWCNT viscosity average aspect ratio (L_w/d) = 5130 ± 130. The isotropic cloud point φ_{iso} was measured by imaging SWCNT solutions in flame-sealed glass capillaries (VitroTubes) with

polarized light microscopy using a Zeiss Axioplan optical light microscope. Solutions were diluted until birefringence no longer appeared in the samples (74 ± 10 ppm by volume). The ratio of the experimentally measured isotropic cloud point φ_{iso} (volume fraction) to the theoretical value for monodisperse rigid rods $\varphi_{Onsager} = 3.34(L_v/d)^{-1}$ was used to estimate the polydispersity index σ ~1.41 and the L_{avg} was then calculated as ~4.5 μm.

3.2.3. Sorting S2E-SWCNTs by ATP

We used ATP to separate the nanotubes by electronic type, which involved mixing 1-part of the DOC stabilized SWCNT solution with 0.3-parts of 20% dextran (DX) and 0.3-parts of 50% polyethylene glycol (PEG) aqueous solution to yield ~0.2-parts of SWCNTs concentrated in the bottom DX-enriched phase after mild centrifugation at 4000 g for 60 s. DOC surfactants were then gradually replaced by a sodium cholate (SC) and sodium dodecyl sulfate (SDS) co-surfactant system following the reported procedure so that the final concentration of SC and SDS were 0.9% and 0.7%, respectively. Multiple cycles of this metallic/semiconducting SWCNT sorting process were applied until a desired purity of semiconducting SWCNTs was reached. The PEG and DX polymers were further removed from the final semiconducting SWCNTs enriched solution by an ultrafiltration step using a centrifugal ultrafiltration tube (Amicon Ultra-15, PLHK Ultracel-PL membrane, 100 kDa) before making thin films.

3.2.4. Fabrication of Thin Film Transistors and Electrical Measurement

To eliminate the potential influence of metallic SWCNTs and nanotube density on the measurement of the electrical properties, all semiconducting SWCNTs used were sorted by an identical ATP recipe and cycles and the SWCNT density in the fabricated devices was carefully adjusted to be equal. Solutions of ATP sorted semiconducting SWCNTs of different nanotube lengths were filtered through a 0.025 μm nitrocellulose membrane (Merck Millipore Ltd.) to form a thin film consisting of a random SWCNT network. Films consisting of aligned SWCNTs were fabricated by following a reported procedure.[77] Heavily n-doped silicon wafers (Silicon Quest International) with a 300 nm thermally grown SiO_2 layer were used as the back-gated substrates. SWCNT thin films were placed on the SiO_2 substrates with compressed force and annealed at 95 ºC so that the films were firmly attached to the substrates. An organic solvent (acetone or chloroform) bath was used to totally dissolve and remove the filter membrane. The substrates were then annealed in Ar at 300 ºC to increase the adhesion with SWCNTs. Standard bilayer photolithography using LOR-5B as the sacrificial layer and Shipley 1813 as the photoresist was used to define the patterns for electrode deposition (channel length and width were 15 and 35 μm, respectively). 5 nm of titanium and 30 nm of palladium were subsequently deposited on the Si wafers by Ebeam deposition (Angstrom NexDep Ebeam evaporator). After a standard lift-off procedure, another bilayer photolithography process was used again to remove undesired SWCNTs by oxygen plasma etching so that the adjacent transistors were electronically isolated. Electrical measurements were performed on a Keithley 4200-SCS probe station.

3.2.5. Spectroscopic and Microscopic Characterization

UV-vis-NIR absorption spectra of the S2E-SWCNTs supernatant after centrifugation were measured using a Lambda 1050 (Perkin Elmer) spectrometer with a broadband InGaAs detector. The resonant Raman spectra of the ATP-sorted SWCNTs was measured by a LabRAM ARAMIS Raman microscope (Horbia Jobin Yvon) with three different excitation laser sources (532 nm, 633 nm, and 785 nm). SEM images were collected by a SU-70 SEM (Hitachi). For PL microscopy measurements, the semiconducting enriched long SWCNTs after ATP sorting were drop cast onto Si wafers coated with 50 nm gold (Ebeam deposition) and followed by a 50 nm polystyrene layer (spin coating). Single nanotube PL imaging was performed on an IR optimized Olympus LCPLN100XIR objective (100x NA 0.85) and a liquid-N_2 cooled (-190 ^{o}C) two-dimensional InGaAs detector (Cougar 640, Xenics, Inc.). SWCNTs were excited with a collimated, 730 nm diode laser (Shanghai Dream Lasers Technology) at a power density of 50 W/cm^2.

3.3. Results and Discussion

3.3.1. Impact of SWCNTs/Superacid Concentration on the Length Distribution of S2E-SWCNTs

We started this self-sorting process by dissolving raw SWCNT materials into superacid, followed by adding the SWCNT/superacid dispersion into an aqueous solution containing DOC as the surfactant and sodium hydroxide. The aqueous dispersion is then centrifuged to separate bundled nanotubes from those individually dispersed in the supernatant.

SWCNTs spontaneously dissolve in superacid to form an optically homogenous solution at high concentrations (~0.61 vol%, or ~8.8 mg/mL).[51] In this superacid,

SWCNTs behave as a weak base that can be protonated. The protonation induces Coulombic repulsion between nanotubes, which overcomes the strong tube-tube van der Waals interaction allowing the SWCNTs to individually dissolve in the superacid to form a thermodynamically stable solution.[51] Unlike many other acids such as nitric acid,[78, 79] nitric/sulfuric acid mixture[80] or hydrogen peroxide/sulfuric acid mixture,[81] which can oxidize SWCNTs, chlorosulfonic acid is a true solvent that dissolves SWCNTs without oxidation.[51, 82] The sidewall protonation effect is completely reversible and the structures of SWCNTs can be fully recovered as evidenced by spectroscopy studies. due to sidewall protonation induced Coulombic repulsion.[50] Once dissolved in CSA, the SWCNTs behave like rigid rods with ultrahigh aspect ratios (length/diameter, *L/d*). The phase behavior for rods of monodisperse length was first described by Onsager[83] and Flory,[84] then extended to polydisperse rods by Wensink and Vroege,[85] and finally applied to SWCNTs by Green.[86] These theories have been shown to well describe the SWCNTs dissolved in CSA, which are polydisperse in aspect ratio and exhibit distinct phase behavior at different concentrations. At sufficiently low SWCNT concentration, the solutions are isotropic and all the SWCNTs freely rotate as Brownian rods. Increasing the SWCNT concentration beyond a critical value (the isotropic cloud point, φ_{iso}) leads to the formation of a nematic liquid crystalline phase that coexists within an isotropic phase. This transition into a biphasic system occurs as the SWCNTs sacrifice rotational entropy to maximize translational entropy. Further increasing the concentration beyond the nematic point (φ_{nem}) causes all of the SWCNTs to transit into a fully liquid crystalline nematic phase.

Both φ_{iso} and φ_{nem} are linearly related to the inverse aspect ratio of the rods (here $\varphi_{iso} = 3.29(L/d)^{-1}$ and $\varphi_{nem} = 4.19(L/d)^{-1}$) and these scaling laws have been applied to polydisperse CNT solutions[86] and confirmed experimentally.[76] Indeed, the polydispersity in aspect ratio of the SWCNTs leads to a self-partitioning of the longest SWCNTs into the nematic phase while the shortest nanotubes remain in the isotropic phase (Figure 3-1a). On the other hand, the CSA molecules on SWCNTs can be spontaneously replaced by DOC molecules in a straightforward superacid-surfactant exchange (S2E) process to produce surfactant-stabilized individual SWCNTs. In this context, we hypothesize that during S2E, the individual SWCNTs in the isotropic phase are maintained far apart from each other while the CSA is neutralized such that the DOC molecules can diffuse to their surfaces before re-bundling can occur. On the other hand, the SWCNTs in the nematic phase readily bundle and precipitate before DOC can stabilize them individually in the aqueous dispersion. Therefore, by tuning the SWCNT concentration, it should be possible to preferentially bundle long nanotubes during S2E because long CNTs concentrate in the liquid crystalline phase due to their higher excluded volume, and once bundled, they precipitate during centrifugation, leaving short SWCNTs individually dissolved in the aqueous solution (Figure 3-1b).

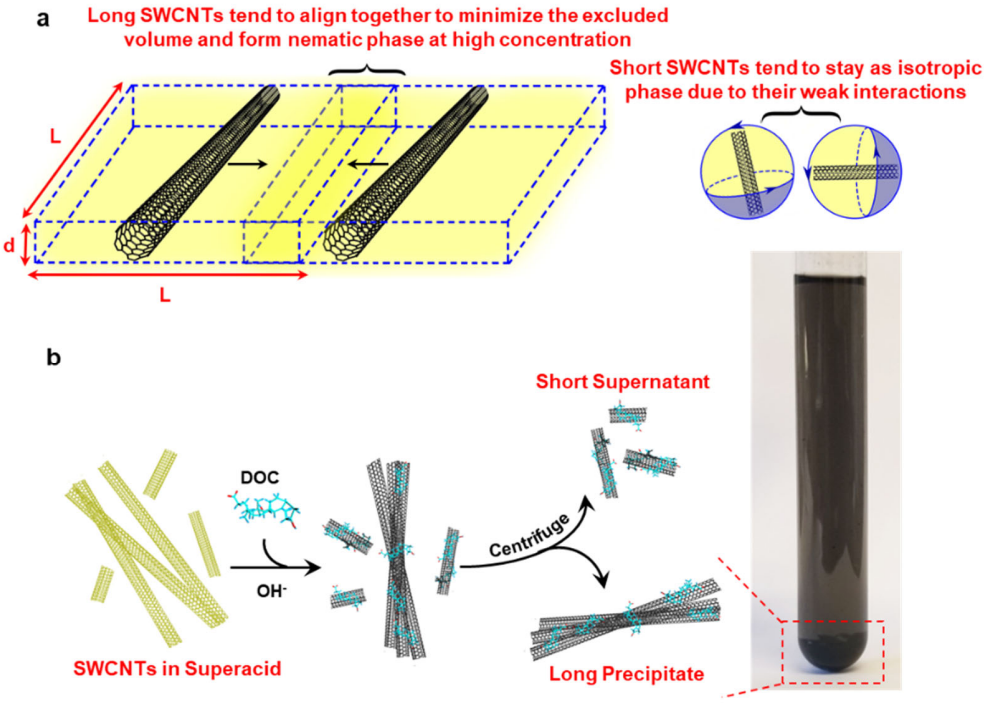

Figure 3-1. Schematic illustrations of the self-sorting mechanism and procedures. (a) Long SWCNTs dissolved in superacid tend to align together to minimize the excluded volume (V) and form a nematic phase. The excluded volume scales with dL^2, where d and L are the SWCNT diameter and length respectively ($V \propto dL^2$). Short SWCNTs in superacid tend to stay in an isotropic phase due to their limited interactions. (b) The SWCNTs are dissolved in superacid and subsequently neutralized with NaOH and DOC to produce short, individual nanotubes that are stabilized by surfactant in the aqueous solution. Meanwhile, long carbon nanotubes bundle and form precipitates, which can be separated from the dispersion by centrifugation.

We first studied the impact of SWCNT/CSA concentration on S2E to understand how it could potentially be employed to separate the nanotubes by length. AFM was used to characterize the length distribution of the DOC-stabilized SWCNTs

in the aqueous supernatant after centrifugation. Figure 3-2a-e shows representative AFM topographic images of the SWCNTs as a function of the initial nanotube concentration in CSA. At a high concentration of ~0.7 mg/mL, only short SWCNTs with an L_{avg} of ~0.1 μm were found in the supernatant. As the concentration decreases, we began to observe longer nanotubes in the supernatant, and at a dilute concentration of ~0.1 mg/mL, a maximum L_{avg} of ~3.1 μm was reached.

Analogous to the molecular weight polydispersity index in polymer physics, we calculated the length polydispersity index (*LPDI*) as a ratio of the number-averaged lengths (L_{avg}) and length averaged lengths (L_l) to quantify the length distribution:

$$L_{avg} = \frac{\sum_i^N L_i}{N}$$

$$L_l = \frac{\sum_i^N {L_i}^2}{\sum_i^N L_i}$$

$$LPDI = \frac{L_l}{L_{avg}}$$

LPDI is a unitless coefficient that enables the direct comparison of the length distribution of SWCNT samples regardless of their different L_{avg} values. We compiled the L_{avg}, L_l, and *LPDI* values of DOC-stabilized SWCNTs from different initial CSA concentrations in Table 1. A clear trend of increasing L_{avg} was observed as the SWCNT concentration in CSA decreases (Figure 3-2f). In addition, *LPDI* increased from 1.27 to 1.58, indicating that as the concentration of SWCNTs in CSA decreases, nanotubes of a wider range of lengths are stabilized as individual nanotubes during the S2E process.

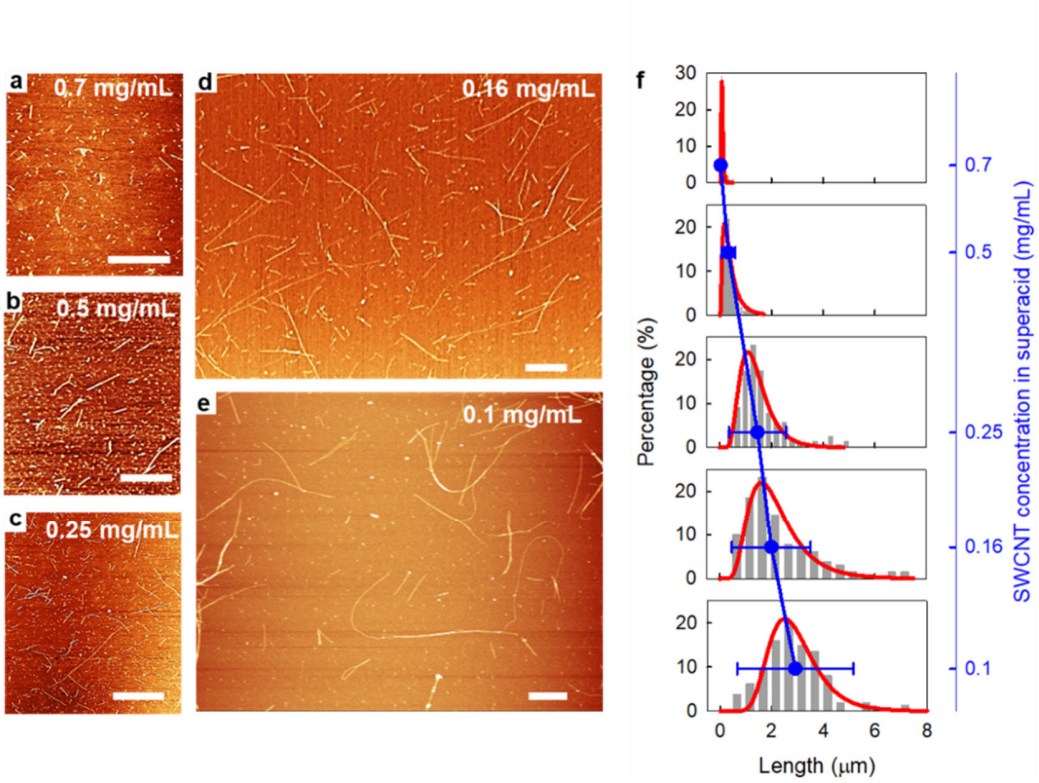

Figure 3-2. Length distribution of SWCNTs dispersed by S2E is highly dependent on SWCNTs concentration in superacid. (a-e) Representative AFM images and (f) corresponding length distributions (grey bars) of individual DOC-stabilized SWCNTs from decreasing SWCNT-superacid solution concentrations of ~0.70, ~0.50, ~0.25, ~0.16, and ~0.10 mg/mL, respectively. All scale bars are 1 μm. The distributions are fitted using log-normal functions (red lines). The average length of the DOC-stabilized SWCNTs increases as the concentration of SWCNTs in superacid decreases, as indicated by the blue line.

Table 1. Correlation of L_{avg}, L_l, and *LPDI* of SWCNTs stabilized in the aqueous phase by S2E with the SWCNT concentration in superacid.

	SWCNT concentration in CSA (mg/mL)				
	~0.70	~0.50	~0.25	~0.16	~0.10
L_{avg} (μm)	0.11	0.41	1.53	2.13	3.10
L_l (μm)	0.14	0.59	2.29	3.28	4.84
LPDI	1.27	1.44	1.50	1.54	1.58

3.3.2. Selectively Removal of Short SWCNTs by Iterative S2E Processes

The strong inverse correlation between SWCNT/CSA concentration with the L_{avg} of DOC-stabilized SWCNTs motivated us to selectively remove the shorter nanotubes by lowering the initial concentrations step-wise. Through repeated application of this self-sorting process, followed by separation of the bundled (longer nanotube) component, and subsequent re-dissolution of this precipitate in the CSA to repeat the process at a lower concentration, we were able to successively reduce the population of shorter nanotubes in the precipitated material (Figure 3-3a). SWCNTs were first dispersed at a high concentration (~0.7 mg/mL) so that only the shortest nanotubes were extracted from the bulk materials by the S2E process (defined as 1 cycle). The precipitates were then collected and re-dissolved into the CSA at a lower concentration. Applying the same S2E process again, a portion of slightly longer SWCNTs were removed (Figure 3-3b-e), further increasing the average length of the separated nanotubes. Since the overall length of the SWCNTs can be maintained throughout this iterative process, short nanotubes can be extracted repeatedly until a satisfactory long nanotube length is achieved.

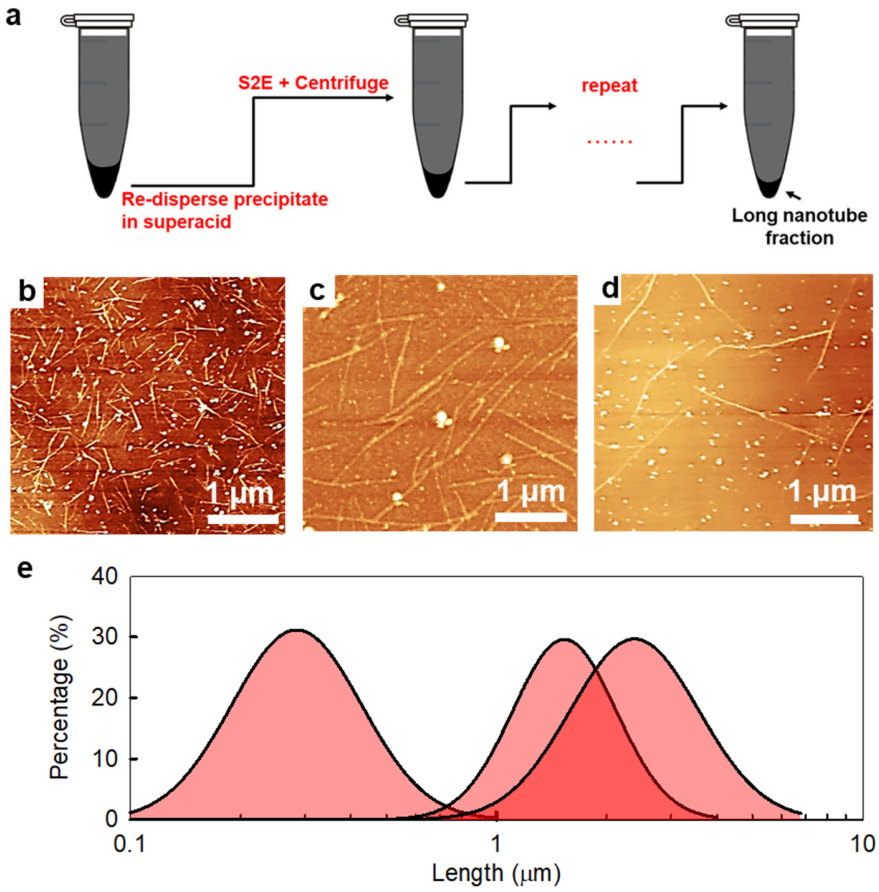

Figure 3-3. Selective extraction of short SWCNTs by iterative S2E processes. (a) Schematic illustration of iterative self-sorting of long SWCNTs. (b-d) Representative AFM images and (e) length distributions of the short DOC-stabilized SWCNT supernatant fractions from 2nd cycle at ~0.5 mg/mL (b), 3rd cycle at ~0.3 mg/mL (c) and 4th cycle at ~0.2 mg/mL (d) respectively.

Figure 3-4a-c shows representative AFM images of the sorted long tubes from the 2nd, 4th and 6th cycles of self-sorting. The removal of short nanotubes is clearly evident by the absence of nanotubes <1 μm in length. Moreover, the length distribution becomes progressively narrower (with a *LPDI* decreasing from 1.58 in the starting

material to 1.30, approaching the ideal limit of 1) while the corresponding L_{avg} values increasing to ~3.8 µm at the 6th cycle (Figure 3-4d). We note that a significant amount of ultralong nanotubes (>10 µm) can be easily found after 4 cycles. Figure 3-4e shows tiled AFM topography images of a ~12 µm ultralong SWCNT. Analysis of the AFM height profile unambiguously confirmed that it is an individual nanotube with a diameter of ~1.2 nm (Figure 3-4f). AFM images of additional ultralong SWCNTs (>10 µm) can be found in Figure 3-5.

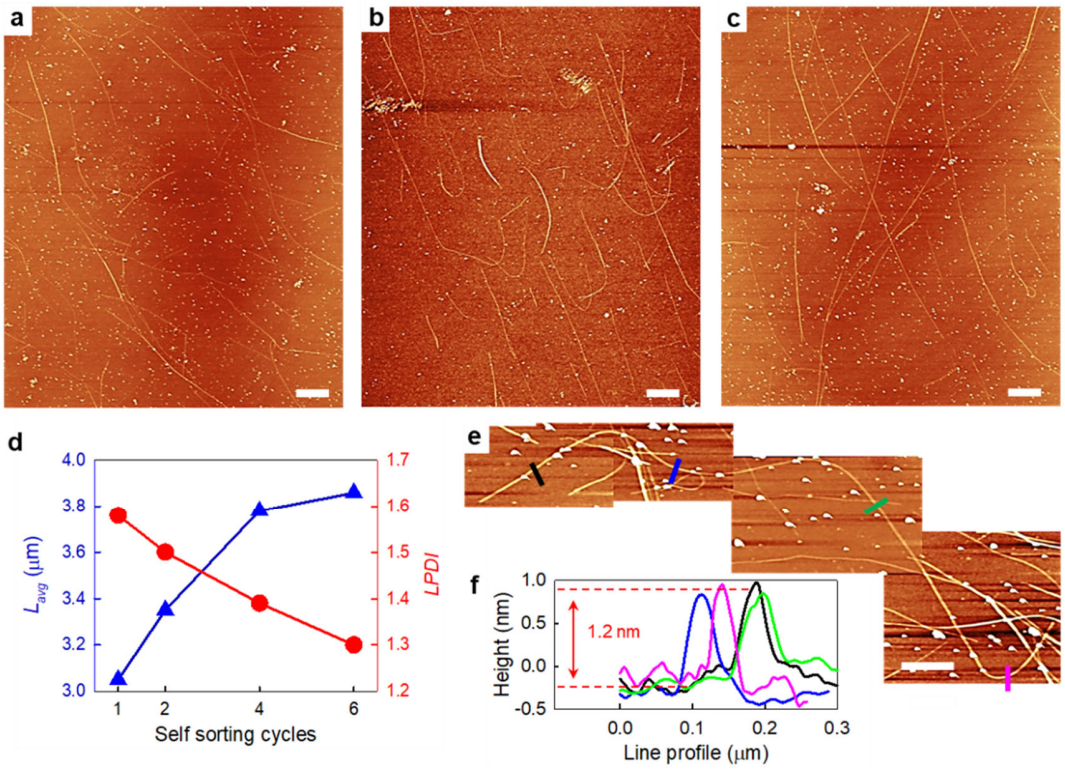

Figure 3-4. Length of SWCNTs can be progressively increased by iterative cycles of S2E processes. (a-c) Representative AFM images of individual, long SWCNTs separated after the 2nd, 4th, and 6th iterative S2E cycles. All scale bars are 1 µm. (d) The L_{avg} and *LPDI* of the extracted DOC-stabilized SWCNTs as a function of the self-

sorting cycles. (e) Tiled AFM images of a 12 μm long SWCNT. Scale bar: 1 μm. (f) Height profiles extracted along the nanotube, as marked in (e) by the black, blue, green, and purple lines.

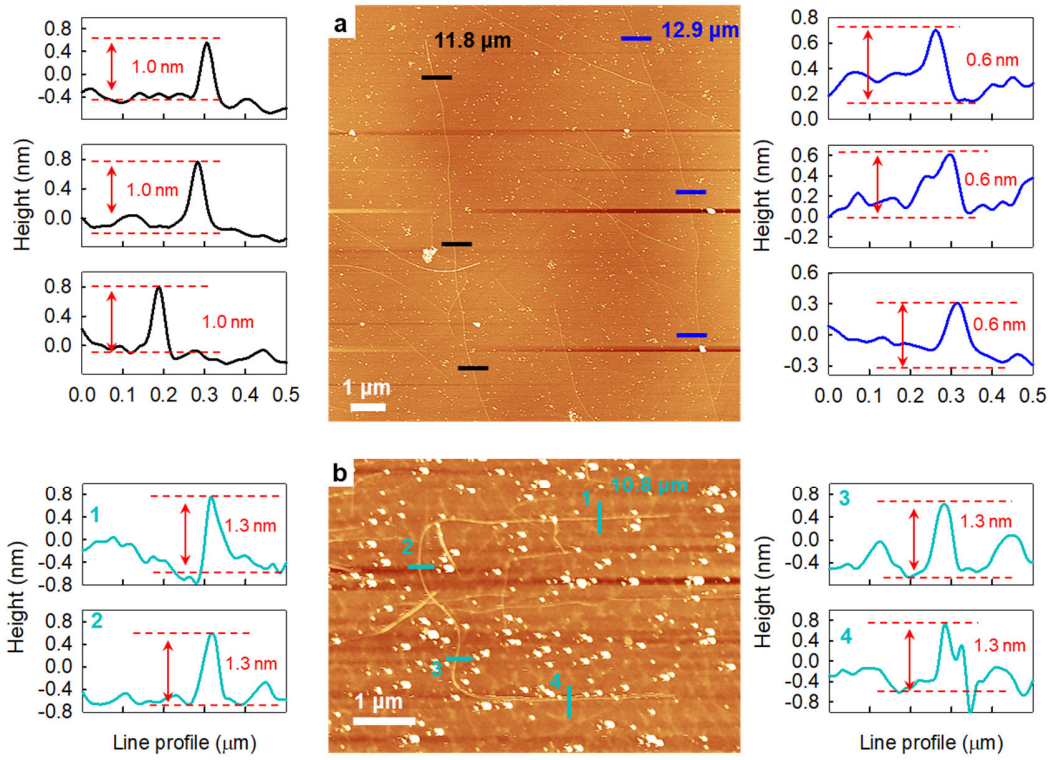

Figure 3-5. AFM images of ultralong SWCNTs (>10 μm). (a-b) Representative AFM images of three ultralong nanotubes after 4 self-sorting cycles, and the corresponding height profiles along the ultralong nanotubes (black, blue, and cyan) shown in (a) and (b).

3.3.3. Phase Behavior of SWCNTs in Superacid

We further confirmed the concentration-dependent phase behaviors by the cross-polarized microscopy (Figure 3-6a). Clearly, as the CSA concentration in the

superacid decreases from ~0.7 mg/mL to ~0.1 mg/mL, the relative proportions of the nematic and isotropic phases changes, and the birefringent liquid-crystalline structures disappear completely at φ_{iso} ~0.1 mg/mL. When SWCNT samples with polydisperse length are dissolved in the CSA at a sufficiently high concentration, shorter nanotubes stay as isotropic individual rigid rods while longer nanotubes assemble into nematic ordered phases (Figure 3-6b). Therefore, when neutralizing a SWCNT/CSA solution at a concentration above φ_{iso}, only short nanotubes that stay as isotropic individual rods can be effectively converted into DOC-stabilized SWCNTs by S2E. As the concentration of SWCNTs in CSA decreases, longer SWCNTs partition in the isotropic phase, and eventually with the same S2E procedure, they can be "captured" by the surfactant molecules and stabilized as individual nanotubes in aqueous solution. The fitting between L_{avg} with SWCNT concentration in CSA (c) yield an exponential relationship of $c \propto {L_{avg}}^{-0.76}$, which closely follows the prediction from Onsager's Theory ($c \propto {L_{avg}}^{-1}$, Figure 3-7). We note the L_{avg} of the pristine sample measured by capillary thinning extensional viscosity[76] is ~4.5 μm, which is ~45% longer than the L_{avg} of ~3.1 μm for the DOC-stabilized SWCNTs before length sorting. This discrepancy may be simply due to the approximations intrinsic in the extensional viscosity length determination, or may indicate that even at the optically dilute isotropic regime of ~0.1 mg/mL, ultralong tubes (>20 μm for instance) are still not well-stabilized by DOC molecules during the S2E process. Lowering the concentration of SWCNTs further in the CSA may allow the attainment of even longer SWCNTs by this self-sorting process.

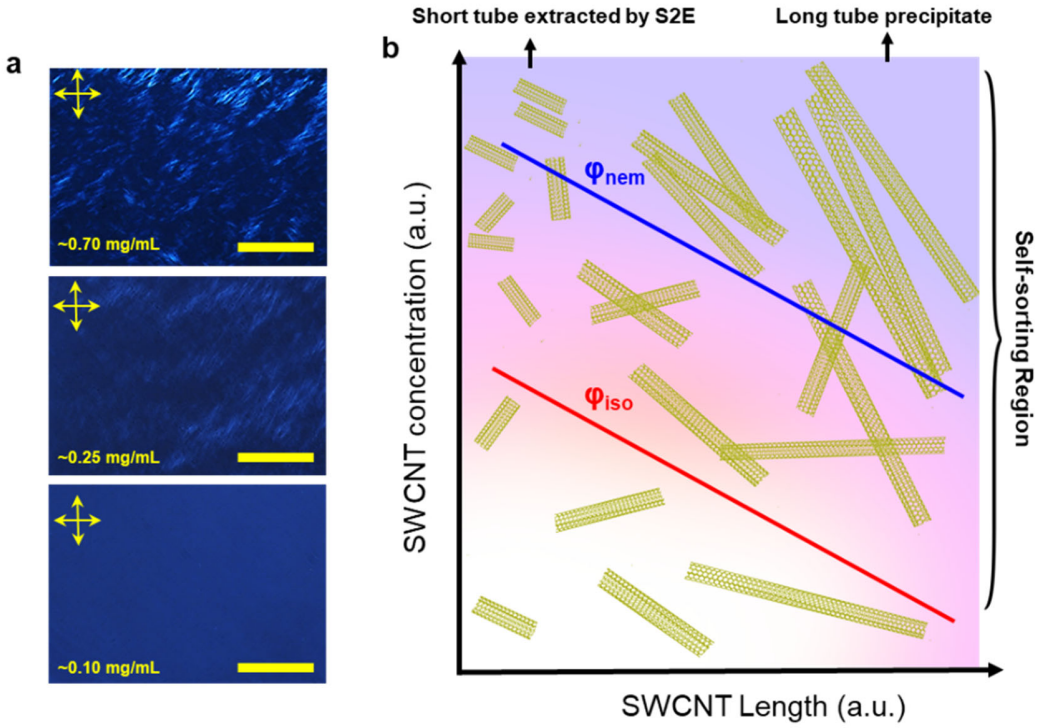

Figure 3-6. Phase behaviors of SWCNTs in superacid. (a) Polarized light microscopy shows the solution morphology of SWCNTs at different superacid concentrations. The cross arrows indicate the relative orientation between the polarizer and analyzer. Scale bars: 200 μm. (b) Phase behavior of SWCNTs in superacid solvent as a function of SWCNT length and concentration. The correlation of φ_{iso} and φ_{nem} with polydispersed SWCNT length are plotted according to the Onsager theory (axes are plotted in logarithmic scale). Above φ_{iso} the short tubes are selectively extracted by S2E while long tubes remain as bundles.

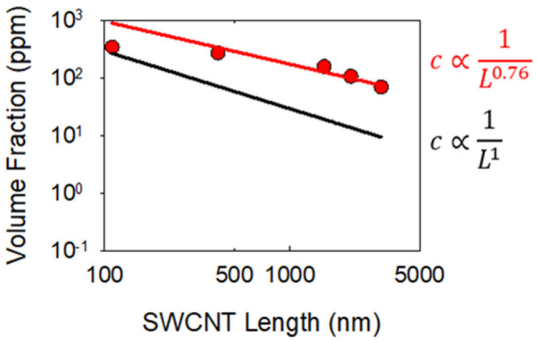

Figure 3-7: Comparison between the fitting of experimental data and the Onsager theory prediction. Fitting experimental data (red) yields an exponent of −0.76 with R=0.96, which is close to the Onsager theory's prediction of −1 (black).

Although our experiments unambiguously show that the observed "self-sorting" phenomena originate from nanotube phase separation in the CSA, directly centrifuging the SWCNT/CSA solution to separate the long nanotubes from the short ones does not work because the isotropic and nematic phases occur at very similar concentrations (about a factor of 1.5). Hence, the density difference and interfacial tension between the two phases are expected to be minimal. As a result, the small density difference would make it difficult to separate SWCNTs of different length at low centrifugal force, and the low interfacial tension would allow the two phases to mix during centrifugation.

3.3.4. Sorting Ultralong SWCNTs with Specific Properties and Their Applications in Thin Film Transistors

Because our long sorted S2E-SWCNTs are suspended in water, we can further purify the materials according to their electronic properties. We demonstrate this possibility by using the well-established aqueous two-phase (ATP) extraction method with minimum modifications.[43] Figure 3-8a shows a photo of three sorted fractions of long nanotubes with different chirality distributions, as indicated by the different colors of the solutions and their distinct UV-vis-NIR absorption spectra (Figure 3-8b). From the left to right in Figure 3-8a, the three solutions manifest different electronic properties and are categorized as metallic SWCNTs, large-diameter semiconducting SWCNTs, and small-diameter semiconducting SWCNTs. Photoluminescence (PL) microscopy was used to confirm the long length of the sorted semiconducting SWCNTs enriched fraction (Figure 3-8c).

To understand the influence of nanotube length and alignment on their macroscale electrical performances, we fabricated thin-film transistors from large-diameter semiconducting SWCNTs with different lengths and alignment, including aligned long semiconducting SWCNTs, random long semiconducting SWCNTs, and random short semiconducting SWCNTs (Figure 3-8d-f), in a back-gated configuration. Electrical transport characteristic curves and the plot of mobility *vs.* the current ON/OFF ratio of TFTs fabricated from different SWCNT films are shown in Figure 3-8g and Figure 3-8h, respectively. All TFTs showed similar p-type semiconducting behaviors with all ON/OFF ratios larger than 1000. However, TFTs fabricated from long aligned semiconducting SWCNTs show the highest mobility up to ~91 $cm^2 \cdot V^{-1} \cdot s^{-1}$ (average ~61.0 ± 15.6 $cm^2 \cdot V^{-1} \cdot s^{-1}$), while long random semiconducting SWCNTs and short random semiconducting SWCNTs exhibited much lower average mobilities of

30.1 ± 3.7 $cm^2 \cdot V^{-1} \cdot s^{-1}$ and 10.7 ± 2.4 $cm^2 \cdot V^{-1} \cdot s^{-1}$, respectively. To the best of our knowledge, the mobility from the long aligned semiconducting SWCNTs are among the highest values reported for SWCNT-based TFTs and is significantly higher than transistor devices made from soluble organic semiconductors (<1 $cm^2 \cdot V^{-1} \cdot s^{-1}$),[72] amorphous Si (~1 $cm^2 \cdot V^{-1} \cdot s^{-1}$) and nanocrystalline Si (~50 $cm^2 \cdot V^{-1} \cdot s^{-1}$),[73] even approaching that of p-type Si TFTs (~100 $cm^2 \cdot V^{-1} \cdot s^{-1}$).[74] The relatively low ON/OFF ratios (~1000-4000) of our multilayer thin-film devices can be explained by the charge screening effect, which is typically observed for relatively thick films of semiconducting nanotubes. Generally, the back-gate potential only has good control on the SWCNT-layer that is in contact with the dielectric. The charge carriers generated on this contact layer can screen the overlying SWCNT-layers, making it difficult for them to be fully turned off, resulting in higher off currents and lower ON/OFF ratio.[87, 88] This charges screen effect can be circumvented by decreasing the film thickness. We therefore fabricated TFTs comprising a sub-monolayer of long random semiconducting SWCNTs. The ON/OFF ratio was increased up to ~22000 while the mobility remained at ~50 $cm^2 \cdot V^{-1} \cdot s^{-1}$ (Figure 3-9). Strategies for further improving the ON/OFF ratio include using SWCNTs with larger bandgaps,[87] using single-chirality semiconducting SWCNTs[89] or using high-κ dielectric materials.[88] Our study here shows that with long semiconducting SWCNTs as the channel material for long-channel TFTs, the mobilities of charge carriers can be improved by more than 10 times, demonstrating the significant influence of SWCNT-length on the performance of SWCNT-based TFTs.

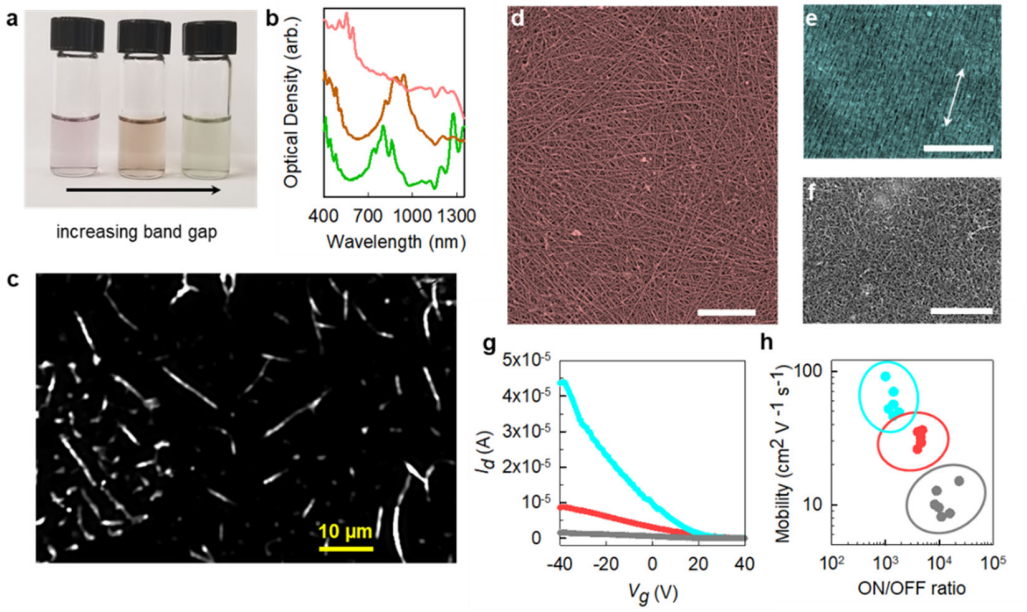

Figure 3-8. Sorting of long semiconducting SWCNTs and their applications in TFTs. (a) A photograph of aqueous solutions of chirality-sorted SWCNTs with increasing bandgaps by ATP. (b) UV-vis-NIR absorption spectra of the 3 solutions shown in (a). (c) A broadband (900–1600 nm) PL image of the sorted semiconducting DOC-stabilized SWCNTs. d-f) False-color SEM images of thin films fabricated from (d) random, long semiconducting SWCNTs, (e) aligned, long semiconducting SWCNTs, and (f) random, short semiconducting SWCNTs. All scale bars are 500 nm. (g) Electrical transport characteristic curves and (h) mobility *vs.* the current ON/OFF ratio of thin film TFTs fabricated from the random, long semiconducting SWCNTs (red, d), aligned, long semiconducting SWCNTs (cyan, e), and random, short semiconducting SWCNTs (grey, f).

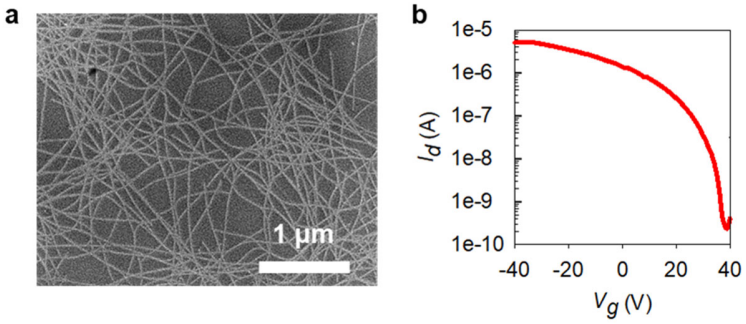

Figure 3-9. TFTs based on a submonolayer of random long semiconducting SWCNTs. a) SEM images showing a submonolayered network of random long semiconducting SWCNTs. The scale bar is 1 µm. b) Transfer characteristics of the corresponding TFT in a logarithmic scale.

3.4. Conclusions

In conclusion, we demonstrate that ultralong SWCNTs can be self-sorted by exploiting their length-dependent phase partitioning in solution, which depends on nanotube length. We obtained an L_{avg} ~3.8 µm with a narrow length distribution (*LPDI* = 1.30), with a significant fraction of ultralong SWCNTs longer than 10 µm. We further sorted SWCNTs with different lengths into semiconducting and metallic fractions using aqueous two-phase extraction. TFTs fabricated from the long semiconducting nanotubes show ON/OFF ratios greater than 1000 and a significant improvement of carrier mobilities up to ~90 $cm^2 \cdot V^{-1} \cdot s^{-1}$, well-exceeding those of short semiconducting SWCNTs, organic semiconducting polymers or polycrystalline silicon. Our approach provides a pathway to attain ultralong SWCNTs with defined electrical properties, opening opportunities to significantly improve the transport properties and performance of SWCNT-based devices, such as TFTs and sensors.

4. Extraordinary Electromechanical Properties of Long Metallic Double-Walled Carbon Nanotubes

This chapter is adapted from a published manuscript.[90]

Wang, P.; Peng, Z.; Li, M.; Wang, Y. *Small*, **2018**, 14(38): 1802625

P.W. and Z.P. contributed equally to this work. Y.W., P.W. and Z.P. conceived and designed the experiments. P.W. and Z.P. performed the major experiments. Z.P. and M.L. performed the DGU sorting. Y.W., P.W., and Z.P. wrote the manuscript with inputs from all authors.

This work was partially supported by AFOSR (FA9550-16-1-0150) and NIH/NIGMS (R01GM114167). AFM images were obtained using a shared system supported by the NSF MRI program (CHE1626288).

4.1. Introduction

The extraordinary collective properties from long CNTs can be demonstrated in the applications of stretchable transparent conductive films (STCFs).

STCFs can accommodate various configurations on arbitrary surface geometries, leading to intimate contact with objects of different shapes.[91] Such mechanical flexibility is crucial for overcoming the physical mismatch between soft/elastic biological materials and stiff microelectronics. Recent advancements in STCFs have initiated a number of exciting applications, such as epidermal body sensors,[92] implantable retinal prostheses,[93] and electrophysiology/neuro-imaging devices.[94] Benefitting from higher electrical conductivity, optical transparency, and mechanical stretchability, STCFs can also help build revolutionary applications, like bionic contact lenses, which could potentially superimpose data and information with real vision, thus creating an enhanced reality that could fundamentally change the way humans perceive and interact with the world.

The major hurdle for further advancement of STCFs, however, has been finding materials that can simultaneously achieve high conductivity (> 1000 S/cm) and transparency (> 85%) under large tensile strain (> 100%). One of the most common approaches to fabricating STCFs is by compositing functional electronic materials with soft substrates.[91] Currently, conductive polymers, metallic nanostructures, and low-dimensional carbon-based nanomaterials have been successfully proposed as "rigid conductors" for the fabrication of STCFs in combination with elastic polymers.[91] Conductive polymers are inherently flexible and simple to prepare and process, but their intrinsic conductivity is usually low (< 550 S/cm at zero tensile strain).[95] Instability caused by environmental factors (e.g., humidity, UV light, and elevated temperature) remains another concern. Micro-sized metals with various structures (e.g., thin films, grids, and nanowires) show excellent electrical performance, but such structures easily delaminate from elastomer substrates at high tensile strain, resulting in quick conductivity decay.[96] The hazy appearance of these materials due to their relatively large diameter (~50 nm) also deteriorates the overall optical transparency.[97] Two-dimensional carbon materials, such as graphene, feature superior conductivity and transparency (> 5000 S/cm at 85% transmittance) when tensile strain is absent, but readily crack into pieces at less than 5% strain since their carbon-carbon bonding network cannot provide an energy dissipation mechanism to the externally applied force.[98, 99]

1D nanocarbon material such as CNTs are among the most promising candidates for high-performance STCFs. When fabricated into films, CNTs readily assemble into percolating networks that remain intact even at high tensile strain due to

the high mechanical strength of these materials (Young's modulus on the order of 1 TPa, as compared to 0.2 TPa for steel).[13] Additionally, the collective van der Waals interactions between entangled nanotubes (~0.5 eV/nm for 1.4 nm diameter nanotubes) are much stronger than those from micron-sized 1D metal nanowires, allowing reconfiguration within the CNT network in response to the mechanical strain to avert delamination. Also, CNT films feature high transparency and neutral color, since the small diameter of CNTs can significantly reduce the degree of light scattering and haze effect compared with other 1D metal nanowires.[24] Lastly, recent breakthroughs in mass production (up to 10 tons per year) of high quality CNTs (OCSiAl's Tuball tubes feature a G/D ratio >100) had decreased the cost down to $1 per gram, making CNTs even more competitive than precious metal nanowires or graphene, which is still limited to laboratory-scale production.

Despite the superior flexibility and transparency of CNT-based STCFs, however, a large obstacle is the overall low conductivity of the CNT thin films. While individual CNTs can be extremely conductive, the highest electrical conductivity of macroscale networks formed from raw CNT materials is usually less than 4% of the inherent conductivity of an individual tube.[24] This low conductivity is due to the large junction resistance (R_j) between different CNTs. Moreover, raw CNTs are typically synthesized as a polydisperse material that contains both semiconductors and metals, further hampering the use of CNTs as conductive materials.

To alleviate the impact of tube-tube junctions and electron scattering sites on the film conductivity, two strategies can be employed: (1) lowering the average junction resistance; and (2) decreasing the number of junctions. In general, junction

resistances are much smaller between metallic tubes than their heterogeneous counterparts, which has motivated the development of advanced purification techniques, such as DGU and ATP to enrich samples with metallic nanotubes. Additionally, the longer the CNT, the fewer junctions that are encountered by electrons traversing the fabricated thin films. While methods of growing CNTs with increased lengths have been reported, current large-scale fabrication of CNT-based STCFs (such as roll-to-roll processing) typically requires an initial step of dispersing the CNTs into aqueous solution using ultrasonication to overcome the strong van der Waals interactions within the CNT bundles. The sonication process, however, inevitably introduces defects and cuts the CNTs into shorter fragments, which is a major issue for further improving the overall conductivities of CNT-based STCFs. To this end, long and metallic CNTs are desirable for high performance devices.

Here, by compositing full-length metallic outer-walled double-walled carbon nanotubes (m-DWCNTs) as electrical conductors on a polydimethylsiloxane (PDMS) substrate, we successfully fabricated CNT-based STCFs achieving high electrical conductivity (> 1000 S/cm) and high optical transmittance (> 85%) at over 200% tensile strain. DWCNTs were chosen in this work because previous studies have shown that they are the best type of CNT for high electrical conductivity applications.[100, 101] This is because as the wall numbers increase, individual tubes become more electrically conductive due to the electronic coupling effects between walls, however, the packing density (i.e., number of CNTs per unit area) in the thin film also decreases. Therefore, the electrical conductivity peaks when the average wall number is approximately two. Long m-DWCNTs were prepared using S2E method to first disperse long, raw

nanotubes into aqueous solution, followed by subsequent DGU purification to enrich the metallic nanotubes.[102] Since no sonication is necessary in this CNT-dispersion and enrichment process, the sorted m-DWCNTs feature an average length of ~3.2 μm, which is substantially larger than the sonication control (~0.8 μm on average). Benefiting from this nondestructive process, the fabricated STCFs showed excellent conductor performance. When stretched to 100% tensile strain, 3.2 μm long m-DWCNT STCFs exhibited a record high conductivity of up to 3316 S/cm at 100% tensile strain and 85% optical transmittance, which is 194-times higher than that of 0.8 μm short nanotube controls. Moreover, extraordinary electrical stability under prolonged cycles of stretching and release was also observed. After 1000 stretch-release cycles (between 100% to 0% tensile strain), the conductivity of the long m-DWCNT STCFs decayed by just 4%. In contrast, STCFs based on short m-DWCNTs experienced a significant decay of over 89% after the same stretching/releasing protocol. Electron microscopy studies revealed that microscale gaps formed in DWCNT films induced by stretching were effectively bridged by the long nanotubes, which kept the electrical pathways intact throughout the thin film.

Lastly, as a proof of concept to demonstrate the device's use as a flexible conductor, we mounted a 3.2 μm long m-DWCNT STCF on a subject's finger, and demonstrated how it can provide a stable electrical current path despite the curling movement of the digit. In contrast the 0.8 μm short control demonstrated large electrical current change in response to the finger's movement, suggesting the material's use for sensitive motion sensors. Our results reveal the significant impact of the size of

nanoscale components on device performance and pave the way for the application of low-dimensional carbon materials in future flexible electronics.

4.2. Experimental Section

4.2.1. Dissolution of Full-Length DWCNTs in Aqueous Solution

2 mg of raw DWCNT powder (CheapTubes Inc.) was mixed with 10 mL chlorosulfonic acid (Sigma Aldrich, 99.9%) and stirred using a magnetic stir bar overnight so that the DWCNTs were fully dissolved. The S2E procedures are identical as previous described in Section 3.

4.2.2. Separation of metallic-DWCNTs by DGU

DGU separation of m-DWCNTs was performed using an Optima XE-90 ultracentrifuge (Beckman Coulter). A linear density gradient was first formed in an open-top polyclear centrifuge tube (Seton) containing homogeneous 0.4% w/v sodium cholate and 0.6% w/v sodium dodecyl sulfate surfactant loading. The density gradient, with water as solvent, consisted of a 1.5 mL underlayer containing 60% w/v iodixanol (Sigma Aldrich), followed by a 5 mL linear gradient with a concentration ranging from 40 to 25% w/v iodixanol generated from a gradient maker (Hoefer SG15). After that, a 1 mL layer of the S2E dispersed DWCNT solution containing 20% w/v iodixanol was added on top of the linear gradient. ~4 mL of 0% w/v iodixanol solution was finally added to fill the tube. The gradient solutions were then ultracentrifuged for 15 h at a rotational frequency of 40000 rpm in a SW41 Ti rotor (Beckman Coulter). Following DGU, the sorted materials were extracted using a piston gradient fractionator (Biocomp Instruments) into ~100 μL fragments for later characterization.

4.2.3. Spectroscopic and Microscopic Characterization

The UV-vis-NIR absorption spectra of the DWCNT solution before and after DGU purification were measured using a Lambda 1050 (Perkin Elmer) spectrometer equipped with a broadband InGaAs detector. To measure the transmittance of the STCFs, an integrating sphere (Labsphere Model No. 150MM RSA ASSY) equipped with a broadband InGaAs detector installed in the UV-Vis-NIR spectrophotometer was also used. A LabRAM ARAMIS Raman microscope (Horiba Jobin Yvon) was used to measure to Raman scattering of the DWCNTs before and after DGU sorting. SEM and TEM images were collected with a SU-70 SEM (Hitachi) and a JOEL FEG TEM, respectively.

4.2.4. DWCNT Length Characterization

DWCNTs before and after DGU purification were deposited on (3-aminopropyl) triethoxysilane functionalized Si/SiO_2 substrates. The coated wafers were annealed in air at 300 ˚C for 15 min so that the surfactants and other possible organic solvents could be removed. All AFM images were recorded in tapping mode on a Cypher ES AFM (Asylum Research Corporation) with conical AFM probes backside-coated with gold (Tap300GD-G, with a force constant of 40 N/m, Ted Pella).

4.2.5. Fabrication and Characterization of Stretchable Transparent Conductive Films

Dispersed DWCNTs were filtered through a 0.025 μm nitrocellulose membrane (Merch Millipore Ltd) to form light grey thin films of various thicknesses The PDMS films were fabricated by spin coating the mixture of precursor and Sylgard 184 (Dow Corning) at a ratio of 10:1 on a glass substrate at 500 rpm and cured at 80 ˚C for 8 h. Prior to transferring the DWCNT thin films onto the PDMS substrate, the PDMS films

were treated with 20 min UV-Ozone (ProCleaner^{TM} Plus, Bioforce Nanosciences) with a UV intensity of 19.4 mW/cm^2 to increase the adhesion between the DWCNTs and the PDMS. The DWCNTs along with the filtration membrane were compressed onto the PDMS/glass substrate by applying force and annealed at 90 ºC for 1 h. Overnight acetone vapor bath at 105 ºC followed by acetone rinsing were used to totally dissolve and remove the filtration membrane. The PDMS/DWCNTs thin film were then peeled off with a razor blade from the glass substrate. Four Ag electrodes were deposited on the as-fabricated STCFs using a Metra Thermal Evaporator in order to facilitate the measurement of the electrical conductivities. A high-speed camera was used to monitor the length and width change of the PDMS/DWCNT composites during the stretching process. AFM was used to measure the film thickness and a thickness-optical transmittance curve is plotted in Figure S8. For fabricating STCFs for human motion sensor applications, the overall procedure was identical except the PDMS precursor was spin coated on glass substrates at 4000 rpm so the thinner STCFs that were produced could adhere to the human body better. Electrical measurements were carried out using an HMS-5000 semiconductor parameter analyzer and a Biologic SP-200 potentiostat. Mechanical tensile strain tests were performed on a Shimazu Autograph AGS-X tensile tester.

4.3. Results and Discussion

4.3.1. Separation of Long m-DWCNTs

Figure 4-1 schematically describes the steps for fabricating STCFs from long m-DWCNTs, including the dissolution of full-length DWCNTs in aqueous solution using our S2E method, the subsequent purification of m-DWCNTs by the DGU

technique, and finally integration of the materials on a PDMS substrate. DWCNTs are dissolved in superacid, which is further exchanged to DOC as the superacid-DWCNT solution is added drop-by-drop into a basic aqueous solution containing the surfactant. The end result is a homogeneous aqueous solution of individual DWCNTs stabilized by DOC. Since there is no sonication-induced cutting, the dissolved DWCNTs maintain their full lengths, which cannot be achieved when sonication is used to disperse the materials. After simple solution-based mixing and filtration steps to concentrate the DWCNTs and remove the salt generated from the neutralization step, the obtained DWCNT-DOC aqueous solution can be readily used as the parent material for advanced purification by the established DGU method.

DGU purification relies on the different buoyant densities of various types of CNTs wrapped by surfactant molecules. Under a strong centrifugal force, the CNTs will reside in different layers of gradient media that match their buoyant densities. We adopted this DGU method and further modified it to differentiate the electronic type of our S2E DWCNTs by using a co-surfactant system, eventually realizing the separation of m-DWCNTs from single-walled CNTs (SWCNTs) and semiconducting outer-walled DWCNTs (Figure 4-1). Finally, we filtered the sorted m-DWCNTs to fabricate thin films, which were then transferred onto flexible UV-ozone activated PDMS substrates to test the samples' electrical properties under various stretching conditions. As controls, DWCNTs were dispersed by a conventional sonication method and sorted by the same DGU procedure to produce short m-DWCNTs, which were also prepared and fabricated into STCFs for comparison.

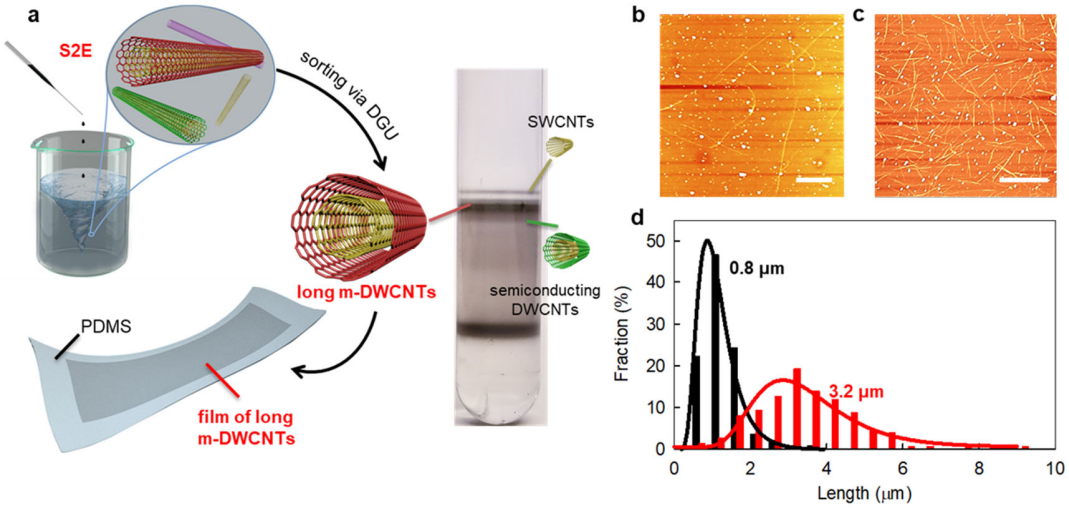

Figure 4-1. Preparation of long m-DWCNTs. (a) Schematic of the fabrication of flexible, transparent, conductive m-DWCNT thin films on PDMS from full-length m-DWCNTs. A photograph of a centrifuge tube following the DGU separation of a S2E-DWCNT solution is shown. Representative AFM topography images of m-DWCNTs prepared by (b) S2E and (c) sonication. Scale bars: 1 μm. (d) Length distribution of long m-DWCNTs (red) and the short sonication control (black).

We first confirmed the enrichment of m-DWCNTs after S2E dispersion and DGU purification by optical absorption and Raman scattering measurements. Figure 4-2a shows an ultracentrifuge tube after DGU sorting of the S2E-DWCNTs, which features distinct layers that indicate the enrichment of SWCNTs, m-DWCNTs, and semiconducting DWCNTs from top to bottom, respectively. UV-Vis-NIR spectra from each extracted fraction (Figure 4-2b) unambiguously demonstrates such assignments: the top fraction showed distinct peaks from 900 to 1350 nm, representing the E_{11} optical transition of SWCNTs; the middle fraction showed broad absorption between 700 and 900 nm, representing the M_{11} optical transition of m-DWCNTs; and the bottom fraction

exhibited absorption between 900 and 1300 nm, representing the S_{22} optical transition of semiconducting DWCNTs. Resonant Raman spectra (Figure 4-2c,d) along with transmission electron microscopy (TEM) images (Figure 4-3) further demonstrated the separation of SWCNTs, m-DWCNTs, and semiconducting DWCNTs after DGU. Because of the aqueous solution-based nature of the S2E dispersion process, other aqueous separation methods that are less expensive with higher loading, such as aqueous two-phase extraction and gel chromatography, may also be employed to obtain purified long m-DWCNTs as the starting material for the following experiments.

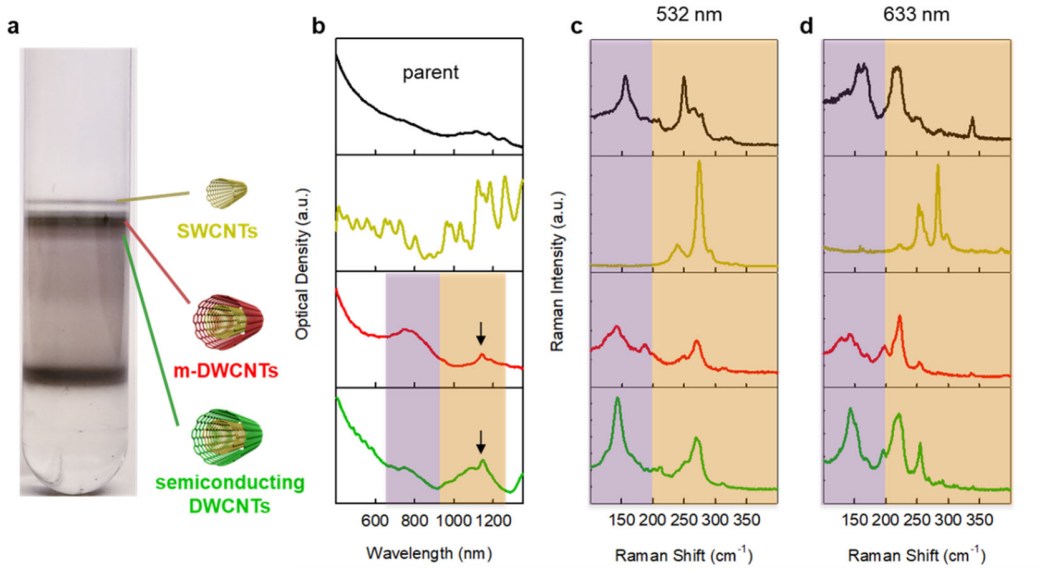

Figure 4-2. Sorting of m-DWCNTs by DGU. (a) A photograph showing a centrifuge tube after DGU separation of the S2E DWCNT solution. The distinct layers from top to bottom can be attributed to SWCNTs, m-DWCNTs, and semiconducting outer-walled DWCNTs. b) The UV-vis-NIR spectra of the separated fractions. The Raman spectra of the RBMs at c) 532 nm laser excitation and d) 633 nm laser excitation of the

parent, SWCNTs, m-DWCNTs, and semiconducting outer-walled DWCNTs, from top to bottom.

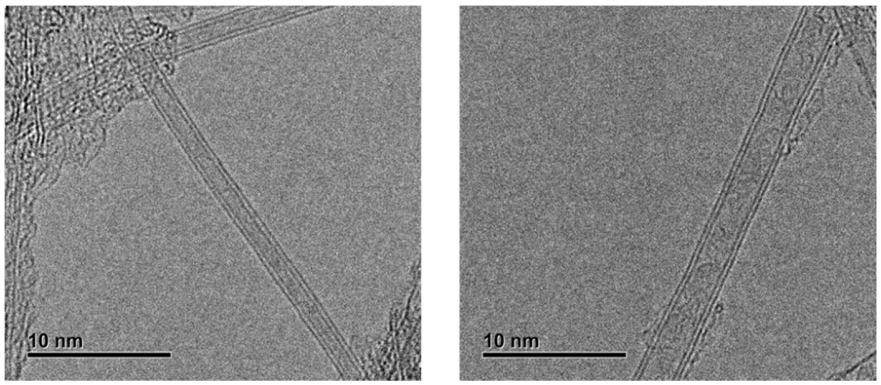

Figure 4-3. Representative TEM images of DGU-sorted long m-DWCNTs.

AFM was then used to characterize the length distribution of the sorted m-DWCNTs. Figure 4-1b,c shows the representative AFM images of the m-DWCNTs from S2E and m-DWCNTs from sonication as the control, respectively. While the m-DWCNTs from sonication featured an average length of 0.8 μm, in substantial contrast the S2E m-DWCNTs reached an average length of 3.2 μm, which is 4-times longer (Figure 4-1d). Thus, the successive S2E-DGU process proves to be an efficient way of preparing enriched m-DWCNT solutions with maintained nanotube length, which will benefit subsequent device fabrication and performance.

4.3.2. Stretchable Transparent Conductive Films from Long m-DWCNTs

The long purified 3.2 μm m-DWCNTs were then used to fabricate thin films of various thicknesses by the filtration method and subsequently transferred onto flexible PDMS substrates for STCF fabrication. The electrical conductivity of the fabricated

STCFs were then *in situ* monitored under tensile stress. Figure 5-4a and 5-4b show the conductivity as a function of tensile strain for STCFs fabricated from 3.2 μm long m-DWCNTs and 0.8 short μm m-DWCNTs, respectively, at different transmittances (i.e., film thicknesses). Despite the distinct initial conductivities, all the long m-DWCNTs STCFs of different transparency showed extremely stable and high conductivity under large tensile strain. For example, the conductivity of the STCF at 85% transmittance monotonically increased from an initial conductivity of 1651 S/cm to the maximum value of 2122 S/cm when stretched to 32%, possibly due to the strain-induced alignment of DWCNTs along the stretching direction, which will be discussed later. Further stretching to 100% strain decreased the conductivity by only 1.8% to 1651 S/cm. Even at 285% tensile strain when the PDMS broke, the conductivity was still maintained as high as 953 S/cm. In contrast, STCFs fabricated from short m-DWCNTs not only showed much lower initial conductivities due to the short length of the tubes and thus overall high junction resistance, but also manifested pronounced conductivity decay even under minimal tensile strain (< 10%), resulting in a conductivity of less than 30 S/cm at 100% tensile strain, which is inadequate for stretchable electronics applications (Figure 4-4b).

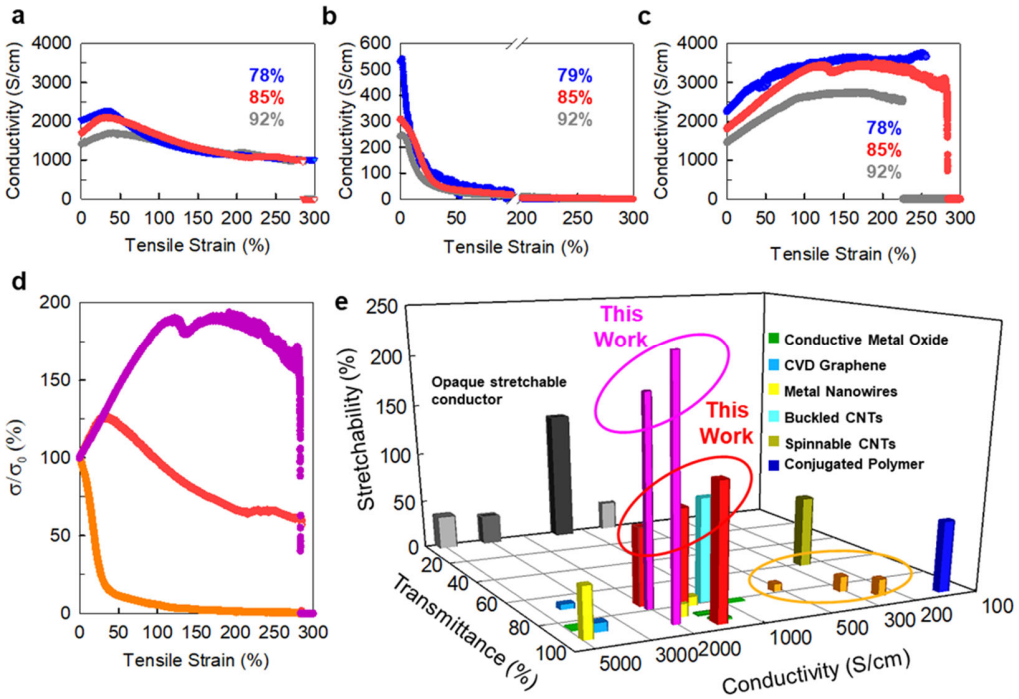

Figure 4-4. Electrical conductivity versus tensile strain profiles of STCFs fabricated from (a) 3.2 μm long m-DWCNTs, (b) 0.8 μm short m-DWCNTs, and (c) 3.2 μm long m-DWCNTs on pre-stretched PDMS substrates at various transmittances. Numbers in a-c indicate the transmittance of different films. (d) Normalized conductivity-tensile strain curves of STCFs made from long m-DWCNTs (red), short m-DWCNTs (orange), and pre-stretched long m-DWCNTs (purple) at 85% transmittance. (e) Comprehensive comparison of conductivity, transmittance, and stretchability of STCFs made from long m-DWCNTs (red), short m-DWCNTs (orange), and pre-stretched long m-DWCNTs (purple) with other reported values.

To further increase the mechanical tolerance of STCFs, long m-DWCNTs were deposited onto PDMS substrates that were pre-stretched to 100% tensile strain (Figure 4-4c). At 85% transmittance, the conductivity increased from an initial value of 1809

S/cm at 0% strain to 3316 S/cm at 100% tensile strain and 2425 S/cm at a maximum 285% tensile strain. To the best of our knowledge, 2425 S/cm at maximum tensile strain is the record high conductivity for flexible transparent conductive films. We also plotted the normalized conductivity (σ/σ_0) versus tensile strain profile for long m-DWCNT, short m-DWCNT, and pre-stretched long m-DWCNT STCFs at the same transmittance (85%) in Figure 4-4d to better show the distinct electromechanical responsive behaviors of these devices. The comparison unambiguously demonstrated the superior mechanical tolerance of longer nanotube-based STCFs (whether pre-stretched or not) compared to those made from shorter tubes. Notably, in our previous work we demonstrated that the high conductivity of thin films from S2E-processed CNTs was not the result of doping, which is a commonly used way to increase the conductivity of CNT-based conductive films. Therefore, such STCFs would be an ideal candidate for conductor applications since doped films are not stable and will lose conductivity over time. Figure 4-4e further provides a comprehensive comparison of the fabricated STCFs from 3.2 μm long m-DWCNTs with previous reported conductors using different conducting materials[92, 103-109] to showcase the clear advantage of long m-DWCNTs based STCFs in achieving high performances in all three critical parameters: optical transmittance, electrical conductivity, and mechanical stretchability. To make the comparison more reasonable, we define the stretchability as the tensile strain at which the conductance decreases by 50% (or resistance increases by 200%) of the initial value. Clearly, the conductivity and transmittance of CVD-grown graphene, metal nanowires, and metal oxide materials, such as indium tin oxide, can be very high (> 1000 S/cm), however, most of their stretchabilities are less than

20%. Spinnable CNTs and conjugated polymers can reach a stretchability of more than 70% but their overall conductivities are less than 250 S/cm. Printing conductive ink from Ag flakes or conductive polymers with ionic additives can generate high conductivity (> 1500 S/cm) and modest stretchability (> 50%), however, the opaque nature of these inks prevents their use as transparent flexible conductors (films composed of transparent elastomer substrates with printed opaque lines cannot be categorized as "true" STCFs since their inhomogeneous conductive nature prevents their use in applications such as bionic contact lenses). Long m-DWCNT thin films by simultaneously combining high transmittance (> 85%), high conductivity (> 1000 S/cm), and high stretchability (> 90%) unambiguously outperformed all other reported conductors. Furthermore, the pre-stretching strategy can further enhance the stretchability of the long m-DWCNTs STCFs to ~200% while maintaining superior transmittance and conductivity. Note that the long m-DWCNTs used here are sorted only by the electronic type of the outer-wall through DGU, many of which contain semiconducting inner tubes that can deteriorate the overall conductivity of STCFs. Therefore, further enhancement of conductivity may be achieved by using sorted DWCNTs with metallic inner and outer tubes.

4.3.3. Electrical and Electromechanical Properties from Long m-DWCNTs

In order to evaluate the durability and reversibility of m-DWCNT STCFs, we used a homemade dynamic mechanical analyzing system to monitor the resistance change of the films over prolonged stretching-releasing cycles. The resistances of the STCFs at 0% (released state) and 100% (stretched state) tensile strain were measured

(Figure 4-5a) and plotted in cycling profiles (Figure 4-5b–e). The long m-DWCNT STCFs exhibited an extremely stable resistance profile with only 4% increase of the initial value after 1000 stretching/releasing cycles, corresponding to only ~0.004% conductance loss per cycle. In sharp contrast, after 1000 stretching/relaxing cycles, at the released state, the resistance of the short m-DWCNT STCF increased by 19-fold, representing ~0.095% conductance decay per cycle. Therefore, the durability of STCFs made from long tubes is ~23.7-times better than that from short tubes. An abrupt resistance change ($R/R_0 > 10^5$) in short m-DWCNT thin films was observed after 100 cycles, which can be explained by the accumulation of "permanent gaps" throughout the film generated after each cycle (see later discussions).

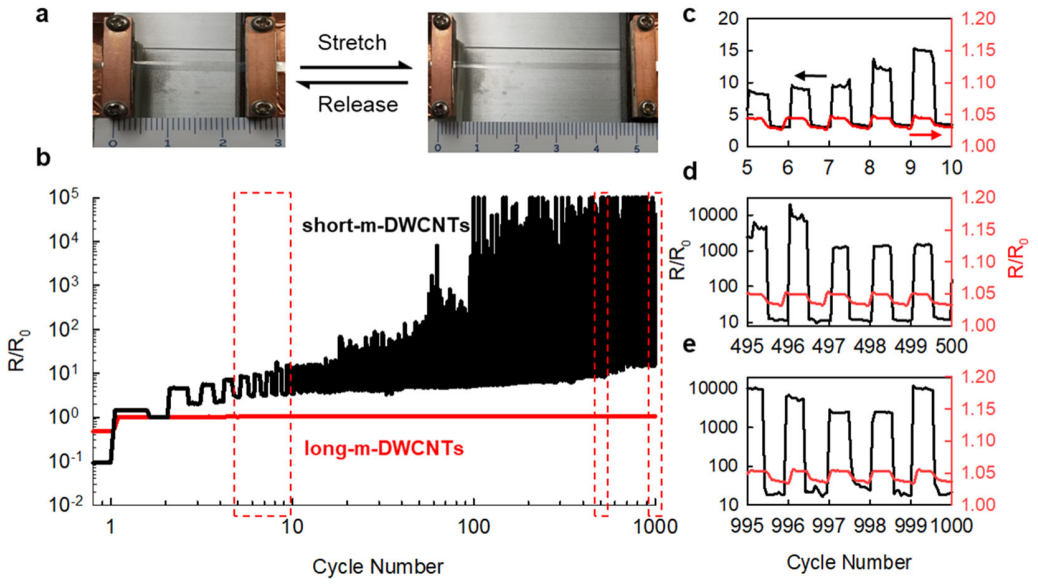

Figure 4-5. (a) Photograph of an STCF under released (0% tensile strain) and stretched (100% tensile strain) states. (b) Relative resistance changes of long m-DWCNT (red) and short m-DWCNT (black) STCFs under long term stretching-releasing cycles. (c),

(d) and (e) are zoomed-in relative conductivity profiles for the stretching-releasing cycles of 5 to 10, 495 to 500, and 995 to 1000, respectively.

To fully understand the length dependent distinct electromechanical responses, scanning electron microscopy (SEM) was used to study the surface morphology of these devices under different strains. Initially, DWCNTs of both short and long lengths assembled into uniform thin films on the top of the PDMS substrate with isotropic orientations (Figure 4-6a,e). For STCFs comprised of short m-DWCNTs, when applied with 50% strain, nano-sized gaps began to emerge within the thin film (Figure 4-6b), and further stretching to 100% strain caused the gaps to enlarge to a few hundred nanometers. At this point, the thin film was lacerated into different "patches" (Figure 4-6c). After the strain was released, the relaxation caused some gaps to recombine together while others stayed permanently open (Figure 4-6d). On the other hand, thin films made from long m-DWCNTs exhibited a completely different surface morphology change with added stress. At 50% tensile strain, although some nano-sized gaps were also generated, the main phenomenon we observed was the stress-induced tube-alignment parallel to the stretching direction (Figure 4-6f). When stretched to 100% strain, gaps of a few hundred nanometers appeared, but in comparison to the short m-DWCNT sample, the long m-DWCNTs were able to successfully bridge these gaps (Figure 4-6g). After releasing the strain, the long tube bridges formed "wavy structures" across these gaps (Figure 4-6h). We assume the main reason causing these phenomena is the mismatch of flexibilities between the DWCNT thin films and the PDMS substrate. Briefly, CNT thin films tend to stretch with the UV-ozone activated

PDMS because of strong adhesion force, but their low elasticity compared with PDMS induces breakages across the thin films. Since long tubes can successfully bridge the gaps between different "patches" within the film, active percolating electrical pathways are therefore maintained. In comparison, gaps generated upon stretching the long m-DWCNT STCFs could not be bridged due to the short length of the sonicated tubes, consequently resulting in the fragmentation of electrical pathways and a significant deterioration of conductivity. When the strain is released, some "patches" in the short m-DWCNT STCFs come into contact again to partially resume the electrical connections, but more were permanently disconnected, leading to overall degraded conductivity. As for the long m-DWCNT STCFs, since most electrical pathways were maintained across the gaps during the strain-relaxation cycles, the overall film conductivity changed little if any during mechanical deformation.

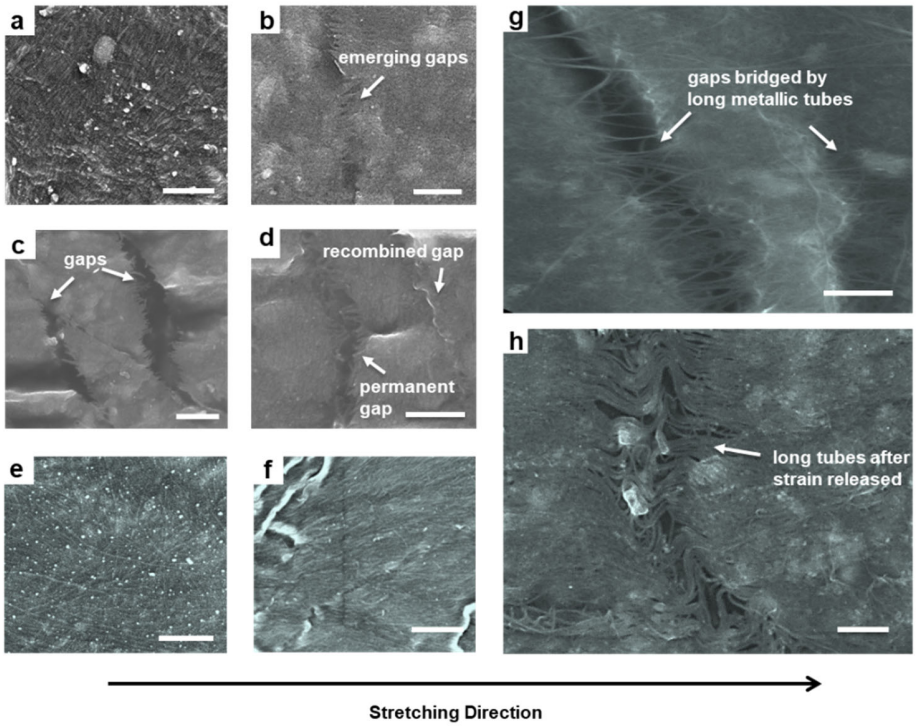

Figure 4-6. Surface morphology evolution of STCFs made from short m-DWCNTs (a,b,c,d) and μm long m-DWCNTs (e,f,g,h) under different tensile strain, including a, e) 0% tensile strain, b, f) 50% tensile strain, c, g) 100% tensile strain, and d, h) back to 0% tensile strain.

Long m-DWCNT STCFs, with their extremely stable conductivities over high tensile strain, should be ideal candidates for wearable electronic applications where stable conductivity is required in diverse configurations and at different strains. As proof of principle, a long m-DWCNT STCF featuring 85% transmittance was mounted to the joint of an index finger to mimic the motions of the human body in real life and connected to a light emitting diode (LED) as a real-time indicator of local film conductivity change (Figure 4-7a). Constant 3V was applied. Relative changes in conductivity were recorded with multiple cycles of bending/relaxing of the index finger. Figure 4-7b shows the relative resistance profile of the long m-DWCNT and short m-DWCNT STCFs. The long m-DWCNT STCFs did not show any notable changes in conductivity when the joint was bent, which is consistent with the same brightness of the connected LED light and constant measured current (from 0.0751 mA to 0.0745 mA) regardless of the position of the finger (Figure 4-7c,e). However, for short m-DWCNT STCFs, when the joint was bent, the overall resistance increased by ~40 times and the measure current dropped from 0.0229 mA to 0.584 μA. The connected LED readily responded to this local conductivity change by displaying a weak light when the finger was straight, which was totally extinguished when the finger was bent (Figure 4-7d,f). While the dramatic conductivity differences are not preferable

in flexible conductors, we note the short m-DWCNT STCFs may find application in motion sensors[110] due to their high sensitivity in response to small shape changes.

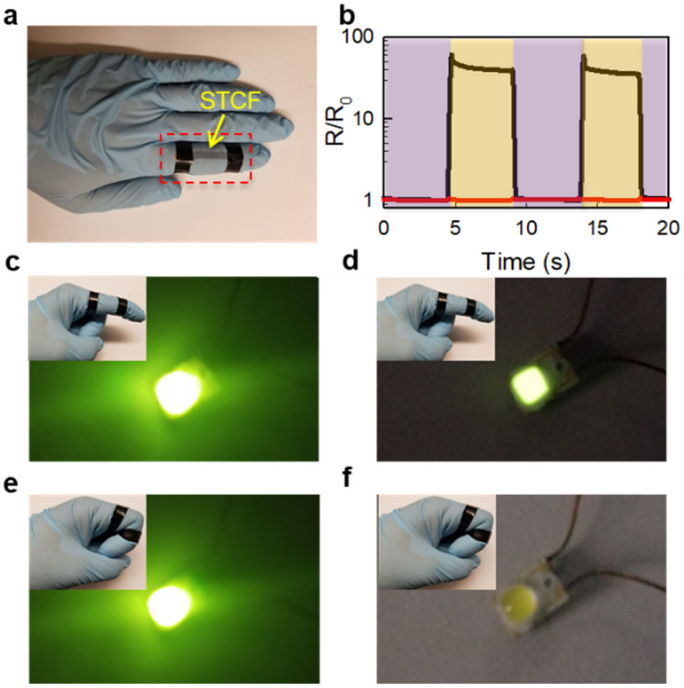

Figure 4-7. (a) A photograph of an STCF mounted on the joint of an index finger functioning as a wearable device. (b) Conductivity change of the mounted STCF when the index finger is straightened (purple area) or bent (orange area). Red and black lines are conductivity responses of long m-DWCNT and short m-DWCNT STCFs, respectively. Brightness changes from an LED attached to c, e) long m-DWCNT and d, f) short m-DWCNT STCFs during c, d) straightening and e, f) bending of the index finger.

4.4. Conclusions

We have successfully fabricated STCFs with extraordinarily high and stable conductivity over repeated tensile strain cycles by incorporating long metallic DWCNTs into PDMS. The long nanotubes were obtained by dispersing the materials in water at full-length followed by purification based on their electronic types. The resulting STCFs exhibited a high electrical conductivity of 1809 S/cm at 85% transmittance, which increased to 3316 S/cm at 100% tensile strain, and featured only a 4% decay after 1000 such stretch-release cycles. SEM images reveal that long tubes bridge gaps formed in the thin films during stretching, thus preserving the overall conductivity of the device. On the other hand, short nanotubes showed significantly larger ON/OFF ratios, making them a better candidate as strain sensors. Our results demonstrate how the length of carbon nanotubes can significantly affect their collective electrical properties, allowing transparent conductors to be fabricated from the same CNT materials and tailored for different applications in wearable electronics and human-machine interactive devices.

5. Long-SWCNT-Networks as Mechanical Reinforcement for Graphene

This chapter is adapted from a submitted manuscript

Wang, P.; Li, Y.; Wang, L.; Kłos, J.; Peng, Z.; Kim, N.; Bluhm, H.; Gaskell, K.; Liu, P.; Lee, S. B.; Eichhorn, B. W.; and Wang, Y.

P.W. and L.Y. contributed equally to this work. Y.W., B.W.E., and P.W. conceived and designed the experiments. P.W., L.Y. L.W. and K.G. performed the experiments. N.K. fabricated the AAO membranes. J.K. performed MD calculations. Z.P. performed the TEM characterizations. Y.W., B.W.E., P.W., and L.Y. wrote the manuscript with inputs from all authors.

This work is partially supported by Nanostructures for Electrical Energy Storage (NEES), an Energy Frontier Research Center funded by the U.S. Department of Energy, Office of Science, Office of Basic Energy Sciences under Award Number DESC0001160. AFM measurements were performed on a shared system supported by the NSF MRI program (CHE1626288). Part of this research project was conducted using computational resources provided by XSEDE.org through grant No. CHE-130120 to J.K. and by the Maryland Advanced Research Computing Center (MARCC) to Y.W. P.W. gratefully acknowledges the Millard and Lee Alexander Fellowship from the University of Maryland.

5.1. Introduction

In addition to the outstanding optical, electrical and electromechanical properties, long nanotubes also show excellent mechanical properties. In this section, I will describe how SWCNTs can be used to enhance the mechanical strength of the graphene materials.

The electrical double layer (EDL) is spontaneously formed at the solid-liquid interface between a charged electrode surface and an electrolyte.[111-113] The theory of EDL in conventional diluted electrolyte solution, such as inorganic ionic salts in water, was first conceptualized by Helmholtz in 1879[114] and later expanded into the Guoy-Chapman-Stern model.[115-117] Briefly, the ions form a compact layer (*i.e.*, the Stern layer) and a diffusive layer of the opposite charges (*i.e.*, the diffuse layer) at the

electrode-electrolyte interface. Ionic liquids, in contrast, are an electrolyte family that find broad applications in electrochemistry[118, 119] but behave differently from conventional electrolyte solutions.[111] Unlike a dilute aqueous electrolyte solution where the cations and anions are far apart and may be considered noninteractive at the dilute limit,[111, 120] ionic liquids are composed of cation-anion pairs that are densely packed due to strong Coulombic interactions.[113] Because of this feature, it is unknown whether the EDL for ionic liquids is correctly described by the Guoy-Chapman-Stern model. Indeed, Landau-Ginzburg-type continuum theory[121] and mean-field theory[122] suggest layer-by-layer arrangements of ions in the EDL of ionic liquids. These theories have been supported by molecular dynamics (MD) simulations[122], electrochemical impedance spectroscopy (EIS) studies,[123] and atomic force measurements[124] However, these experiments are largely macroscopic (*i.e.*, EDL capacitance measured by EIS). It remains challenging to experimentally profile the ion distribution of the EDL at the molecular level.

X-ray photoelectron spectroscopy (XPS) is an elemental analysis technique that can be used to quantitatively study atom/ion concentrations, chemical composition, and bonding conditions of various materials by exciting the sample with X-rays and measuring the kinetic energy of the emitted photoelectrons.[125] Since the inelastic mean free path (λ_{IMFP}) of the emitted photoelectrons is very short, XPS provides surface-sensitive detection, with a penetration depth typically ranging from a few to tens of nanometers.[125] As a result, XPS should be well-suited for elucidating the EDL structures, whose thickness falls into the same scale (for aqueous solution, typically < 30 nm, with the Stern layer being < 5 nm; for ionic liquid, ~5 nm),[111, 113] allowing the

observation of different ionic species and providing a better understanding of the EDL structure at the molecular level.

In principle, there are two ways to use XPS to investigate the EDL: either applying the X-rays and collecting the resulting signal from the electrolyte (liquid) side of the device (Figure 5-1a), or doing the same except from the electrode (solid) side (Figure 5-1b). With the former experimental configuration,[126, 127] the emitted photoelectrons must penetrate through the bulk electrolyte solution to reach the detector, and as a result, a significant amount of the signal with valuable information about the "buried" EDL structure is lost (Figure 5-1a). Sophisticated experimental set-ups and ultrabright light sources are needed to mitigate the severe inelastic scattering of emitted photoelectrons in bulk electrolytes, and therefore only a limited number of successful cases have been demonstrated (e.g., the "dip-and-pull" method involving a synchrotron light source.[126, 127]

Alternatively, the emergence of two-dimensional (2D) conductive materials, such as graphene,[128, 129] has made the latter (solid-side) experimental configuration possible (Figure 5-1b,c). Photoelectrons emitted from the EDL can easily penetrate a graphene sheet without much inelastic scattering due to its ultrathin thickness and the low-atomic-number of carbon atoms. Towards this end, photoelectron spectroscopic studies on aqueous electrolyte[130-132] and solid nanoparticles[132-134] capped by graphene or graphene oxide layers[135, 136] have been conducted and provided deeper understanding of fundamental electrochemical oxidation/reduction processes. However, up to now, no *operando* experiments have been conducted to decipher the molecular structures of the EDL formed by ionic liquids at the solid/liquid interface, presumably because the

high viscosity of the ionic liquids make it difficult for a bare graphene membrane to hold the liquid without leaking.

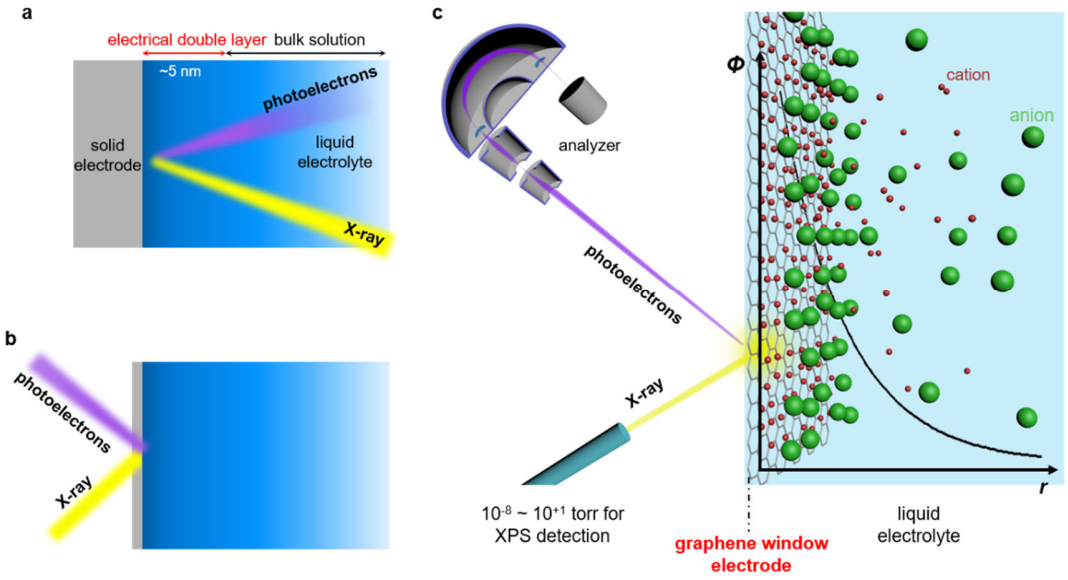

Figure 5-1. Schematics of *operando* XPS observation of the EDL at the solid-liquid interface. a-b) Two ways of detecting the solid-liquid interface: from the (a) liquid and (b) solid sides of the electrode. The dimmer purple color of the photoelectron beam in Figure a indicates the decaying of the photoelectron flux travelling through the bulk liquid. c) Schematic illustration of *operando* XPS visualization of the EDL behind an atomically-thin G+T window (SWCNTs are not shown for picture clarity). We apply a negative voltage to the graphene to produce an EDL in the electrolyte contained behind the electrode.

In this work, we developed a hybrid graphene/carbon nanotube (G+T) transparent working electrode that enables us to measure the EDL configuration formed on the solid-liquid interface (Figure 5-1c). In our design, an ionic liquid electrolyte (1-

butyl-1-methylpyrrolidinium bis[(trifluoromethane)sulfonyl] imide [$Bpy_{1,4}$][TFSI] containing 1 M of lithium TFSI) is sandwiched between a counter electrode and the electrically biased G+T working electrode, which also serves as a "watching window" that allow us to directly "observe" the EDL formed behind it responding to the applied voltage. Our G+T hybrid membrane features multiple advantages: (1) the mechanical strength of the hybrid film is reinforced by long, single-walled carbon nanotubes (SWCNTs) with little sacrifice of the photoelectron transparency; (2) the hybrid membrane is electrochemically stable due to the inertness of both the graphene and SWCNTs; (3) the superior electrical conductivity makes the G+T membrane an excellent working electrode; (4) the hybrid film can easily cover a large area (cm^2), well accommodating the analysis spot size of XPS (for high sensitivity XPS on lab-based instruments, the spot sizes are generally ~1 millimeter in diameter or greater) and allowing for more photoelectron signal detection and therefore higher sensitivity; (5) no assistive polymers are needed during the membrane transfer process, ensuring a clean membrane and therefore preventing contamination signals in subsequent XPS measurements. Due to these advantages, our integrated liquid cell featuring the G+T hybrid membrane as a transparent working electrode enables the sensitive detection of elements with small photoionization cross-sections, such as nitrogen and sulfur. With this liquid cell device, we quantitatively monitored the concentration distribution profile of cations and anions in the resulting EDL and successfully observed the "charge flipping" phenomenon when the G+T working electrode was biased with the reverse electrical potential.

5.2. Experimental Section

5.2.1. Graphene Growthy by the Chemical Vapor Deposition

The graphene films were grown on 2 cm ×2 cm, 25 μm thick Cu foils (Alfa Aesar) following the literature description.[137] Briefly, the Cu foil was placed in a fused silica tube in a chemical vapor deposition (CVD) furnace. After the evacuation of the system, H_2 (g) at a 15 sccm flow rate was introduced and the system base pressure was maintained at 40 mTorr. The furnace was then heated up to 1030 °C and annealed for 60 min. CH_4 (g) at 10 sccm flow rate was then introduced, and the pressure in the chamber was tuned to 500 mTorr. The growth process lasted for 30 min. After the graphene growth, the furnace was cooled down to room temperature at a cooling rate of 80 °C/min.

5.2.2. Fabrication of G+T Hybrid Film

Highly crystalline SWCNTs (EC1.5, Meijo Nano Carbon Co., Ltd.) were dissolved in chlorosulfonic acid (Sigma Aldrich) at ~0.4 mg/mL by mechanical stirring with a magnetic stir bar for 3 days. ~50 μL of the SWCNT-acid solution was spin coated on top of the graphene-on-Cu foil at 3500 rpm for 2 min, followed by the addition of ~200 μL of nanopure water (Barnstead Nanopure water purification system, Thermo Scientific) to remove any remaining acid. (*Safety Note: protective lab apparel, including a lab coat, goggles, facial mask, and acid resistive gloves are necessary for handling the chlorosulfonic acid.*) The sample was then placed on a hot plate at 120 °C for 2 min. Since the graphene was grown on both sides of the Cu foil, to facilitate the etching process, we etched the graphene on the side without the spin-coated carbon nanotubes using a UV/Ozone ProCleaner TM (Bioforce Nanosciences) for 20 min. The Cu foil was then wet etched in 0.1 M $(NH_4)_2S_2O_8$ (Sigma Aldrich) aqueous solution

overnight, after which a free-standing G+T hybrid film could be found floating on the surface of the etching solution. The etching solution was then gradually exchanged into isopropanol to decrease the surface tension (surface tension of water: ~73 mN/m; isopropanol: ~23 mN/m) of the solvent prior to transferring the G+T to the substrate.[138] Si_3N_4 perforated substrates were purchased from Aquamarijn Company, Netherlands.

5.2.3. Film Intactness Analysis

We characterized the film intactness based on the SEM images of the suspended membranes using ImageJ software. The broken holes can be discriminated from the intact membrane due to the different color contrast. The area of the intact parts and broken holes can be automatically calculated by the software. We note here that the intactness is defined as the ratio of the intact area to the total area of all suspended area, i.e., intactness = (1- area of the broken holes / area of all circular suspended area) × 100%, as used in the literature.[139]

5.2.4. Fabrication of the AAO Film

AAO films were fabricated utilizing the two-step anodization method. 0.25 mm thick, 99.99% pure aluminum foil was purchased from Alfa Aesar. The Al foil was degreased in acetone under sonication for 5 minutes. The degreased Al foil was then placed in a solution composed of 160 mL of 70% perchloric acid and 800 mL of 200 proof ethanol at 3 °C, along with a plate of stainless steel. 15 V was applied for 5 minutes between the Al foil as the anode and the stainless-steel plate as the cathode to electropolish the Al foil. The Al foil was first anodized in 0.3 M oxalic acid at 8 °C under 40 V for 6 h. The disordered anodized layer from the first anodization was then removed by etch solution composed of 70 mL of 85% phosphoric acid, 180 mL of 10%

chromic acid, and 750 mL of water at 60 °C for 4 h. This left a pre-patterned surface on the Al foil. The second anodization was performed for 12 h. The remaining Al was removed in 1 L of saturated $CuCl_2$ with 10 mL of 37% hydrochloric acid to facilitate the removal of Al. The barrier layer of the AAO was selectively removed by placing the film in 0.1 M phosphoric acid for 40 minutes. The AAO was pore widened in 5% phosphoric acid at 38 °C for 11.5 minutes.

5.2.5. Spectroscopic and Microscopic Characterization

Raman spectra were recorded from 500 to 3000 cm^{-1} using a LabRAM ARAMIS Raman microscope (Horiba Jobin Yvon) with 633 nm excitation. The integration time was 0.8 s, taken 10 times in total. The power density of the incident laser was 1.2 $mW/\mu m^2$. UV-vis-NIR transmittance spectra were measured using a Lambda 1050 (Perkin Elmer) spectrometer with a broadband InGaAs detector and an integrating sphere (Labspere Model No. 150 mm RSA ASSY). SEM and TEM images were taken using a Hitachi SU-70 SEM and a JOEL LaB6 TEM, respectively.

5.2.6. XPS Measurement

We performed the XPS measurements on a Kratos Axis 165 X-ray spectrometer with monochromatic Al Kα beam radiation (1486.7 eV). Modifications were made to the XPS system and the sample holder for the adaption of the *oprando* electrochemical and spectroscopic measurement. The regular sample holder was cut into halves and rejointed together by a piece of insulating Macro ceramics, so that it has two electrically-conductive yet isolated parts. A copper rod, which could be moved up and down, was added to the transfer chamber to make the electrical connection to the sample transfer arm, which was left connected to one side of the sample holder after

transfer. This side acted as the ground. The other side of the sample holder was connected to the metal fork in the analysis chamber, which was connected with a potentiostat (Bio-Logic SP-200) through a BNC cable so that the potential can be applied. The pass energies used for the survey scans and high-resolution scans were 160 eV and 40 eV, respectively, and the base pressure for the measurement was below ~10^{-8} Torr. The XPS spectra was deconvoluted and fit using CacaXPS software. A Shirly background and 30% Gaussian/Lorentzian product formula (GL(30)) was used for all the peak fittings except for sp^2 C 1s signal, which was fitted instead by the asymmetric-parameters-modified Gaussian/Lorentzian product formula (A(0.35, 0.35, 35)GL(30)), in order to accommodate the asymmetric line shape of the sp^2 carbon at high binding energy.[38, 140]

5.2.7. MD simulations

We used classical molecular dynamics approach to simulate the formation of the electrical double layer in a system composed of 6900 ions (2645 [Bpy1,4][TFSI] and 805 [Li][TFSI] ion pairs). The ions were enclosed in a 10 nm ×10 nm ×20 nm 3-dimensional rectangular cuboid graphene layer box in which two 10 nm × 10 nm monolayer graphene windows separated by 20 nm serve as a positively and negatively charged electrodes. The four remaining 10 nm × 20 nm graphene walls of zero charge were used as enclosure to prevent ions to move outside the boundaries of electrodes during the simulations. All the graphene layer coordinates were kept fixed during the MD simulations. The dielectric constant was set to a value of 14.7 t corresponding to our ionic liquid. All the MD simulations were performed with the NAMD package[141] and results were analyzed and visualized using VMD 1.9.4 program.[142]

In order to perform MD simulations, we have developed necessary force field parameters for the Bpy1,4 and TFSI ionic pairs using *ab initio* geometry optimizations of these molecules and Force Field ToolKit[143] available in VMD. The partial charges from Natural Bond Order analysis of Bpy1,4 and TFSI ions were obtained from Density Functional Theory (DFT) calculations employing ωb97xd functional and 6-311G(d,p) basis set. The ab initio calculations were performed using Gaussian 09 program.[144]

The initial distribution of all ions inside the 10×10×20 nm graphene layer rectangular cuboid box has been prepared with Packmol program.[145] This initial structure was used to prepare topology and structure files for NAMD calculations. The MD simulations were performed at room temperature with the Langevine dynamics switched on. The trajectory was propagated for 6 ns with the first 25000 steps for minimization procedure. We have performed separately simulations for voltage conditions corresponding to 0, 1 and 3V potential used in experiments. The carbon atoms of the 10×10 nm graphene layer electrodes were given partial charges to correspond to these voltages and the simulations were performed with the electric field switched on corresponding to the experimental conditions. At the end of the simulations we analyzed the last 54 frames of each trajectory to obtain horizontal pair distribution functions of each kind of ion and electrode to quantify the appearance of electric double layer. The horizontal pair distribution function was taken along the z-axis spanning 20 nm length between the graphene window electrodes.

5.2.8. XPS Signal Calculation from the Molecular Dynamics Simulation Results

The XPS photoelectron signal that can travel through a solid and reach the detectors can be calculated by equation 1:

$$I = I_d \times e^{-\frac{d}{\lambda_{IMFP} \sin\theta}}$$

in which I is the detected XPS signal intensity; I_d is the XPS signal intensity generated at a depth of d in the sample; λ_{IMFP} is the inelastic mean free path of the photoelectrons in the sample; θ is the takeoff angle of the photoelectrons relative to the sample surface, which is set as 90°.

Also, since I_d is linearly related to the local concentration (C_d) of the species:

$$I_d = \mathrm{A}C_d$$

we can derive

$$I_1 = I_d \times e^{-\frac{d}{\lambda_i}} = AC_d \times e^{-\frac{d}{\lambda_i}}$$

in which I_1 is the signal intensity before travelling through the graphene layer and λ_i is the inelastic mean free path in the ionic liquid media. For N 1s photoelectrons with kinetic energy of ~1050 eV (beam energy for monochromatic Al anode: 1486.6 eV; binding energy for N1s: ~400 eV), λ_i in ionic liquid media is estimated to be ~2.5 nm based on NIST Standard Reference Database 71. As a result, the final signal intensity I that can penetrate through the G+T layer is

$$I = I_1 \times e^{-\frac{d_g}{\lambda_g}} = (AC_d \times e^{-\frac{d}{\lambda_i}}) \times e^{-\frac{d_g}{\lambda_g}}$$

Where d_g and λ_g are the thickness of the graphene layer and the inelastic mean free path, respectively.

Therefore, the theoretical N^+/N^- ratios can be calculated as

$$\frac{I_{N^+}}{I_{N^-}} = \frac{\sum_0^d \left(AC_{d(N^+)} \times e^{-\frac{d}{\lambda_i}} \right) \times e^{-\frac{d_g}{\lambda_g}}}{\sum_0^d \left(AC_{d(N^-)} \times e^{-\frac{d}{\lambda_i}} \right) \times e^{-\frac{d_g}{\lambda_g}}} = \frac{\sum_0^d (AC_{d(N^+)} \times e^{-\frac{d}{\lambda_i}})}{\sum_0^d (AC_{d(N^-)} \times e^{-\frac{d}{\lambda_i}})}$$

5.3. Results and Discussion

5.3.1. Long SWCNTs Supported Graphene Hybrid Membrane (G+T) as the Ultrathin, Transparent and Mechanical Strong Electrochemical Electrode

We fabricated the G+T hybrid membrane by spin coating a thin layer of SWCNTs on the surface of a graphene. To guarantee enough mechanical support for the graphene layer without building up the film thickness, a uniform SWCNT network mainly comprised of long SWCNTs[25, 146] is favorable. Furthermore, the solvent dissolving SWCNTs should wet the graphene surface, which is hydrophobic, so that the SWCNTs can be homogenously distributed on the graphene surface by spin coating. Towards this end, we chose chlorosulfonic acid to disperse the SWCNTs because it is a true solvent that can nondestructively dissolve SWCNTs through protonation as well as wet the graphitic surface.[147-149] The SWCNT-chlorosulfonic acid solution was then spin coated onto a few-layered (2-3 layers) piece of graphene that was grown on a copper foil by chemical vapor deposition[137] (Figure 5-2a). The resulting graphene plus nanotubes (G+T) hybrid window is mechanically robust, as clearly evidenced by the large and uniform free-standing membrane floating on water after the copper substrate is etched away (Figure 5-2b). In contrast, the graphene without SWCNTs cracks into small pieces due to the strong surface tension of water (Figure 5-3). Transmission

electron microscopy (TEM) imaging (Figure 5-2c) of the G+T membrane clearly demonstrates that the SWCNTs are uniformly distributed across the graphene surface, which may act as rebar-like supporting structures. Due to the strengthening effect of the SWCNT network, the G+T membrane can be easily fabricated into centimeter-sized pieces (Figure 5-2b, 5-3). The electron diffraction also indicates its high crystallinity, which is consistent with the resonant Raman spectroscopy measurement, which shows no obvious D peak (~1350 cm^{-1}) (Figure 5-4). Compared to graphene without the SWCNT supports, the G+T membrane also features ~4-fold improvement in electrical conductivity, a cleaner surface from the transfer, and only ~3% sacrifice in the optical transmittance (Figure 5-5 – 5-7). We also determined the thickness of the hybrid film was 1–1.5 nm based on the ~92% film transmittance (Figure 5-7).[150, 151]

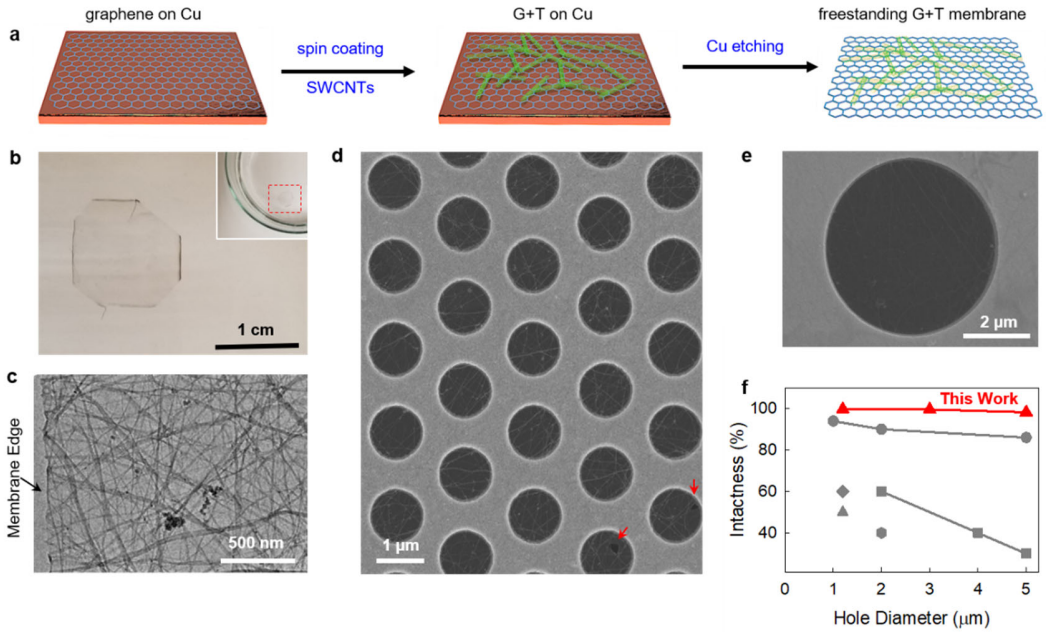

Figure 5-2: Schematics of *operando* XPS that directly measures the EDL at the solid-liquid interface. a-b) Two ways of detecting the solid-liquid interface: from the (a) liquid and (b) solid sides of the electrode. The dimmer purple color of the photoelectron

beam in Figure a indicates the decay of the photoelectron flux travelling through the bulk liquid. c) Schematic illustration of *operando* XPS visualization of the EDL behind an atomically-thin G+T window (SWCNTs are not shown for image clarity). We apply a negative voltage to the graphene to produce an EDL behind the XPS-transparent electrode.

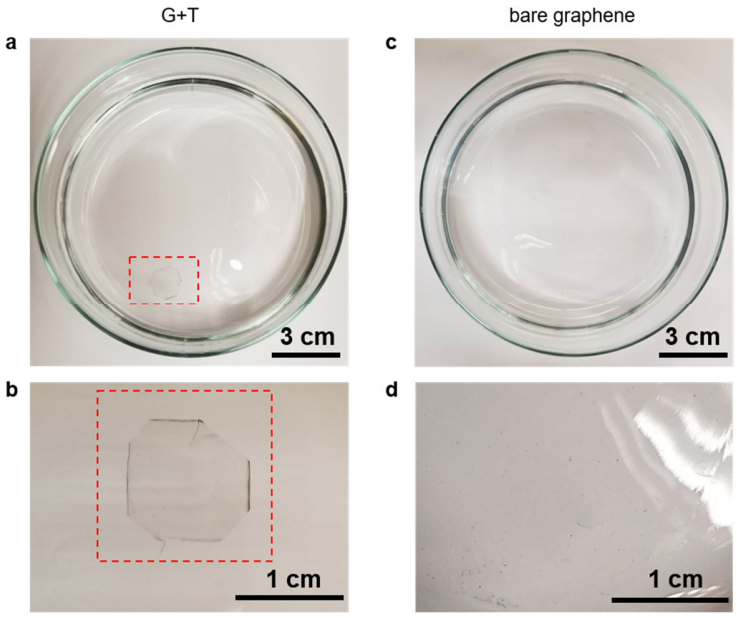

Figure 5-3. a, b) Optical photos showing a centimeter-sized G+T hybrid film floating on water without breaking. c, d) Bare graphene without the support from SWCNTs cracks into small pieces that can hardly be seen due to the surface tension of water.

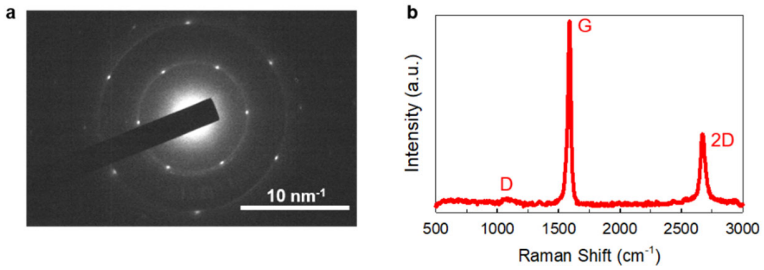

Figure 5-4. a) The selected area electron diffraction pattern and b) non-detectable D peak in the resonance Raman scattering spectrum demonstrate the crystallinity of the G+T hybrid film.

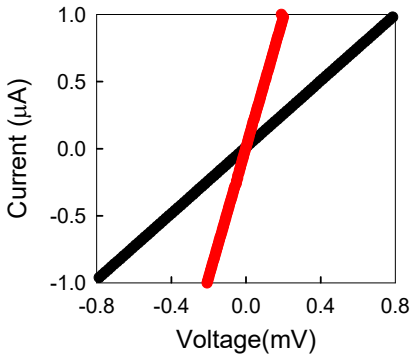

Figure 5-5. Voltage-current (IV) curves show the G+T hybrid film (red) features ~4-times improvement in conductivity compared to a bare graphene film without SWCNTs (black).

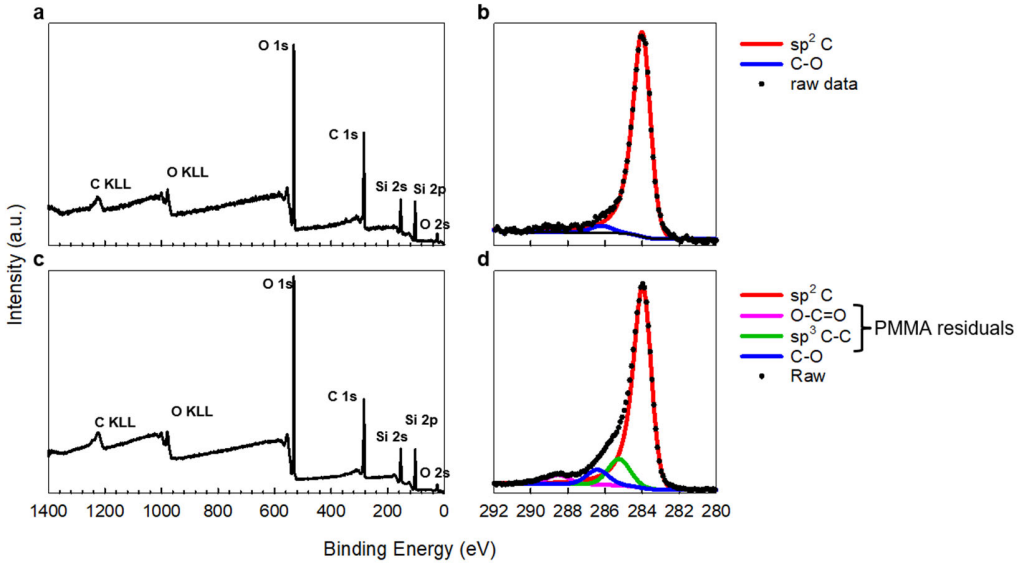

Figure 5-6. Surface comparison between the (a, b) G+T hybrid film and (c,d) a graphene film transferred by the PMMA method.[152] Both films were transferred onto a Si/SiO_2 substrate for XPS tests. The G+T film shows no detectable contamination signals, as evidenced by the lack of C 1s signal from sp^3 C-C bonds and O-C=O bonds that are present in the PMMA-transferred graphene control sample.

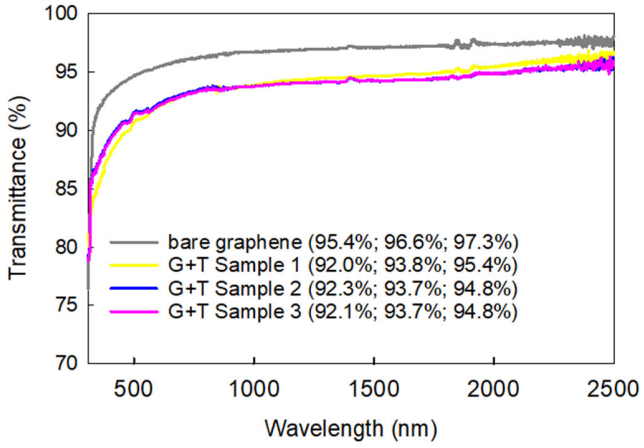

Figure 5-7. Transmittance comparison between the G+T film and bare graphene. The hybrid film shows outstanding optical transmittance in the wavelength range of 300–2500 nm. Three replicate samples of the G+T film are shown to demonstrate the reproducibility of the material synthesis. Figures in the parentheses from left to right indicate the transmissive values at the wavelengths of 600 nm, 1000 nm, and 2000 nm, respectively, for each sample.

Apart from the large size, mechanical robustness, high electrical conductivity, clean surface, and ultrathin thickness, the G+T hybrid membrane must also be pinhole free if it is to contain a liquid electrolyte. In order to statistically evaluate the intactness of the film, we transferred the G+T membrane onto a perforated Si_3N_4 microsieve membrane with different holes sizes and then used high-resolution scanning electron microscopy (SEM) to examine the quality of the suspended film. Figure 5-2d displays a typical SEM image of the suspended G+T film on the Si3N4 membrane with circular hole-diameters of 1.2 μm. Higher magnification demonstrates the high quality of the suspended graphene film on a 5 μm circular hole supported by long SWCNTs with no observable pinholes (Figure 5-2e). We further analyzed the intactness of the film by examining a suspend area over 10,000 μm^2 across hole sizes of 5 μm, 3 μm, and 1.2 μm, respectively, finding that the G+T membrane achieved intactness rates of 98.2%, 99.6%, and 99.7%, respectively (Figure 5-8). We note that the intactness of our hybrid membrane is among the best of suspended graphene on perforated substrates reported in the literature (Figure 5-2f).[152, 153]

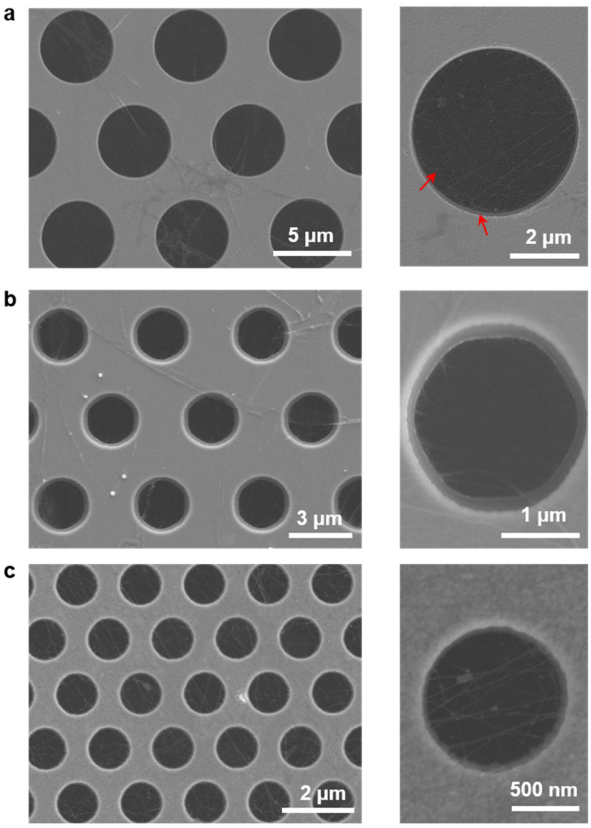

Figure 5-8. Typical SEM images of the suspended G+T hybrid membrane on a perforated Si_3N_4 substrate featuring (a) 5 µm, (b) 3 µm, and (c) 1.2 µm holes. The magnified SEM image clearly shows the SWCNTs serving as supports for the graphene membrane. Red arrows indicate the long SWCNTs as the supporting structures.

5.3.2. G+T Hybrid Film Enabled *oprando* XPS Observation of Electrical Double Layer Formation at the Solid-Liquid Interface

We then assembled a liquid cell by transferring the G+T hybrid membrane (as the transparent working electrode) onto a piece of insulating anodic aluminum oxide (AAO) film to produce a parallel electric capacitor (Figure 5-9a). Figure 5-10 shows the SEM image of the surface morphology of the liquid cell after infusing the AAO with the ionic liquid. Compared with the filled pores, the cracked film/empty pores/membrane pinholes (red arrow in Figure 5-10) appear darker under SEM, and correspondingly, the energy dispersive X-ray spectroscopy (EDS) shows significantly lower C and F signal at the darker pores (Figure 5-11). These results confirm that after the infusion of ionic liquid, the AAO pores are filled and the G+T membrane remains mostly intact. We then measured the signal attenuation by comparing the XPS signal from the pure ionic liquid and that from the ionic liquid beneath the G+T film (Figure 5-9b). Although we observed a significant increase of the C 1s signal in the presence of the G+T film, photoelectrons generated from the film-capped ionic liquid was clearly resolved (see F 1s, N 1s, and S 2s in Fig. 5-9b). We can deconvolute and unambiguously assign the C 1s scans to different carbon species from the ionic liquid (Figure 5-9c,d).

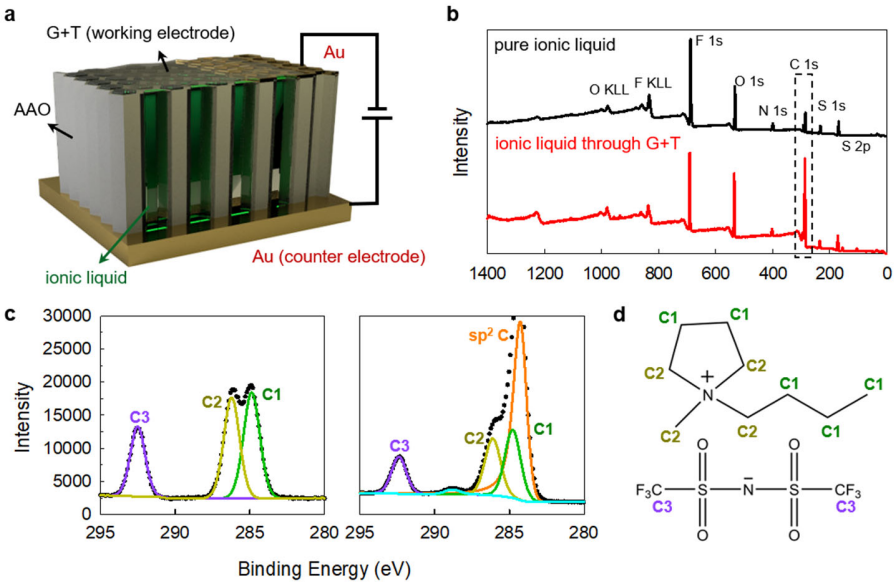

Figure 5-9. Characterization of the G+T liquid cell without applied bias. a) Schematic illustration of the liquid cell featuring the G+T window. b) XPS survey scan of the pure ionic liquid (black line) and ionic liquid through the G+T window (red line). c) Deconvoluted peaks from the C 1s XPS signal of the pure ionic liquid (left) and ionic liquid through the G+T window (right). d) Molecular structure of the ionic liquid (N-methyl-N-butylpyrrolidinium bis(trifluoromethylsulfonyl)imide) used in this paper.

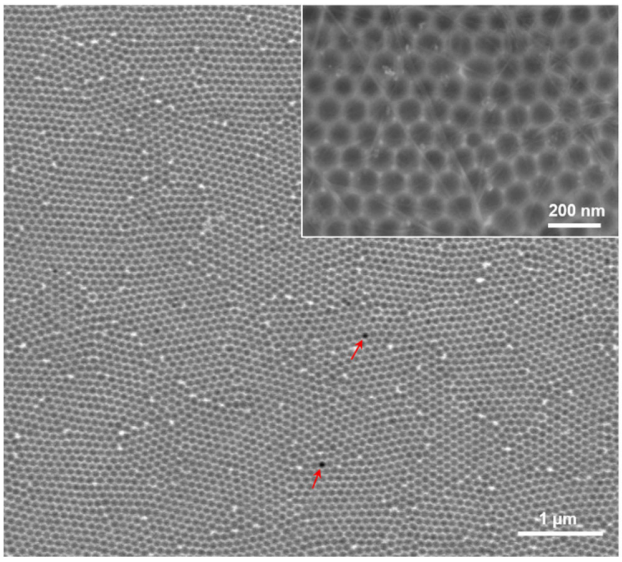

Figure 5-10. Typical SEM image of the suspended G+T hybrid membrane on an AAO film. The AAO is filled with ionic liquid. Red arrows indicate the pinholes in the G+T membrane. Top right: Zoomed in image of the G+T on AAO.

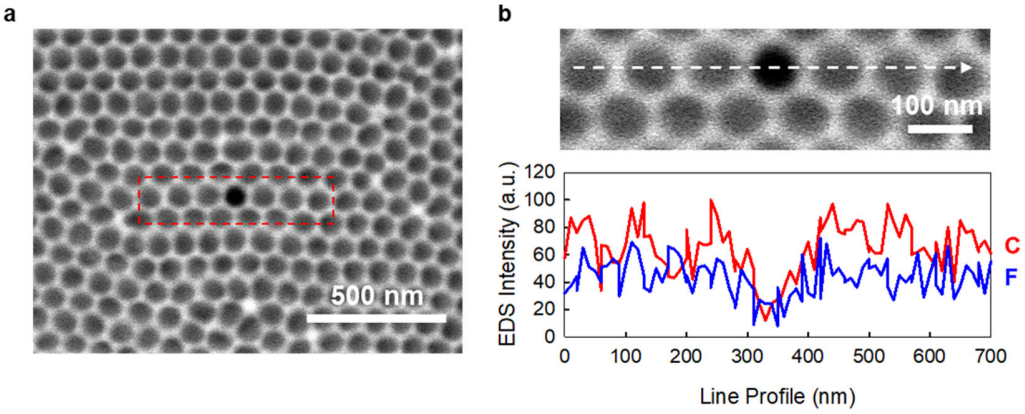

Figure 5-11. EDS analysis shows that the color contrast in the SEM image is due to a pinhole in the G+T membrane. a) An SEM image of the suspended G+T hybrid membrane on the AAO membrane. b) The darker component of the film shows significantly less C and F signal, indicating the breakage of the G+T membrane.

Having observed clean XPS signal though the G+T window, we further show it is possible to directly capture the EDL formation under applied potentials and *in operando* monitored the XPS signal changes from different elements. Cyclic voltammetry (CV) reveals a double layer capacitive behavior of the liquid cell, as shown by the near rectangular-shape of the CV curve (Figure 5-12a). We then applied chronoamperometry to the G+T membrane to charge/discharge the liquid cell and *operando* measure the XPS signal. The XPS results were acquired when the equilibrium state of the EDL charging/discharging was reached, as evidenced by a negligible constant residue current of close to zero (Figure 5-12b). We determined the local electrical potentials of the G+T membrane by measuring the photoelectron spectral shifts relative to the peak position at 0 V, which originate from the changes of the Fermi level of the elements.[154] Figure 5-13a shows the N 1s signal at different local electrical potentials of the G+T membrane. The signal can be deconvoluted into two distinct peaks, which can be attributed to the Bpy1,4 cations (higher binding energy, N^+ 1s, red) and the TFSI anions (lower binding energy, N^- 1s, blue) of the ionic liquid, respectively. Since the escape depth of the emitted photoelectrons is only a few nanometers, as we varied the local potential, changes in the peak areas of the N^+ 1s and N^- 1s signals reflect the ion population changes adjacent to the G+T. The intensity of N^+ 1s signal increases at more negative voltages, indicating that Bpy1,4 cations preferentially accumulate beneath the G+T membrane. Switching to a positive voltage range, we observed an increase of the N^- 1s signal as a result of more accumulated TFSI anions.

We further plotted the ratio of the integrated area for N^+/N^- as a function of the local potential in Figure 5-13b to better illustrate the change of the cation/anion concentrations. Specifically, the N^+/N^- ratio changed from ~0.55 at -2.5 V to ~1.10 at +2.2 V. Figure 5-13c shows the reversible, switching behavior of the N^+/N^- ratio, unambiguously demonstrating the dynamic spectral changes that originate from the charging-discharging capacitive behavior of the EDL formed at the electrode/electrolyte interface. We also note that, although more cracks can be observed on the G+T membrane after the electrochemistry and XPS test, the intactness is still more than 90% (Figure 5-14), demonstrating the superior robustness of the membrane

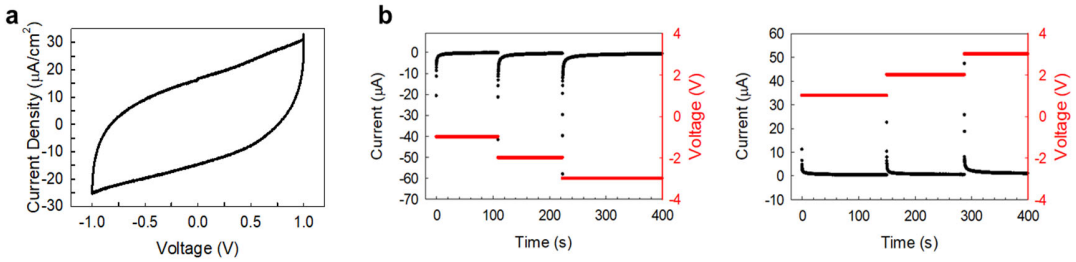

Figure 5-12. (a) A CV curve of the liquid cell. The scan rate was 50 mV/s. (b) The chronoamperometry curves of the liquid cell *operando* measured in the XPS chamber. As the applied voltage changes (red), the liquid cell shows ideal current responses (black; instant current increase and then exponentially decaying to zero). The XPS spectra were measured at the steady-state-current condition when the current drops to zero.

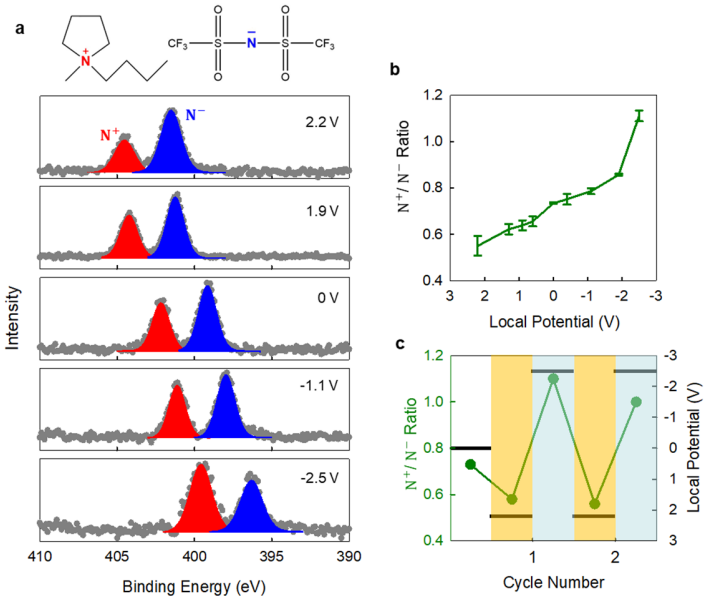

Figure 5-13. *Operando* XPS monitoring of EDL formation with different biases applied to the G+T window. a) N 1s XPS spectra at different biases applied to the G+T window. The spectra can be deconvoluted into two peaks attributed to N^+ (red) and N^- (blue). b) N^+/N^- signal ratio change *vs.* the local potential on the G+T membrane. c) The reversible switching behavior of the N^+/N^- ratio (red line), which was switched at the local potentials indicated by the black lines.

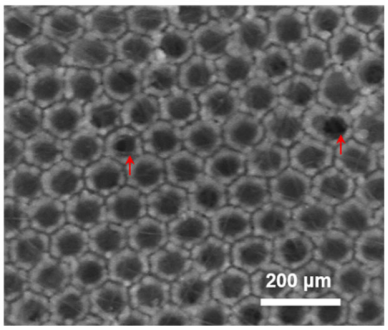

Figure 5-14. SEM images of the liquid cell after the electrochemistry in the XPS chamber. The intactness of the G+T hybrid film is still higher than ~90.0% after electrochemical testing.

To provide further insight into the EDL formation on the G+T hybrid film, we used molecular dynamic (MD) simulations to model the EDL structures and calculate the theoretical N^+/N^- ratio changes at different local potentials. We confined 2645 [Bpy1,4][TFSI] and 805 [Li][TFSI] ion pairs between two 10×10 nm parallel monolayered graphene layers separated by a distance of 20 nm as the working and counter electrodes (Figure 5-15), which were kept mechanically rigid during MD simulations. Constant voltages were then applied to the two electrodes corresponding to experimental conditions, and the dielectric constant is adjusted to that of the studied ionic liquid. Figure 5-15a,b presents the snapshots of the MD trajectory for the EDL structure at the equilibrium state for -3 V and +3 V after the total energy was converged at 298 K after 6 ns time propagation of the MD trajectory. The accumulation of Bpy1,4 cations and TFSI anions was observed at the negative and positive electrodes, respectively. Moreover, we observed multilayered structures extending for more than ~20 Å from the graphene electrodes, which agrees with the previous theoretical simulations[122] and experimental results.[155] Figure 5-15c,d plot the horizontal ion density distribution profiles of the Bpy1,4 cations, TFSI anions and Li cations as a function of their position relative to the graphene electrode surface at +3 V and -3 V respectively. Based on the MD simulations results, we calculated the theoretical change in the XPS N^+/N^- ratio with respect to different voltages and compared these findings

with our experimental data (Figure 5-15e). We found out experimental data are highly consistent with the theoretical modeling results.

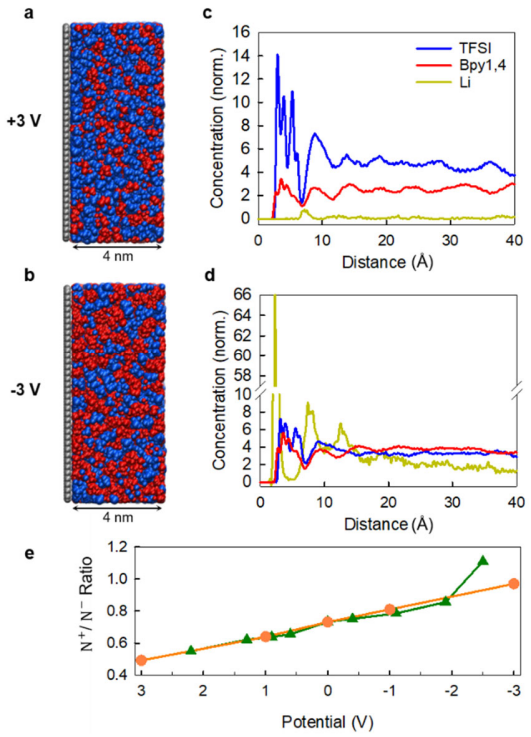

Figure 5-15. Correlation of the molecular modeling with the experimental results. a,b) Cross-sectional configuration snap-shots of the distribution of the ionic liquid molecules adjacent to the (a) +3 V charged and (b) -3 V charged graphene surfaces (Bpy cation (red); TFSI anion (blue)). Li cations are not shown for clarity. c,d) Ionic liquid concentration profile as a function of distance relative to the biased electrode surfaces (c: +3 V; d: -3 V; Bpy cations: red lines; TFSI anions: blue lines; Li cations: yellow lines). e) Comparison of the N^+/N^- signal ratio change *vs.* the local potential from MD modeling (orange) and the experimental data (green).

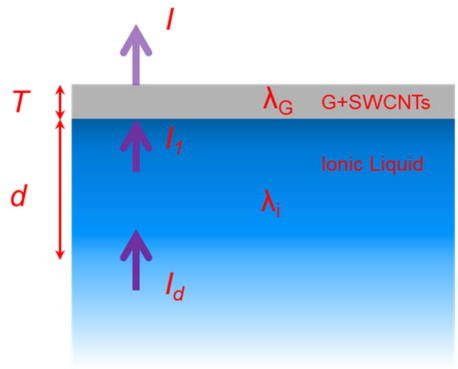

Figure 5-16. Schematic of the liquid cell model for XPS signal calculation.

5.4. Conclusions

In conclusion, we have successfully observed the formation and dynamic change of the EDL structure using *operando* XPS and a robust G+T membrane as the transparent working electrode in a liquid cell containing ionic liquid as electrolyte. Due to the mechanical support provided by the long SWCNT network, the G+T membrane can be made centimeter-sized while also being ultrathin and providing outstanding photoelectron transmittance. With this setup, we can obtain high resolution XPS spectra of the resulting EDL structure when an electrical field is applied, even from elements that feature a small photoionization cross-section, such as nitrogen. Cation and anion concentration changes calculated from their peak areas at different local potentials were correlated and found to be consistent with MD modeling. The experimental configuration introduced here opens up opportunities for exploration of chemical and physical phenomena at solid-liquid interfaces and may spur future development in material synthesis, catalysis, and energy storage research.

6. S2E Ramifications: Large Scale Synthesis of Organic Color Center-Tailored SWCNTs.

This chapter is adapted from a published manuscript.[156]

Luo, H.; Wang, P.; Wu, X.; Qu, H.; Ren, X.; Wang, Y. *ACS Nano*, **2019**, 12, 7, 8417

H.L. and P.W. contributed equally to this work. Y.W. and P.W. conceived and designed the experiments. H.L. and P.W. performed the experiments. X.W and H.Q. performed the photoluminescence microscopy characterization. Y.W., H.L., and P.W. wrote the manuscript with inputs from all authors.

This work is partially supported by NSF (Grant No. PHY1839165). H.L. gratefully acknowledges the support provided by the China Scholarships Council (CSC No. 201708320366) during his visit to the University of Maryland. P.W. gratefully acknowledges the Millard and Lee Alexander Fellowship from the University of Maryland. AFM measurements were performed using a shared system supported by the NSF MRI program (CHE1626288).

6.1. Introduction

Organic color center (OCC), which are sp^3 quantum defects intentionally implanted into the sp^2 carbon nanotube lattice,[157-161] are being intensively investigated because of their molecularly tunable defect PL in shortwave infrared (IR).[162, 163] The implanted sp3 defects create local potential wells in the semiconducting SWCNT host, allowing mobile excitons to be harvested at the trapping defect and converted into infrared PL with high efficiency and single-photon purity.[163, 164] These exciting properties have motivated the exploration and demonstration of room temperature quantum light emitters,[163] NIR-II bioimaging contrast agents,[22] and *oprando* biological pH sensors.[165] However, the synthesis of OCC-SWCNTs is currently limited at μg/mL scale, which prevents the exploration of many potential applications that require larger quantities of materials. For example, in the case of bioimaging applications, the *in vivo* administration to small animals (*e.g.,* mice and rats) typically require SWCNT

concentrations ranging from ~0.1 to 10 mg kg^{-1},[166, 167] corresponding to at least milligrams for administration to an adult human. Furthermore, large-scale synthesis is also required to reduce processing costs and minimize batch-to-batch variation.

The synthesis of OCC-SWCNTs generally involves implanting sp^3 defects onto semiconducting SWCNT surfaces through the formation of C-C covalent bonds. A scalable synthetic route to produce this promising material should thus meet three prerequisites: (1) the ability to process a large amount of SWCNTs as the reactant material; (2) a facile chemistry to create C-C bonds; and (3) a solvent to individually disperse SWCNTs at high concentrations so that the nanotube surfaces are accessible for the OCC-implanting chemistry. The mass production of SWCNTs has been commercially achieved (e.g., up to 10 tons per year scale at OCSiAl), which provides a sufficient source of raw SWCNTs. However, as-synthesized SWCNTs are bundled due to strong van der Waals attractions, making the nanotube surface largely inaccessible to reactant molecules. As a result, individualizing SWCNTs are necessary to increase the efficiency of OCC-implanting chemistry.

Toward this end, previous methods of synthesizing OCC-SWCNTs have involved stabilizing individual SWCNTs by surfactants in aqueous solution as the first step. However, even with the aid of surfactants, the concentration of SWCNTs dissolved in water is still very low.[34, 168] Moreover, using surfactants to stabilize individual SWCNTs incurs a serious trade-off: strong surfactants, such as DOC, effectively stabilize by homogenously and tightly encapsulating the nanotubes, which in turn, make the nanotube surface less accessible for subsequent reactions.[168] Alternatively, weaker surfactants, like SDS, forms loose and disordered micelle

structures that only partially cover the nanotube sidewalls.[35] Although the uncovered regions are reactive to subsequent OCC implantations, SDS-stabilized SWCNTs re-bundle more easily and the highest concentration of SDS-stabilized SWCNTs is only ~18 μg/mL,[169] making it difficult to scale up the chemical reaction.

Here, we demonstrate a one-pot synthesis of OCC-SWCNTs capable of producing at the hundreds of mg scale at high concentrations (> 4000 μg/mL) by an efficient reaction process that completes in seconds. This one-pot reaction involves simply mixing raw SWCNTs, an aniline derivative, and NaNO2 in chlorosulfonic acid, and then adding the mixture into nanopure water. We further show that the OCC-SWCNTs can be directly sorted into single-chirality enriched OCC-SWCNTs featuring characteristic defect PL.

6.2. Materials and Methods

6.2.1. Synthesis of OCC-SWCNTs

Raw CoMoCat SG65i (Signa-Aldrich) and HiPco (Rice University, batch number 194.3) SWCNTs were used for this large-scale preparation process. Initially, the SWCNTs were dissolved in superacid (Sigma-Aldrich, 99%) at a concentration of ~4 mg/mL with magnetic stirring, followed by the addition of an aniline derivative at different mole ratios relative to the carbon atoms, and equimolar amounts of sodium nitrite (Sigma Aldrich, ≥ 97.0%). In this work, the SWCNTs were functionalized with a wide variety of aniline derivatives, including 3,5-dinitroaniline (Sigma-Aldrich, 97%), 4-nitroaniline (Sigma-Aldrich, ≥99.0%), 4-aminobenzoic acid (ReagentPlus, ≥99%), 2-fluoro-4-nitroaniline (Sigma-Aldrich, 95%), 4-amino-2-fluorobenzoic acid (Sigma-Aldrich, 97%), 4-amino-3-fluorobenzoic acid (Sigma-Aldrich, 97%), 2-

iodoaniline (Sigma-Aldrich, 98%), 4-chloroaniline (Sigma-Aldrich, 98%), and 4-aminophenol (Sigma-Aldrich, ≥98%). The SWCNT-superacid mixture was then subsequently added drop-by-drop into nanopure water with vigorous stirring. The resulting OCC-SWCNTs instantly precipitate out from the solution. The precipitates were then filtered on an AAO filtration membrane with pore size of 0.02 μm (Whatman Anodisc inorganic filter membrane), thoroughly rinsed with nanopure water, and then dried in a vacuum oven.

6.2.2. Spectroscopic Characterization

The OCC-SWCNTs were stabilized by 2 wt/v% DOC, SDS, CTAB in D_2O and 2 wt/v% PFO-BPy in toluene for PL measurements. The OCC-SWCNTs were dispersed in 2 wt/v% DOC-D_2O by tip ultrasonication with a power of 33 W and at 10 ℃ for 1 h, followed by centrifugation at 16400 rpm for 1 h (Eppendorf centrifuge 5810R) to remove undissolved bundles. The PL spectra and excitation-emission maps of the SWCNT solutions were collected using a HORIBA Jobin Yvon NanoLog spectrofluorometer, with a 450 W xenon arc lamp and a liquid-N_2 cooled InGaAs array. UV-vis-NIR absorption spectra were acquired through a PerkinElmer Lambda 1050 spectrophotometer equipped with a broad InGaAs detector. Raman spectroscopy measurements were performed on a HORIBA Jobin Yvon LabRAM Raman microscope, and the spectrum of each sample was the average data for three different regions.

6.2.3. Hyperspectral Imaging

The OCC-SWCNTs were deposited on an imaging substrate by drop casting 10 μL of the OCC-SWCNT solution (2 wt/v% DOC-D_2O) and immediately blowing dry

with N_2. The imaging substrate consisted of a thin, thermally deposited layer of gold (60 nm Au with a 5 nm thick Ti adhesion layer; Metra Thermal Evaporator) on a silicon wafer to improve the photon collection efficiency. A 50 nm thick polystyrene layer was spin coated on top of the Au to prevent fluorescence quenching. The hyperspectral imaging of the deposited OCC-SWCNTs was then performed on a custom-built shortwave IR imaging system that allows the acquisition of PL spectra from all pixels in the camera frame simultaneously. The OCC-SWCNTs were excited with a 730 nm continuous wave laser (Shanghai Dream Lasers Technology Co., Ltd.) at 64 W cm^{-2}. The resulting fluorescence signal was collected by a 100x objective (LCPLN100XIR, numerical aperture (NA) = 0.85, Olympus) before sending the signal to a volume Bragg grating which was placed in front of the detector in the light path. The detector for the fluorescent signal was a Cougar-640 imaging camera (Xenics, Leuven, Belgium) with an InGaAs focal plane array with 640 × 512 pixels, cooled with liquid nitrogen to -190 °C. An image stack was collected, one wavelength at a time, and reconstructed to provide the PL spectrum for each pixel over the entire field of view.

6.2.4. ATP sorting of OCC-SWCNTs

The reported ATP methods were modified and used to separate OCC-SWCNTs with different chiralities. Briefly 1-part of the OCC-SWCNT 2% (m/v) DOC solution was mixed with 0.3-parts of 20% (m/m) dextran (DX, MW 70000 Da, TCI) and 0.3-parts of 50% polyethylene glycol (PEG, MW 6000 Da, Alfa Aesar) aqueous solution to yield ~0.2-parts of OCC-SWCNTs concentrated in the bottom DX-enriched phase after mild centrifugation at 4000 g for 60 s. DOC surfactants were then gradually replaced by a sodium cholate (SC) and SDS co-surfactant system following the

reported procedure so that the final concentration of SC and SDS were 0.9% (wt/wt) and 0.7% (wt/wt), respectively. The metallic/semiconducting SWCNT sorting process was then applied followed by diameter sorting until the desired chirality was enriched. We note that the OCC-(6,5)-SWCNT, OCC-(7,5)-SWCNT, OCC-(7,6)-SWCNT and OCC-(8,4)-SWCNT were sorted from CoMoCAT SG65i, while the OCC-(8,7)-SWCNT and OCC-(12,1)-SWCNT were derived from the HiPco SWCNT starting material. The PEG and DX polymers were removed from the final semiconducting SWCNT-enriched solution by an ultrafiltration step using a centrifugal ultrafiltration nanotube (Amicon Ultra-15, PLHK Ultracel-PL membrane, 100 kDa) and the surfactants were changed to 2 wt/v% DOC in D_2O solution. Based on optical absorption measurements, the ATPE recovery yield for OCC-(6,5)-SWCNTs is estimated at ~58% after 5 sorting cycles. Note that the purity can be further improved with additional ATPE cycles at the cost of recovery yield.

6.3. Results and Discussion

Figure 6-1a schematically describes this one-pot synthesis of OCC-SWCNTs. As a demonstration of this technique, we mixed raw nanotube powders (CoMoCAT SG 65i), $NaNO_2$, and 3,5-dinitroaniline in chlorosulfonic acid, and then slowly added the mixture into nanopure water. This resulted in the synthesis OCC-SWCNTs, mainly 3,5-dinitroaryl-OCC tailored-(6,5)-SWCNTs (hereafter referred as $C_6H_3(NO_2)_2$-OCC-tailored-(6,5)-SWCNT), as black precipitates, which can be collected via vacuum filtration. We confirmed the covalent modification to the sp^2 carbon lattice by Raman spectroscopy, which reveals a significant increase of the D/G ratio (the intensity of the D peak at ~1300 cm^{-1} to the G peak at ~1600 cm^{-1}) to ~0.5, compared with ~0.1 for the

starting raw SWCNTs (Figure 6-1b,c). This one-pot reaction allows us to synthesize OCC-SWCNTs at the hundreds of milligrams scale in a straightforward manner. Figure 1a shows a batch of $C_6H_3(NO_2)_2$-OCC-tailored-SWCNT weighing ~200 mg.

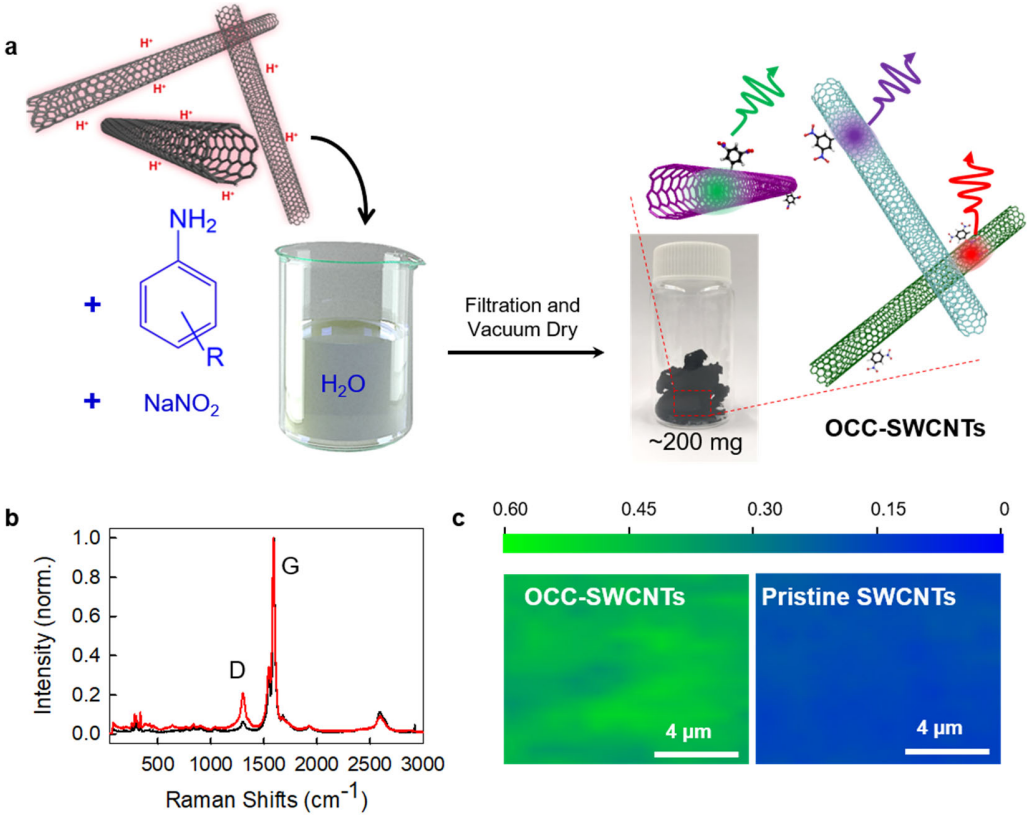

Figure 6-1. A one-pot, large-scale synthesis of OCC-SWCNTs. (a) The reaction occurs by mixing SWCNTs, aniline derivatives, and $NaNO_2$ in chlorosulfonic acid, followed by introducing the mixture into water. (b) Raman scattering from thin films of $C_6H_3(NO_2)_2$-OCC-tailored-SWCNTs (red) and pristine SWCNTs (black), and (c) the spatial maps of the Raman D/G ratios (plotted in color scale). The laser excitation is 633 nm.

To characterize the photoluminescence properties, we dispersed the synthesized $C_6H_3(NO_2)_2$-OCC-tailored-SWCNT material in 2 wt/v% DOC-D_2O and measured the

excitation-emission map (Figure 6-2a). A bright defect PL (E_{11}^-) was observed at ~1160 nm, which is red-shifted by 170 nm (184 meV) from the native E_{11} emission from (6,5)-SWCNT (Figure 6-3a). This E_{11}^- PL originates from the mobile excitons that are efficiently trapped and emit as photons at the OCC defect sites. We note that the OCCs synthesized by this one-pot method exhibit remarkable stability (more than 4 months; and similar high brightness compared to OCCs created by diazonium reactions in aqueous solution.[157]

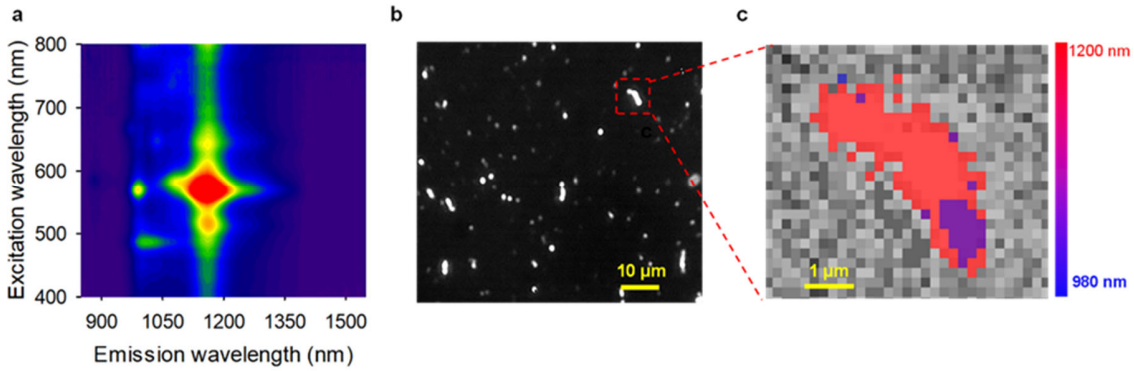

Figure 6-2. $C_6H_3(NO_2)_2$-OCC-tailored-SWCNTs fluoresce brightly in the shortwave infrared. (a) PL excitation-emission map of $C_6H_3(NO_2)_2$-OCC-tailored-SWCNTs in 2 wt/v% DOC-D_2O solution. (b) Single particle PL imaging of $C_6H_3(NO_2)_2$-OCC-tailored-SWCNTs. (c) Hyperspectral PL image of an individual $C_6H_3(NO_2)_2$-OCC-tailored-(6,5)-SWCNT.

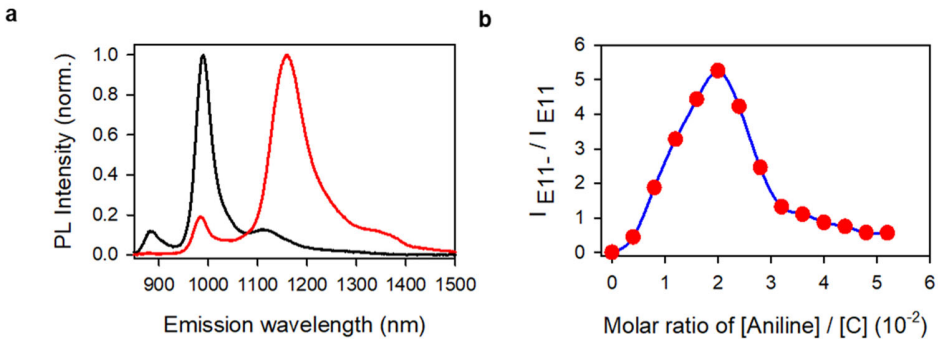

Figure 6-3. (a) PL spectra (at 565 nm excitation) of pristine SWCNTs (black) and OCC-SWCNT-$C_6H_3(NO_2)_2$ (red) dispersed in 2 wt/v% DOC-D_2O solution. (b) The PL intensity ratio of E_{11}^- / E_{11} as a function of the initial relative concentration of aniline and carbon. By adjusting the initial relative amounts of the reagents, the PL intensity of the synthesized OCC-SWCNTs can be controlled.

We further performed hyperspectral fluorescence imaging using a custom-built microscope to investigate the defect PL down to the individual OCC-SWCNT level. Figure 6-2b shows a broadband (1100–1600 nm) PL image of the $C_6H_3(NO_2)_2$-OCC-tailored-SWCNT sample with a longpass filter at 1100 nm to filter out the pristine E_{11} PL emission. Hyperspectral imaging was then performed to resolve the spatial distribution of defects along the length of individual OCC-SWCNTs.[21] Figure 6-2c shows the emission wavelength map of a ~4 μm long (6,5) chirality OCC-SWCNT-$C_6H_3(NO_2)_2$), which features a homogenous defect E_{11}^- PL emission at ~1160 nm along the entire nanotube axis. This indicates uniform sidewall functionalization on SWCNTs, presumably due to the fact that the SWCNTs dispersed in superacid are bare (*i.e.*, without surfactant), thus exposing the whole surface of the material and making it readily accessible to the reactant molecules. We also note that by controlling the

relative amounts of reactants (3,5-dinitroaniline and SWCNTs), the functionalization degree and resulting PL intensity of OCC-SWCNT-$C_6H_3(NO_2)_2$) can be easily controlled. In Figure 6-3b, we show that the defect PL intensity of $C_6H_3(NO_2)_2$-OCC-tailored-(6,5)-SWCNT reaches its maximum at a reactant to carbon molar ratio ([aniline]:[C]) of ~1:50 (note that the carbons in this case are from all nanotube chiralities and other carbon species in the starting SG65i raw material). Excessive reaction ultimately quenches both the PL of E_{11} and E_{11}^-.

Because the optical behavior of an OCC is strongly dependent on the chemical nature of the defect,[157, 163] the tunability of the functional group is particularly valuable for OCC chemistries. Figure 6-4 shows the PL spectra of OCC-SWCNTs functionalized by a wide variety of aniline derivatives, including fluoroaniline and aminobenzoic acid derivatives, some of them (*e.g.,* 2-fluoro-4-nitroaniline, 4-amino-2-fluorobenzoic acid and 4-amino-2,3,5,6-tetrafluorobenzoic acid) have never been achieved in aqueous-based reactions due to the difficulty in synthesizing the corresponding diazonium salts, demonstrating the versatility of this one-pot chemistry.

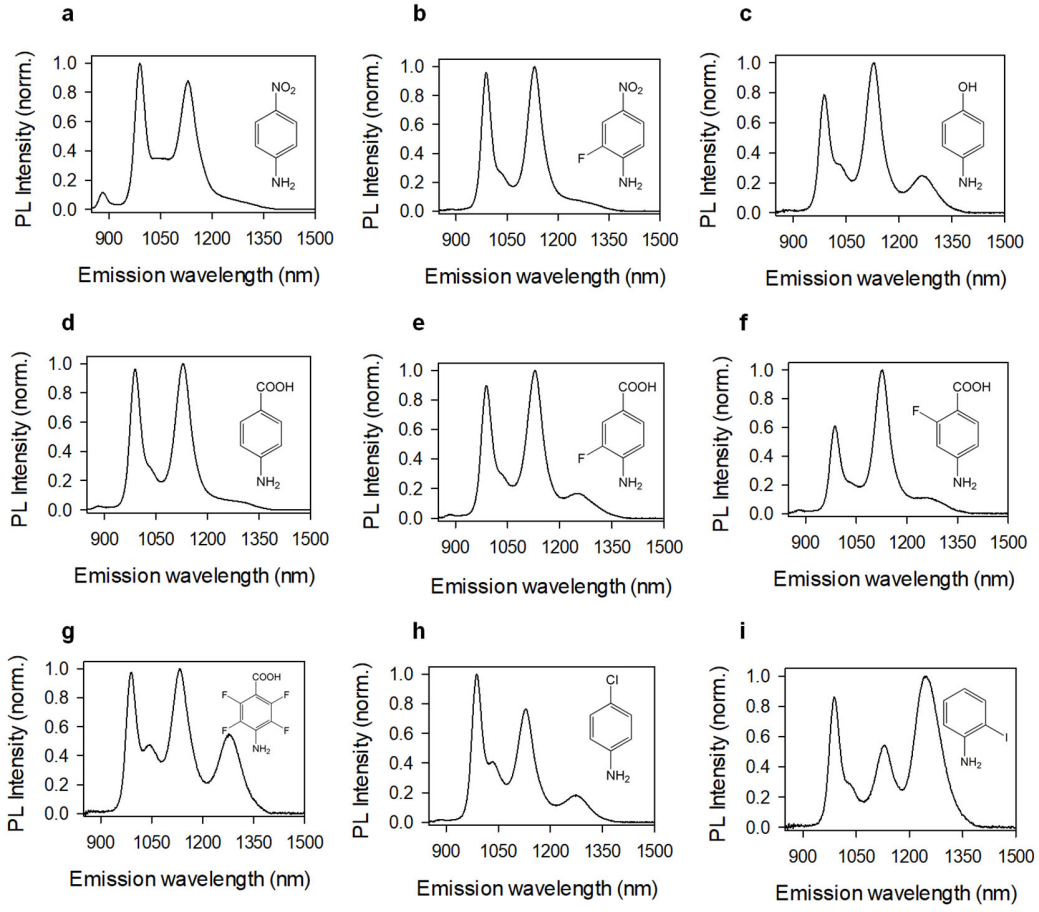

Figure 6-4. The PL spectra (at 565 nm excitation) of OCC-SWCNTs tailored with a wide variety of aniline OCCs, including (a) 4-nitroaniline, (b) 2-fluoro-4-nitroaniline, (c) 4-aminophenol, (d) 4-aminobenzoic acid, (e) 4-amino-2-fluorobenzoic acid, (f) 4-amino-3-fluorobenzoic acid, (g) 4-amino-2,3,5,6-tetrafluorobenzoic acid, (h) 4-chloroaniline, and (i) 2-iodoaniline. The OCC-SWCNTs were stabilized as individual particles in 2 wt/v% DOC-D2O solution. We note that 2-fluoro-4-nitro-aryl (b), 4-amino-2-fluorobenzoic acid (e), and 4-amino-2,3,5,6-tetrafluorobenzoic acid (g) OCCs were synthetically achieved for the first time, enabled by this one-pot reaction.

We further show that long, individually dispersed OCC-SWCNTs can be directly obtained by superacid-surfactant exchange (S2E) by simply adding the superacid-SWCNTs-reactants mixture into a DOC/NaOH solution.[55, 90] We note that the resulting OCC-SWCNTs exhibit much lower E_{11}^- PL emission when compared with that of water-quenched OCC-SWCNTs (Figure 6-5). This is possibly due to competition between the DOC surfactant and the reactant molecules in coating the exposed SWCNTs as the chlorosulfonic acid leaves. DOC coating of the nanotube surfaces will prevent the further attachment of aniline molecules to the carbon lattice. We addressed this problem by re-dissolving the solid OCC-SWCNTs materials in the superacid and then performed S2E as a separate step. In this manner, we were able to obtain OCC-SWCNTs with an average length of ~1.55 μm (Figure 6-6) that exhibited much brighter E_{11}^- PL (Figure 6-7).

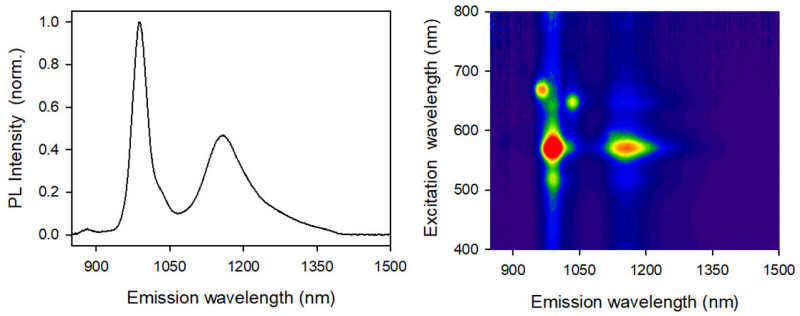

Figure 6-5. PL spectrum (at 565 nm excitation) and excitation-emission map of the OCC-SWCNT-$C_6H_3(NO_2)_2$ sample that was directly stabilized by the S2E process.

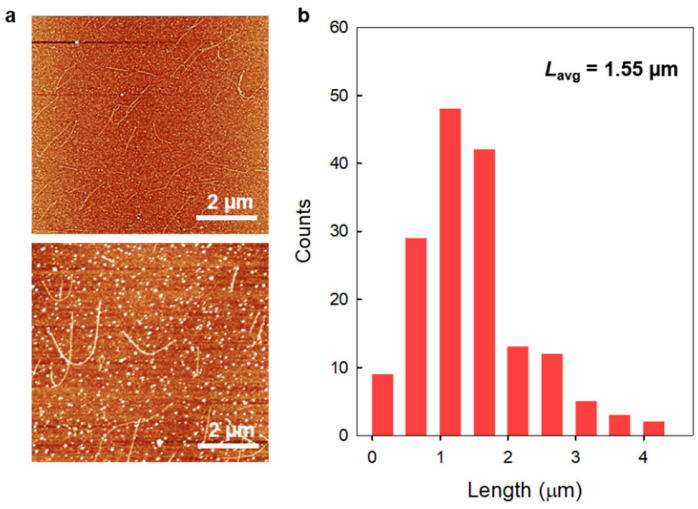

Figure 6-6. AFM imaging and length distribution of the OCC-SWCNT-$C_6H_3(NO_2)_2$ sample produced from the separate S2E step.

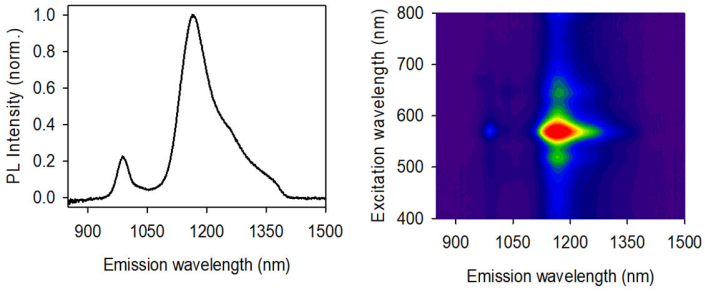

Figure 6-7. PL spectrum (at 565 nm excitation) and excitation-emission map of the OCC-SWCNT-$C_6H_3(NO_2)_2$ sample produced from the separate S2E step.

In addition to the scalability, another significant advantage of this synthetic route is that OCC-SWCNTs are produced as solid bulk materials, which we hypothesized could be dissolved into a wide spectrum of solvents with different surfactants or polymers, depending on the specific requirements of subsequent

processing steps necessary for different applications. For instance, in the case of biomedical imaging and therapy, surfactant molecules are typically highly toxic and cause biocompatibility concerns.[22] Also, excess free surfactant molecules that are not physically adsorbed on the SWCNTs are difficult to remove from the solution, creating an obstacle to the further conjugation of SWCNTs with imaging labels or bioactive molecules. Although prolonged dialysis can be used to exchange the bioincompatible surfactants (such as SDS) to other biocompatible and stable molecules, the method is highly time-consuming and the recovery rate is usually very low (< 30%).[170]

Here, we demonstrate that the resulting OCC-SWCNTs can be stabilized by a wide variety of surfactants and polymers, including SDS, cetrimonium bromide (CTAB), and DNA in D_2O and PFO-BPy in toluene, all of which exhibit bright defect PL (Figure 6-8). The relatively low E_{11}^{-}/E_{11} ratio of the PFO-BPy wrapped OCC-SWCNTs dispersed in toluene can be attributed to the strong optical absorption of the toluene solvent at the wavelengths from 1100 to 1250 nm (Figure 6-9), which overlaps with the E_{11}^{-} emission. It is noteworthy that the PFO-BPy wrapped OCC-SWCNTs dispersed in toluene show E_{11}^{-} emission with a much narrower full width at half maximum (fwhm) of ~63 meV compared with those dispersed in aqueous solution (~96 meV, and 103 meV for SDS and CTAB, respectively). This is possibly due to the absence of charge transfer from the nanotube OCCs to the nonpolar toluene solvent and may also affected by the optical absorption from toluene.

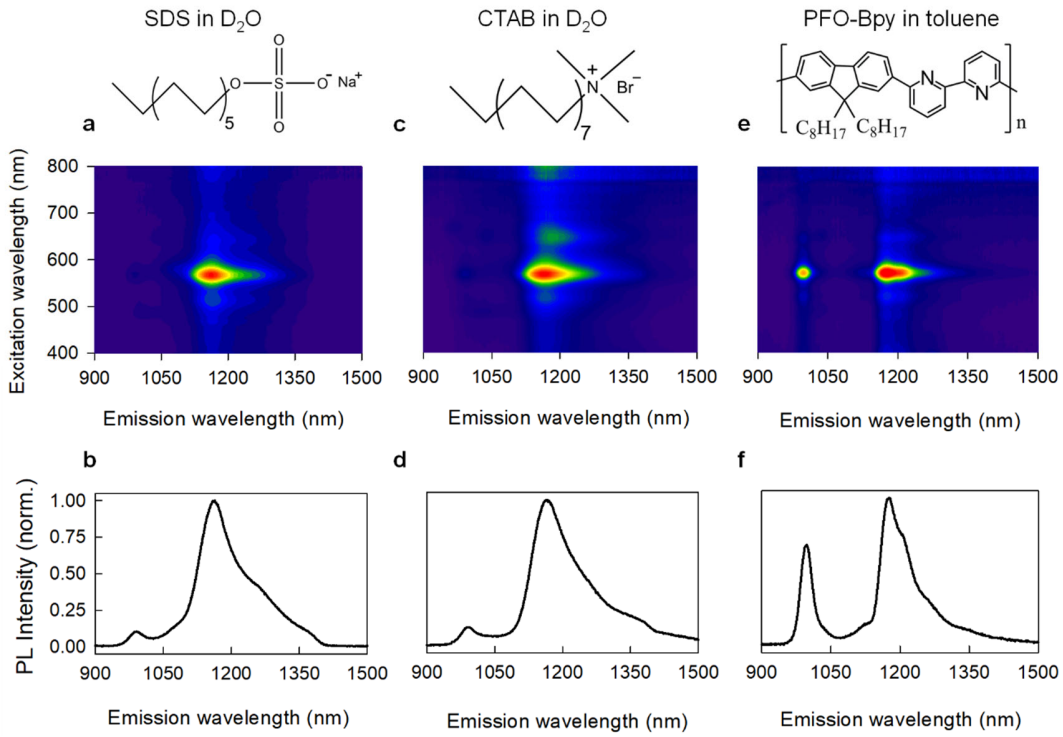

Figure 6-8. Individual OCC-SWCNTs encapsulated directly by various molecules and polymers. PL excitation-emission maps and spectra (565 nm excitation) of $C_6H_3(NO_2)_2$-OCC-tailored-SWCNTs that are directly dispersed in (a, b) 2 wt/v% SDS, (c, d) CTAB in D_2O, and (e, f) PFO-BPy in toluene.

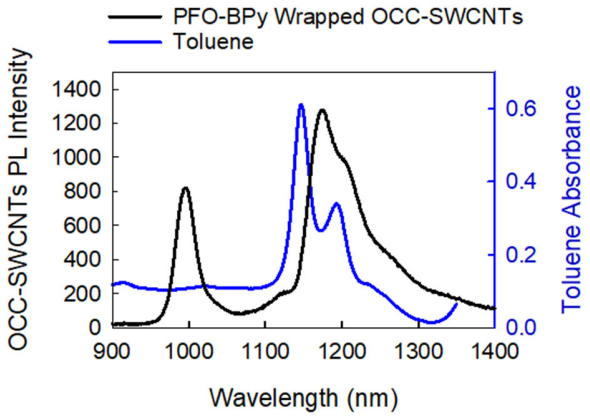

Figure 6-9. The PL spectrum (565 nm excitation) of PFO-BPy wrapped OCC-SWCNTs in toluene (black) and the absorption spectrum of toluene (blue). The wavelengths overlapping between the toluene absorption and E_{11}^{-} emission must have contributed to a smaller E_{11}^{-}/E_{11} ratio than that of OCC-SWCNTs dispersed in aqueous solution.

Single chirality SWCNTs possess characteristic optical absorption and emission because of their distinct electronic band structure. For single chirality OCC-SWCNTs,[157] the unique optical properties include not only the native PL features of the nanotube host, but also the added defect PL, both of which are important to fully exploit the extraordinary PL properties for practical applications in optoelectronics. For example, single chirality OCC-SWCNTs are sought after as high purity single photon sources for quantum information processes.[171]

We show that the synthesized OCC-SWCNTs can be sorted by adopting established nanotube purification techniques such as aqueous two-phase extraction (ATPE). Here we developed an ATPE recipe that allows us to directly sort OCC-SWCNTs to attain single chirality-enriched fractions at large volume. (Figure 6-10). Figure 6-11a-d show four sorted solutions of $C_6H_3(NO_2)_2$-OCC-tailored-SWCNTs, including OCC-(6,5)-SWCNT, OCC-(7,5)-SWCNT, OCC-(7,6)-SWCNT, OCC-(8,7)-SWCNT. We note that the $C_6H_3(NO_2)_2$-OCC-tailored-(8,7)-SWCNT fraction also contained some OCC-(12,1)-SWCNT. To avoid the strong water absorption at wavelengths greater than ~1350 nm, we measured the E_{11}^{-} peaks of the larger diameter $C_6H_3(NO_2)_2$-OCC-tailored (12,1)-SWCNT and (8,7)-SWCNT in solid state by

hyperspectral imaging (Figure 6-12). We observed that as the diameter of the host nanotube increases, the E_{11}^{-} emission from the OCCs redshifted from ~1160 nm in the smallest (6,5) host to ~1510 nm in the largest (8,7) host (Figure 6-9e). This diameter dependent relationship is consistent with previous results and is due to the different exciton trapping potentials in hosts of different diameters. The general correlation between E_{11}^{-} with the host nanotube diameter is further shown in Figure 6-11f. Notably, the (8,7) chirality is one of the largest diameter (~1.02 nm) SWCNTs ever reported, and the corresponding OCC-SWCNT sample features the most redshifted E_{11}^{-} emission of up to ~1510 nm, which falls within the telecommunication range. This result is significant in that SWCNTs with large dimeters are difficult to functionalize in aqueous solution due to their relatively high structural stability and low reactivity.[32] Therefore, this superacid-based synthetic route shows great potential for effectively functionalizing SWCNTs with large diameters and paves the way for further study and application of OCCs in large diameter nanotube hosts.

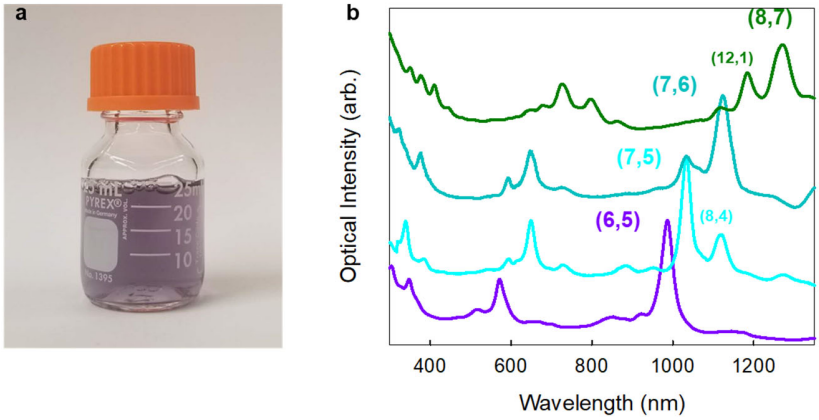

Figure 6-10. (a) 25 mL of the ATP-sorted (6,5) chirality enriched OCC-SWCNT-$C_6H_3(NO_2)_2$. (b) UV-vis-NIR absorption spectra of ATP-sorted OCC-SWCNT-$C_6H_3(NO_2)_2$.

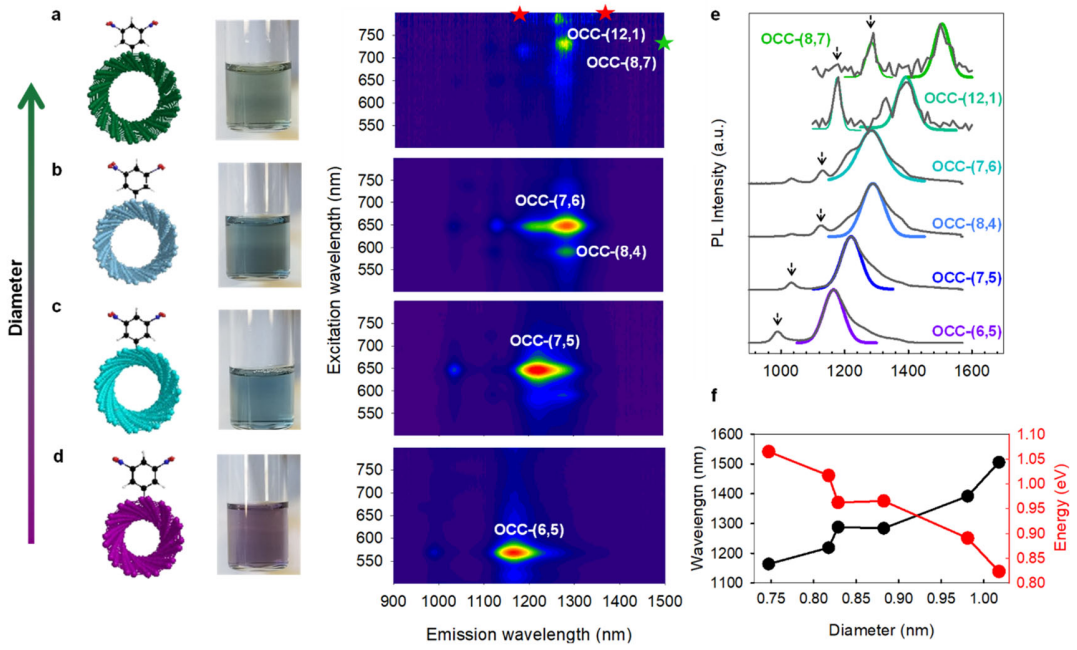

Figure 6-11. ATP-sorting of OCC-SWCNTs to yield large-scale single chirality enriched OCC-SWCNTs. DOC-D_2O Solutions of (a) (8,7), (b) (7,6), (c) (7,5), and (d) (6,5)-enriched OCC-SWCNT-$C_6H_3(NO_2)_2$, along with their corresponding PL excitation-emission maps. Due to the strong water absorption above the wavelength of 1350 nm, the E_{11}^- peak could not be directly detected in the aqueous solutions of (12,1) and (8,7) OCC-SWCNT-$C_6H_3(NO_2)_2$. Green and red stars in (a) are the peak positions measured by the solid-state PL hyperspectral imager. (e) PL spectra of OCC-SWCNT-$C_6H_3(NO_2)_2$ made from different chiralities. The spectra were fitted with Voigt functions. The red arrows indicate the E_{11} wavelength of (12,1) and (8,7) OCC-

SWCNTs-$C_6H_3(NO_2)_2$. (f) The correlation of E_{11}^- with the host nanotube diameters for OCC-SWCNT-$C_6H_3(NO_2)_2$.

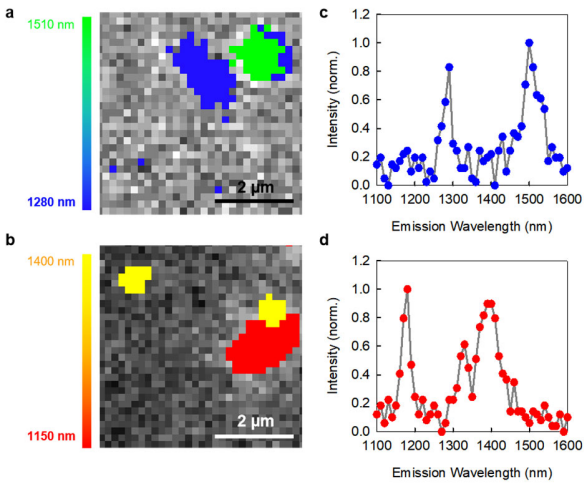

Figure 6-12. Hyperspectral PL images and corresponding PL emission spectra of $C_6H_3(NO_2)_2$-OCC-tailored-(8,7)-SWCNT (a, c) and $C_6H_3(NO_2)_2$-OCC-tailored-(12,1)-SWCNT (b, d).

6.4. Conclusions

We show that large-scale synthesis of organic color center-tailored SWCNTs can be achieved by simply mixing SWCNTs, $NaNO_2$, and an aniline derivative in chlorosulfonic acid, then introducing the mixture into water. Compared with existing OCC chemistries, our one-pot reaction features significant advantages, including: (1) the reaction occurs efficiently even at ultrahigh concentrations (> 4000 μg/mL), making it readily scalable to synthesize large quantities of OCC-SWCNTs; (2) no surfactants or polymers are required to disperse the SWCNTs, thus the nanotube surfaces are "bare", free from molecular coating, and completely accessible for OCC implantation;

(3) the reaction completes in seconds (versus days for aqueous diazonium salt reactions[1]); and (4) distinct from existing methods that require surfactant dispersion and work only for certain surfactants, [cite]our method produces neat OCC-SWCNTs that can be directly encapsulated by specialized molecules/polymers that are required for subsequent applications (*e.g.,* chiral purification of OCC-SWCNTs). This facile, efficient, and scalable method has thus made large quantities of OCC-SWCNTs synthetically accessible for a broad range of applications in imaging, sensing and quantum information processing

7. Summary and Outlook

In summary, this thesis demonstrates a novel strategy that is called the superacid-surfactant exchange to nondestructively disperse CNTs as individual nanotubes in water. CNTs were first dissolved in superacid and subsequently added to a NaOH solution containing DOC surfactant, such that the CNTs were instantly stabilized by the surfactant molecules. Due to the elimination of the sonication throughout the whole process, CNTs obtained by this novel method are significantly longer than the sonicated controls. We further show that by tuning the concentration of SWCNTs in superacid, long SWCNTs can be self-sorted from those short counterparts during the S2E process.

The resulting long CNTs are used to build devices and macroscopic objects that show extraordinary properties. Particularly, we show that transparent conductive film fabricated from long SWCNTs exhibit electrical conductivity surpassing that of the ITO films, thin-film transistors from long, semiconducting SWCNTs demonstrate the carrier mobility approaching that of p-type polycrystalline Si, and long metallic DWCNTs can be used to build stretchable transparent conductors that achieve high transparency, stretchability and conductivity at the same time.

We also show that long SWCNTs can be used to enhance the mechanical strength of the graphene material. A mechanically strong, conductive and transparent graphene+SWCNTs hybrid film was built and enabled us to directly observe the formation and dynamic change of the electrical double layer formed at the electrode-electrolyte interface. Last, we demonstrate that sidewall functionalization of SWCNTs

can be achieved by directly quenching the superacid SWCNTs mixture with water in the presence of sodium nitrite and aniline derivatives.

The techniques reported here open new opportunities to address many fundamental questions that are yet to be answered and enable new applications.

Armchair SWCNTs (armchair metals) are SWCNTs with chiral vector of (n,n) and possess a unique electronic structure.[4, 5] Unlike other SWCNTs that are either semiconducting with a finite band gap or quasi-metallic with a very small band gap, armchair metals present a truly gapless electronic structure with massless carriers and two conduction channels, which originates from the linear dispersion relations of the graphene Brillouin zone together with one-dimensional (1D) confinement in armchair metals. Because of this truly gapless electronic structure, armchair metals can be viewed as unconventional 1D metals with long diffusion lengths and quantum transport.[5] The combination of high mechanical strength, mechanical flexibility owing to their high aspect ratio, and tunable optical transparency in the visible range make armchair metals ideal materials for high-performance electronic applications, such as flexible nanocircuit components, power transmission cables, and transparent conductors. Nevertheless, the full potential of armchair metals remains largely untapped due to the lack of a long and chirality pure SWCNTs. In this context, long SWCNTs prepared by S2E method should have strong potential to produce full-length, high-purity armchair metals to enable the proposed applications.

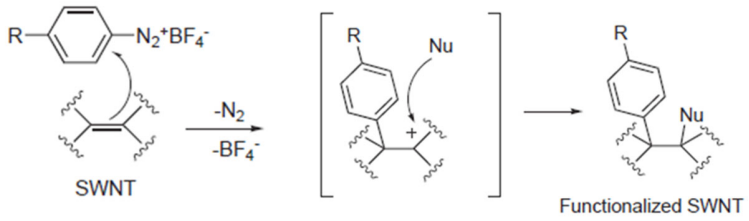

Figure 7-1. Proposed two-step reaction mechanism for functionalization of SWCNTs by diazonium chemistry.

In chapter 6, we demonstrated that, contrary to the previous belief, the functionalization of SWCNTs actually occurs during the acid quenching process and H_2O is an indispensable reagent for the reaction. So, the next question is "what is the role of H_2O in this diazonium chemistry". The mechanism for the implantation of a sp^3 defect site on the sp^2 carbon nanotube lattice usually involves two steps: (1) a C-C σ bond was first formed between a aryl group and SWCNT due to the addition of an electron from the SWCNTs to the diazonium salt, yielding an aryl-SWCNT cation; (2) a nucleophile then react with the aryl-SWCNT cation to form another C-C σ bond. (Figure 7-1) In this context, H_2O molecules should behave like a nucleophile agent that form an OH group at the neighboring position of the aryl defect site. On the other hand, due to the conjugation of sp^2 carbon lattice, the cation may migrate to the adjacent carbon atoms, resulting possibilities of the addition of second C-C σ bond at different neighboring sites. Doorn and coworkers have shown that different positions of the second moiety change the overall binding configurations of the defect sites and eventually change the emission energy of the defect photoluminescence.[158, 164] Therefore, this simple quenching experiment may allow us to understand and provide

opportunities to precisely control the binding configurations of defect sites on SWCNTs and the resulting defect light emission. Related experiments are under active exploration.

Bibliography

1. Wang, X.; Li, Q.; Xie, J.; Jin, Z.; Wang, J.; Li, Y.; Jiang, K.; Fan, S., Fabrication of ultralong and electrically uniform single-walled carbon nanotubes on clean substrates. *Nano Lett.* **2009**, *9* (9), 3137-3141.
2. Dresselhaus, G.; Riichiro, S., *Physical properties of carbon nanotubes*. World scientific: 1998.
3. Shen, C.; Brozena, A. H.; Wang, Y., Double-walled carbon nanotubes: challenges and opportunities. *Nanoscale* **2011,** *3* (2), 503-518.
4. Chen, Y.; Shen, Z.; Xu, Z.; Hu, Y.; Xu, H.; Wang, S.; Guo, X.; Zhang, Y.; Peng, L.; Ding, F., Helicity-dependent single-walled carbon nanotube alignment on graphite for helical angle and handedness recognition. *Nat. Commun.* **2013,** *4*, 2205.
5. Tans, S. J.; Devoret, M. H.; Dai, H.; Thess, A.; Smalley, R. E.; Geerligs, L.; Dekker, C., Individual single-wall carbon nanotubes as quantum wires. *Nature* **1997,** *386* (6624), 474.
6. Yao, Z.; Kane, C. L.; Dekker, C., High-field electrical transport in single-wall carbon nanotubes. *Phys. Rev. Lett.* **2000,** *84* (13), 2941.
7. Odom, T. W.; Huang, J.-L.; Kim, P.; Lieber, C. M., Atomic structure and electronic properties of single-walled carbon nanotubes. *Nature* **1998,** *391* (6662), 62.
8. Kong, J.; Yenilmez, E.; Tombler, T. W.; Kim, W.; Dai, H.; Laughlin, R. B.; Liu, L.; Jayanthi, C.; Wu, S., Quantum interference and ballistic transmission in nanotube electron waveguides. *Phys. Rev. Lett.* **2001,** *87* (10), 106801.
9. Dürkop, T.; Getty, S.; Cobas, E.; Fuhrer, M., Extraordinary mobility in semiconducting carbon nanotubes. *Nano Lett.* **2004,** *4* (1), 35-39.
10. Smith, A. M.; Mancini, M. C.; Nie, S., Bioimaging: second window for in vivo imaging. *Nat. Nanotechnol.* **2009,** *4* (11), 710.
11. O'connell, M. J.; Bachilo, S. M.; Huffman, C. B.; Moore, V. C.; Strano, M. S.; Haroz, E. H.; Rialon, K. L.; Boul, P. J.; Noon, W. H.; Kittrell, C., Band gap fluorescence from individual single-walled carbon nanotubes. *Science* **2002,** *297* (5581), 593-596.
12. Wang, F.; Dukovic, G.; Brus, L. E.; Heinz, T. F., The optical resonances in carbon nanotubes arise from excitons. *Science* **2005,** *308* (5723), 838-841.
13. Yao, N.; Lordi, V., Young's modulus of single-walled carbon nanotubes. *J. Appl. Phys.* **1998,** *84* (4), 1939-1943.
14. Yu, M.-F.; Files, B. S.; Arepalli, S.; Ruoff, R. S., Tensile loading of ropes of single wall carbon nanotubes and their mechanical properties. *Phys. Rev. Lett.* **2000,** *84* (24), 5552.
15. Lu, J. P., Elastic properties of carbon nanotubes and nanoropes. *Phys. Rev. Lett.* **1997,** *79* (7), 1297.
16. Javey, A.; Guo, J.; Wang, Q.; Lundstrom, M.; Dai, H., Ballistic carbon nanotube field-effect transistors. *Nature* **2003,** *424* (6949), 654.
17. Dekker, C., How we made the carbon nanotube transistor. *Nat. Electron.* **2018,** *1* (9), 518.
18. Park, S.; Vosguerichian, M.; Bao, Z., A review of fabrication and applications of carbon nanotube film-based flexible electronics. *Nanoscale* **2013,** *5* (5), 1727-1752.

19. Wang, S.; Zeng, Q.; Yang, L.; Zhang, Z.; Wang, Z.; Pei, T.; Ding, L.; Liang, X.; Gao, M.; Li, Y., High-performance carbon nanotube light-emitting diodes with asymmetric contacts. *Nano Lett.* **2010,** *11* (1), 23-29.
20. Fedorov, G.; Kardakova, A.; Gayduchenko, I.; Charayev, I.; Voronov, B.; Finkel, M.; Klapwijk, T.; Morozov, S.; Presniakov, M.; Bobrinetskiy, I., Photothermoelectric response in asymmetric carbon nanotube devices exposed to sub-terahertz radiation. *Appl. Phys. Lett* **2013,** *103* (18), 181121.
21. Hong, G.; Lee, J. C.; Robinson, J. T.; Raaz, U.; Xie, L.; Huang, N. F.; Cooke, J. P.; Dai, H., Multifunctional in vivo vascular imaging using near-infrared II fluorescence. *Nat. Med.* **2012,** *18* (12), 1841.
22. Hong, G.; Diao, S.; Antaris, A. L.; Dai, H., Carbon nanomaterials for biological imaging and nanomedicinal therapy. *Chem. Rev.* **2015,** *115* (19), 10816-10906.
23. Xu, W.; Chen, Y.; Zhan, H.; Wang, J. N., High-strength carbon nanotube film from improving alignment and densification. *Nano Lett.* **2016,** *16* (2), 946-952.
24. Hecht, D. S.; Hu, L.; Irvin, G., Emerging transparent electrodes based on thin films of carbon nanotubes, graphene, and metallic nanostructures. *Adv. Mater.* **2011,** *23* (13), 1482-1513.
25. Tsentalovich, D. E.; Headrick, R. J.; Mirri, F.; Hao, J.; Behabtu, N.; Young, C. C.; Pasquali, M., Influence of carbon nanotube characteristics on macroscopic fiber properties. *ACS Appl. Mater. Interfaces* **2017,** *9* (41), 36189-36198.
26. Headrick, R. J.; Tsentalovich, D. E.; Berdegué, J.; Bengio, E. A.; Liberman, L.; Kleinerman, O.; Lucas, M. S.; Talmon, Y.; Pasquali, M., Structure–property relations in carbon nanotube fibers by downscaling solution processing. *Adv. Mater.* **2018,** *30* (9), 1704482.
27. Kamalasanan, K.; Gottardi, R.; Tan, S.; Chen, Y.; Godugu, B.; Rothstein, S.; Balazs, A. C.; Star, A.; Little, S. R., ″Zero-Dimensional″ Single-Walled Carbon Nanotubes. *Angew. Chemie.* **2013,** *52* (43), 11308-11312.
28. Danné, N. M.; Kim, M.; Godin, A. G.; Kwon, H.; Gao, Z.; Wu, X.; Hartmann, N. F.; Doorn, S. K.; Lounis, B.; Wang, Y., Ultrashort carbon nanotubes that fluoresce brightly in the near-infrared. *ACS Nano* **2018,** *12* (6), 6059-6065.
29. Lu, K.; Lago, R.; Chen, Y.; Green, M.; Harris, P.; Tsang, S., Mechanical damage of carbon nanotubes by ultrasound. *Carbon* **1996,** *34* (6).
30. Pagani, G.; Green, M. J.; Poulin, P.; Pasquali, M., Competing mechanisms and scaling laws for carbon nanotube scission by ultrasonication. *Proc. Natl. Acad. Sci.* **2012,** *109* (29), 11599-11604.
31. Lucas, A.; Zakri, C.; Maugey, M.; Pasquali, M.; van der Schoot, P.; Poulin, P., Kinetics of Nanotube and Microfiber Scission under Sonication. *J. Phys. Chem. C* **2009,** *113* (48), 20599-20605.
32. Dyke, C. A.; Tour, J. M., Covalent functionalization of single-walled carbon nanotubes for materials applications. *J. Phys. Chem. A* **2004,** *108* (51), 11151-11159.
33. Hudson, J. L.; Casavant, M. J.; Tour, J. M., Water-soluble, exfoliated, nonroping single-wall carbon nanotubes. *J. Am. Chem. Soc.* **2004,** *126* (36), 11158-11159.
34. Haggenmueller, R.; Rahatekar, S. S.; Fagan, J. A.; Chun, J.; Becker, M. L.; Naik, R. R.; Krauss, T.; Carlson, L.; Kadla, J. F.; Trulove, P. C., Comparison of the

quality of aqueous dispersions of single wall carbon nanotubes using surfactants and biomolecules. *Langmuir* **2008,** *24* (9), 5070-5078.
35. Wenseleers, W.; Vlasov, I. I.; Goovaerts, E.; Obraztsova, E. D.; Lobach, A. S.; Bouwen, A., Efficient isolation and solubilization of pristine single-walled nanotubes in bile salt micelles. *Adv. Funct. Mater.* **2004,** *14* (11), 1105-1112.
36. Tulevski, G. S.; Franklin, A. D.; Afzali, A., High purity isolation and quantification of semiconducting carbon nanotubes via column chromatography. *ACS Nano* **2013,** *7* (4), 2971-2976.
37. Liu, H.; Nishide, D.; Tanaka, T.; Kataura, H., Large-scale single-chirality separation of single-wall carbon nanotubes by simple gel chromatography. *Nat. Commun.* **2011,** *2*, 309.
38. Ghosh, S.; Bachilo, S. M.; Weisman, R. B., Advanced sorting of single-walled carbon nanotubes by nonlinear density-gradient ultracentrifugation. *Nat. Nanotechnol.* **2010,** *5* (6), 443.
39. Arnold, M. S.; Green, A. A.; Hulvat, J. F.; Stupp, S. I.; Hersam, M. C., Sorting carbon nanotubes by electronic structure using density differentiation. *Nat. Nanotechnol.* **2006,** *1* (1), 60.
40. Ao, G.; Khripin, C. Y.; Zheng, M., DNA-controlled partition of carbon nanotubes in polymer aqueous two-phase systems. *J. Am. Chem. Soc.* **2014,** *136* (29), 10383-10392.
41. Fagan, J. A.; Khripin, C. Y.; Silvera Batista, C. A.; Simpson, J. R.; Hároz, E. H.; Hight Walker, A. R.; Zheng, M., Isolation of specific small-diameter single-wall carbon nanotube species via aqueous two-phase extraction. *Adv. Mater.* **2014,** *26* (18), 2800-2804.
42. Fagan, J. A.; Hároz, E. H.; Ihly, R.; Gui, H.; Blackburn, J. L.; Simpson, J. R.; Lam, S.; Hight Walker, A. R.; Doorn, S. K.; Zheng, M., Isolation of> 1 nm diameter single-wall carbon nanotube species using aqueous two-phase extraction. *ACS Nano* **2015,** *9* (5), 5377-5390.
43. Khripin, C. Y.; Fagan, J. A.; Zheng, M., Spontaneous partition of carbon nanotubes in polymer-modified aqueous phases. *J. Am. Chem. Soc.* **2013,** *135* (18), 6822-6825.
44. Zheng, M.; Jagota, A.; Semke, E. D.; Diner, B. A.; McLean, R. S.; Lustig, S. R.; Richardson, R. E.; Tassi, N. G., DNA-assisted dispersion and separation of carbon nanotubes. *Nat. Mater.* **2003,** *2* (5), 338.
45. Tu, X.; Manohar, S.; Jagota, A.; Zheng, M., DNA sequence motifs for structure-specific recognition and separation of carbon nanotubes. *Nature* **2009,** *460* (7252), 250.
46. Arnold, M. S.; Stupp, S. I.; Hersam, M. C., Enrichment of single-walled carbon nanotubes by diameter in density gradients. *Nano Lett.* **2005,** *5* (4), 713-718.
47. Nish, A.; Hwang, J.-Y.; Doig, J.; Nicholas, R. J., Highly selective dispersion of single-walled carbon nanotubes using aromatic polymers. *Nat. Nanotechnol.* **2007,** *2* (10), 640.
48. Samanta, S. K.; Fritsch, M.; Scherf, U.; Gomulya, W.; Bisri, S. Z.; Loi, M. A., Conjugated polymer-assisted dispersion of single-wall carbon nanotubes: the power of polymer wrapping. *Acc. Chem. Res.* **2014,** *47* (8), 2446-2456.

49. Lei, T.; Pochorovski, I.; Bao, Z., Separation of semiconducting carbon nanotubes for flexible and stretchable electronics using polymer removable method. *Acc. Chem. Res.* **2017,** *50* (4), 1096-1104.
50. Ramesh, S.; Ericson, L. M.; Davis, V. A.; Saini, R. K.; Kittrell, C.; Pasquali, M.; Billups, W.; Adams, W. W.; Hauge, R. H.; Smalley, R. E., Dissolution of pristine single walled carbon nanotubes in superacids by direct protonation. *J. Phys. Chem. B* **2004,** *108* (26), 8794-8798.
51. Davis, V. A.; Parra-Vasquez, A. N. G.; Green, M. J.; Rai, P. K.; Behabtu, N.; Prieto, V.; Booker, R. D.; Schmidt, J.; Kesselman, E.; Zhou, W., True solutions of single-walled carbon nanotubes for assembly into macroscopic materials. *Nat. Nanotechnol.* **2009,** *4* (12), 830.
52. Behabtu, N.; Young, C. C.; Tsentalovich, D. E.; Kleinerman, O.; Wang, X.; Ma, A. W.; Bengio, E. A.; ter Waarbeek, R. F.; de Jong, J. J.; Hoogerwerf, R. E., Strong, light, multifunctional fibers of carbon nanotubes with ultrahigh conductivity. *Science* **2013,** *339* (6116), 182-186.
53. Mirri, F.; Ma, A. W.; Hsu, T. T.; Behabtu, N.; Eichmann, S. L.; Young, C. C.; Tsentalovich, D. E.; Pasquali, M., High-performance carbon nanotube transparent conductive films by scalable dip coating. *ACS Nano* **2012,** *6* (11), 9737-9744.
54. Cremlyn, R. J. W., *Chlorosulfonic Acid*. Royal Society of Chemistry: 2002.
55. Wang, P.; Kim, M.; Peng, Z.; Sun, C.-F.; Mok, J.; Lieberman, A.; Wang, Y., Superacid-surfactant exchange: enabling nondestructive dispersion of full-length carbon nanotubes in water. *ACS Nano* **2017,** *11* (9), 9231-9238.
56. Girifalco, L.; Hodak, M.; Lee, R. S., Carbon nanotubes, buckyballs, ropes, and a universal graphitic potential. *Physical Review B* **2000,** *62* (19), 13104.
57. Cognet, L.; Tsyboulski, D. A.; Rocha, J.-D. R.; Doyle, C. D.; Tour, J. M.; Weisman, R. B., Stepwise quenching of exciton fluorescence in carbon nanotubes by single-molecule reactions. *Science* **2007,** *316* (5830), 1465-1468.
58. Tabakman, S. M.; Welsher, K.; Hong, G.; Dai, H., Optical properties of single-walled carbon nanotubes separated in a density gradient: length, bundling, and aromatic stacking effects. *J. Phys. Chem. C* **2010,** *114* (46), 19569-19575.
59. Subbaiyan, N. K.; Parra-Vasquez, A. N. G.; Cambré, S.; Cordoba, M. A. S.; Yalcin, S. E.; Hamilton, C. E.; Mack, N. H.; Blackburn, J. L.; Doorn, S. K.; Duque, J. G., Bench-top aqueous two-phase extraction of isolated individual single-walled carbon nanotubes. *Nano Res.* **2015,** *8* (5), 1755-1769.
60. Graf, A.; Zakharko, Y.; Schießl, S. P.; Backes, C.; Pfohl, M.; Flavel, B. S.; Zaumseil, J., Large scale, selective dispersion of long single-walled carbon nanotubes with high photoluminescence quantum yield by shear force mixing. *Carbon* **2016,** *105*, 593-599.
61. Wu, Z.; Chen, Z.; Du, X.; Logan, J. M.; Sippel, J.; Nikolou, M.; Kamaras, K.; Reynolds, J. R.; Tanner, D. B.; Hebard, A. F., Transparent, conductive carbon nanotube films. *Science* **2004,** *305* (5688), 1273-1276.
62. Roxbury, D.; Jena, P. V.; Williams, R. M.; Enyedi, B.; Niethammer, P.; Marcet, S.; Verhaegen, M.; Blais-Ouellette, S.; Heller, D. A., Hyperspectral microscopy of near-infrared fluorescence enables 17-chirality carbon nanotube imaging. *Sci. Rep.* **2015,** *5*, 14167.

63. Hersam, M. C., Progress towards monodisperse single-walled carbon nanotubes. *Nat. Nanotechnol.* **2008,** *3* (7), 387.
64. De Volder, M. F.; Tawfick, S. H.; Baughman, R. H.; Hart, A. J., Carbon nanotubes: present and future commercial applications. *Science* **2013,** *339* (6119), 535-539.
65. Wang, P.; Barnes, B.; Wu, X.; Qu, H.; Zhang, C.; Shi, Y.; Headrick, R. J.; Pasquali, M.; Wang, Y., Self-Sorting of 10-μm-Long Single-Walled Carbon Nanotubes in Aqueous Solution. *Adv. Mater.* **2019**, 1901641.
66. Khripin, C. Y.; Tu, X.; Heddleston, J. M.; Silvera-Batista, C.; Hight Walker, A. R.; Fagan, J.; Zheng, M., High-resolution length fractionation of surfactant-dispersed carbon nanotubes. *Anal. Chem.* **2013,** *85* (3), 1382-1388.
67. Fagan, J. A.; Becker, M. L.; Chun, J.; Hobbie, E. K., Length fractionation of carbon nanotubes using centrifugation. *Adv. Mater.* **2008,** *20* (9), 1609-1613.
68. Fagan, J. A.; Becker, M. L.; Chun, J.; Nie, P.; Bauer, B. J.; Simpson, J. R.; Hight-Walker, A.; Hobbie, E. K., Centrifugal length separation of carbon nanotubes. *Langmuir* **2008,** *24* (24), 13880-13889.
69. Ohmori, S.; Saito, T.; Shukla, B.; Yumura, M.; Iijima, S., Fractionation of single wall carbon nanotubes by length using cross flow filtration method. *ACS Nano* **2010,** *4* (7), 3606-3610.
70. Gui, H.; Chen, H.; Khripin, C. Y.; Liu, B.; Fagan, J. A.; Zhou, C.; Zheng, M., A facile and low-cost length sorting of single-wall carbon nanotubes by precipitation and applications for thin-film transistors. *Nanoscale* **2016,** *8* (6), 3467-3473.
71. Miyata, Y.; Shiozawa, K.; Asada, Y.; Ohno, Y.; Kitaura, R.; Mizutani, T.; Shinohara, H., Length-sorted semiconducting carbon nanotubes for high-mobility thin film transistors. *Nano Res.* **2011,** *4* (10), 963-970.
72. Allard, S.; Forster, M.; Souharce, B.; Thiem, H.; Scherf, U., Organic semiconductors for solution-processable field-effect transistors (OFETs). *Angew. Chemie.* **2008,** *47* (22), 4070-4098.
73. Sun, Y.; Rogers, J. A., Inorganic semiconductors for flexible electronics. *Adv. Mater.* **2007,** *19* (15), 1897-1916.
74. Franklin, A. D., Nanomaterials in transistors: From high-performance to thin-film applications. *Science* **2015,** *349* (6249), aab2750.
75. Street, R. A., Thin-film transistors. *Adv. Mater.* **2009,** *21* (20), 2007-2022.
76. Tsentalovich, D. E.; Ma, A. W.; Lee, J. A.; Behabtu, N.; Bengio, E. A.; Choi, A.; Hao, J.; Luo, Y.; Headrick, R. J.; Green, M. J., Relationship of extensional viscosity and liquid crystalline transition to length distribution in carbon nanotube solutions. *Macromolecules* **2016,** *49* (2), 681-689.
77. He, X.; Gao, W.; Xie, L.; Li, B.; Zhang, Q.; Lei, S.; Robinson, J. M.; Hároz, E. H.; Doorn, S. K.; Wang, W., Wafer-scale monodomain films of spontaneously aligned single-walled carbon nanotubes. *Nat. Nanotechnol.* **2016,** *11* (7), 633.
78. Hu, H.; Zhao, B.; Itkis, M. E.; Haddon, R. C., Nitric acid purification of single-walled carbon nanotubes. *J. Phys. Chem. B* **2003,** *107* (50), 13838-13842.
79. Tchoul, M. N.; Ford, W. T.; Lolli, G.; Resasco, D. E.; Arepalli, S., Effect of mild nitric acid oxidation on dispersability, size, and structure of single-walled carbon nanotubes. *Chem. Mater.* **2007,** *19* (23), 5765-5772.

80. Karousis, N.; Tagmatarchis, N.; Tasis, D., Current progress on the chemical modification of carbon nanotubes. *Chem. Rev.* **2010,** *110* (9), 5366-5397.
81. Ziegler, K. J.; Gu, Z.; Peng, H.; Flor, E. L.; Hauge, R. H.; Smalley, R. E., Controlled oxidative cutting of single-walled carbon nanotubes. *J. Am. Chem. Soc.* **2005,** *127* (5), 1541-1547.
82. Parra-Vasquez, A. N. G.; Behabtu, N.; Green, M. J.; Pint, C. L.; Young, C. C.; Schmidt, J.; Kesselman, E.; Goyal, A.; Ajayan, P. M.; Cohen, Y., Spontaneous dissolution of ultralong single-and multiwalled carbon nanotubes. *ACS Nano* **2010,** *4* (7), 3969-3978.
83. Onsager, L., The effects of shape on the interaction of colloidal particles. *Annals of the New York Academy of Sciences* **1949,** *51* (4), 627-659.
84. Flory, P. J., Phase equilibria in solutions of rod-like particles. *Proceedings of the Royal Society of London. Series A. Mathematical and Physical Sciences* **1956,** *234* (1196), 73-89.
85. Wensink, H.; Vroege, G., Isotropic–nematic phase behavior of length-polydisperse hard rods. *J. Chem. Phys.* **2003,** *119* (13), 6868-6882.
86. Green, M. J.; Parra-Vasquez, A. N. G.; Behabtu, N.; Pasquali, M., Modeling the phase behavior of polydisperse rigid rods with attractive interactions with applications to single-walled carbon nanotubes in superacids. *J. Chem. Phys.* **2009,** *131* (8), 084901.
87. Chortos, A.; Pochorovski, I.; Lin, P.; Pitner, G.; Yan, X.; Gao, T. Z.; To, J. W.; Lei, T.; Will III, J. W.; Wong, H.-S. P., Universal Selective Dispersion of Semiconducting Carbon Nanotubes from Commercial Sources Using a Supramolecular Polymer. *ACS Nano* **2017,** *11* (6), 5660-5669.
88. Sangwan, V. K.; Ortiz, R. P.; Alaboson, J. M.; Emery, J. D.; Bedzyk, M. J.; Lauhon, L. J.; Marks, T. J.; Hersam, M. C., Fundamental performance limits of carbon nanotube thin-film transistors achieved using hybrid molecular dielectrics. *ACS Nano* **2012,** *6* (8), 7480-7488.
89. Zhang, L.; Tu, X.; Welsher, K.; Wang, X.; Zheng, M.; Dai, H., Optical characterizations and electronic devices of nearly pure (10, 5) single-walled carbon nanotubes. *J. Am. Chem. Soc.* **2009,** *131* (7), 2454-2455.
90. Wang, P.; Peng, Z.; Li, M.; Wang, Y., Stretchable Transparent Conductive Films from Long Carbon Nanotube Metals. *Small* **2018,** *14* (38), 1802625.
91. Rogers, J. A.; Someya, T.; Huang, Y., Materials and Mechanics for Stretchable Electronics. *Science* **2010,** *327* (5973), 1603-1607.
92. Lipomi, D. J.; Vosgueritchian, M.; Tee, B. C.; Hellstrom, S. L.; Lee, J. A.; Fox, C. H.; Bao, Z., Skin-like pressure and strain sensors based on transparent elastic films of carbon nanotubes. *Nat. Nanotechnol.* **2011,** *6* (12), 788.
93. Dowling, J., Current and future prospects for optoelectronic retinal prostheses. *Eye* **2009,** *23* (10), 1999.
94. Kuzum, D.; Takano, H.; Shim, E.; Reed, J. C.; Juul, H.; Richardson, A. G.; De Vries, J.; Bink, H.; Dichter, M. A.; Lucas, T. H., Transparent and flexible low noise graphene electrodes for simultaneous electrophysiology and neuroimaging. *Nat. Commun.* **2014,** *5*, 5259.

95. Wang, Y.; Zhu, C.; Pfattner, R.; Yan, H.; Jin, L.; Chen, S.; Molina-Lopez, F.; Lissel, F.; Liu, J.; Rabiah, N. I., A highly stretchable, transparent, and conductive polymer. *Sci. Adv.* **2017,** *3* (3), e1602076.
96. Liu, Y.; Zhang, J.; Gao, H.; Wang, Y.; Liu, Q.; Huang, S.; Guo, C. F.; Ren, Z., Capillary-force-induced cold welding in silver-nanowire-based flexible transparent electrodes. *Nano Lett.* **2017,** *17* (2), 1090-1096.
97. Preston, C.; Fang, Z.; Murray, J.; Zhu, H.; Dai, J.; Munday, J. N.; Hu, L., Silver nanowire transparent conducting paper-based electrode with high optical haze. *J. Mater. Chem. C* **2014,** *2* (7), 1248-1254.
98. Bae, S.-H.; Lee, Y.; Sharma, B. K.; Lee, H.-J.; Kim, J.-H.; Ahn, J.-H., Graphene-based transparent strain sensor. *Carbon* **2013,** *51*, 236-242.
99. Liu, N.; Chortos, A.; Lei, T.; Jin, L.; Kim, T. R.; Bae, W.-G.; Zhu, C.; Wang, S.; Pfattner, R.; Chen, X., Ultratransparent and stretchable graphene electrodes. *Sci. Adv.* **2017,** *3* (9), e1700159.
100. Li, Z.; Kandel, H. R.; Dervishi, E.; Saini, V.; Biris, A. S.; Biris, A. R.; Lupu, D., Does the wall number of carbon nanotubes matter as conductive transparent material? *Appl. Phys. Lett* **2007,** *91* (5), 053115.
101. Chen, G.; Futaba, D. N.; Sakurai, S.; Yumura, M.; Hata, K., Interplay of wall number and diameter on the electrical conductivity of carbon nanotube thin films. *Carbon* **2014,** *67*, 318-325.
102. Green, A. A.; Hersam, M. C., Processing and properties of highly enriched double-wall carbon nanotubes. *Nat. Nanotechnol.* **2009,** *4* (1), 64-70.
103. Wu, H.; Kong, D.; Ruan, Z.; Hsu, P.-C.; Wang, S.; Yu, Z.; Carney, T. J.; Hu, L.; Fan, S.; Cui, Y., A transparent electrode based on a metal nanotrough network. *Nat. Nanotechnol.* **2013,** *8* (6), 421.
104. Hu, W.; Wang, R.; Lu, Y.; Pei, Q., An elastomeric transparent composite electrode based on copper nanowires and polyurethane. *J. Mater. Chem. C* **2014,** *2* (7), 1298-1305.
105. Lipomi, D. J.; Tee, B. C. K.; Vosgueritchian, M.; Bao, Z., Stretchable organic solar cells. *Adv. Mater.* **2011,** *23* (15), 1771-1775.
106. Cheng, Y.; Wang, S.; Wang, R.; Sun, J.; Gao, L., Copper nanowire based transparent conductive films with high stability and superior stretchability. *J. Mater. Chem. C* **2014,** *2* (27), 5309-5316.
107. Zhang, Y.; Sheehan, C. J.; Zhai, J.; Zou, G.; Luo, H.; Xiong, J.; Zhu, Y.; Jia, Q., Polymer-embedded carbon nanotube ribbons for stretchable conductors. *Adv. Mater.* **2010,** *22* (28), 3027-3031.
108. Chun, K.-Y.; Oh, Y.; Rho, J.; Ahn, J.-H.; Kim, Y.-J.; Choi, H. R.; Baik, S., Highly conductive, printable and stretchable composite films of carbon nanotubes and silver. *Nat. Nanotechnol.* **2010,** *5* (12), 853.
109. Matsuhisa, N.; Inoue, D.; Zalar, P.; Jin, H.; Matsuba, Y.; Itoh, A.; Yokota, T.; Hashizume, D.; Someya, T., Printable elastic conductors by in situ formation of silver nanoparticles from silver flakes. *Nat. Mater.* **2017,** *16* (8), 834.
110. Yamada, T.; Hayamizu, Y.; Yamamoto, Y.; Yomogida, Y.; Izadi-Najafabadi, A.; Futaba, D. N.; Hata, K., A stretchable carbon nanotube strain sensor for human-motion detection. *Nat. Nanotechnol.* **2011,** *6* (5), 296.

111. Burt, R.; Birkett, G.; Zhao, X. S., A review of molecular modelling of electric double layer capacitors. *Physical Chemistry Chemical Physics* **2014,** *16* (14), 6519-6538.
112. Parsons, R., The electrical double layer: recent experimental and theoretical developments. *Chem. Rev.* **1990,** *90* (5), 813-826.
113. Fedorov, M. V.; Kornyshev, A. A., Ionic Liquids at Electrified Interfaces. *Chem. Rev.* **2014,** *114* (5), 2978-3036.
114. Helmholtz, H., Studien über electrische Grenzschichten. *Annalen der Physik* **1879,** *243* (7), 337-382.
115. Chapman, D. L., LI. A contribution to the theory of electrocapillarity. *The London, Edinburgh, and Dublin Philosophical Magazine and Journal of Science* **1913,** *25* (148), 475-481.
116. Gouy, M. M., Sur la constitution de la charge électrique à la surface d'un électrolyte. *Journal de physique théorique et appliquée* **1910,** *9* (1), 457.
117. Zure., Theorie der elektrolytischen doppelschicht. *Zeitschrift für Elektrochemie und angewandte physikalische Chemie : herausgegeben von der Deutsche Bunsen-Gesellschaft für Angewandte* **1924,** *30* (21), 508-516.
118. Lewandowski, A.; Świderska-Mocek, A., Ionic liquids as electrolytes for Li-ion batteries—an overview of electrochemical studies. *J. Power Sources* **2009,** *194* (2), 601-609.
119. Xu, K., Electrolytes and interphases in Li-ion batteries and beyond. *Chem. Rev.* **2014,** *114* (23), 11503-11618.
120. Parsons, R., The electrical double layer: recent experimental and theoretical developments. *Chem. Rev.* **1990,** *90* (5), 813-826.
121. Bazant, M. Z.; Storey, B. D.; Kornyshev, A. A., Double layer in ionic liquids: Overscreening versus crowding. *Phys. Rev. Lett.* **2011,** *106* (4), 046102.
122. Vatamanu, J.; Borodin, O.; Smith, G. D., Molecular Insights into the Potential and Temperature Dependences of the Differential Capacitance of a Room-Temperature Ionic Liquid at Graphite Electrodes. *J. Am. Chem. Soc.* **2010,** *132* (42), 14825-14833.
123. Lockett, V.; Sedev, R.; Ralston, J.; Horne, M.; Rodopoulos, T., Differential capacitance of the electrical double layer in imidazolium-based ionic liquids: influence of potential, cation size, and temperature. *J. Phys. Chem. C* **2008,** *112* (19), 7486-7495.
124. Hayes, R.; Borisenko, N.; Tam, M. K.; Howlett, P. C.; Endres, F.; Atkin, R., Double layer structure of ionic liquids at the Au (111) electrode interface: an atomic force microscopy investigation. *J. Phys. Chem. C* **2011,** *115* (14), 6855-6863.
125. van der Heide, P.; Heide, P. V. D., *X-ray Photoelectron Spectroscopy : An introduction to Principles and Practices*. Wiley: 2011.
126. Axnanda, S.; Crumlin, E. J.; Mao, B.; Rani, S.; Chang, R.; Karlsson, P. G.; Edwards, M. O. M.; Lundqvist, M.; Moberg, R.; Ross, P.*, et al.*, Using "Tender" X-ray Ambient Pressure X-Ray Photoelectron Spectroscopy as A Direct Probe of Solid-Liquid Interface. *Sci. Rep.* **2015,** *5*, 9788.
127. Favaro, M.; Jeong, B.; Ross, P. N.; Yano, J.; Hussain, Z.; Liu, Z.; Crumlin, E. J., Unravelling the electrochemical double layer by direct probing of the solid/liquid interface. *Nat. Commun.* **2016,** *7*, 12695.

128. Geim, A. K.; Novoselov, K. S., The rise of graphene. *Nat. Mater.* **2007,** *6*, 183.
129. Allen, M. J.; Tung, V. C.; Kaner, R. B., Honeycomb Carbon: A Review of Graphene. *Chem. Rev.* **2010,** *110* (1), 132-145.
130. Nemsak, S.; Strelcov, E.; Duchoň, T. s.; Guo, H.; Hackl, J.; Yulaev, A.; Vlassiouk, I.; Mueller, D. N.; Schneider, C. M.; Kolmakov, A., Interfacial electrochemistry in liquids probed with photoemission electron microscopy. *J. Am. Chem. Soc.* **2017,** *139* (50), 18138-18141.
131. Guo, H.; Strelcov, E.; Yulaev, A.; Wang, J.; Appathurai, N.; Urquhart, S.; Vinson, J.; Sahu, S.; Zwolak, M.; Kolmakov, A., Enabling photoemission electron microscopy in liquids via graphene-capped microchannel arrays. *Nano Lett.* **2017,** *17* (2), 1034-1041.
132. Velasco-Velez, J. J.; Pfeifer, V.; Hävecker, M.; Weatherup, R. S.; Arrigo, R.; Chuang, C. H.; Stotz, E.; Weinberg, G.; Salmeron, M.; Schlögl, R., Photoelectron spectroscopy at the graphene–liquid interface reveals the electronic structure of an electrodeposited cobalt/graphene electrocatalyst. *Angew. Chemie.* **2015,** *54* (48), 14554-14558.
133. Kolmakov, A.; Dikin, D. A.; Cote, L. J.; Huang, J.; Abyaneh, M. K.; Amati, M.; Gregoratti, L.; Günther, S.; Kiskinova, M., Graphene oxide windows for in situ environmental cell photoelectron spectroscopy. *Nat. Nanotechnol.* **2011,** *6* (10), 651.
134. Weatherup, R. S.; Eren, B.; Hao, Y.; Bluhm, H.; Salmeron, M. B., Graphene membranes for atmospheric pressure photoelectron spectroscopy. *J. Phys. Chem. Lett.* **2016,** *7* (9), 1622-1627.
135. Velasco-Velez, J. J.; Pfeifer, V.; Hävecker, M.; Weatherup, R. S.; Arrigo, R.; Chuang, C.-H.; Stotz, E.; Weinberg, G.; Salmeron, M.; Schlögl, R.*, et al.*, Photoelectron Spectroscopy at the Graphene–Liquid Interface Reveals the Electronic Structure of an Electrodeposited Cobalt/Graphene Electrocatalyst. *Angew. Chemie.* **2015,** *54* (48), 14554-14558.
136. Kolmakov, A.; Dikin, D. A.; Cote, L. J.; Huang, J.; Abyaneh, M. K.; Amati, M.; Gregoratti, L.; Günther, S.; Kiskinova, M., Graphene oxide windows for in situ environmental cell photoelectron spectroscopy. *Nat. Nanotechnol.* **2011,** *6*, 651.
137. Li, X.; Cai, W.; An, J.; Kim, S.; Nah, J.; Yang, D.; Piner, R.; Velamakanni, A.; Jung, I.; Tutuc, E.*, et al.*, Large-Area Synthesis of High-Quality and Uniform Graphene Films on Copper Foils. *Science* **2009,** *324* (5932), 1312.
138. Chen, Y.-M.; He, S.-M.; Huang, C.-H.; Huang, C.-C.; Shih, W.-P.; Chu, C.-L.; Kong, J.; Li, J.; Su, C.-Y., Ultra-large suspended graphene as a highly elastic membrane for capacitive pressure sensors. *Nanoscale* **2016,** *8* (6), 3555-3564.
139. Zhang, J.; Lin, L.; Sun, L.; Huang, Y.; Koh, A. L.; Dang, W.; Yin, J.; Wang, M.; Tan, C.; Li, T.*, et al.*, Clean Transfer of Large Graphene Single Crystals for High-Intactness Suspended Membranes and Liquid Cells. *Adv. Mater.* **2017,** *29* (26), 1700639.
140. Yang, D.-Q.; Sacher, E., Carbon 1s X-ray Photoemission Line Shape Analysis of Highly Oriented Pyrolytic Graphite: The Influence of Structural Damage on Peak Asymmetry. *Langmuir* **2006,** *22* (3), 860-862.

141. Phillips, J. C.; Braun, R.; Wang, W.; Gumbart, J.; Tajkhorshid, E.; Villa, E.; Chipot, C.; Skeel, R. D.; Kalé, L.; Schulten, K., Scalable molecular dynamics with NAMD. *J. Comput. Chem.* **2005,** *26* (16), 1781-1802.
142. Humphrey, W.; Dalke, A.; Schulten, K., VMD: Visual molecular dynamics. *J. Mol. Graph* **1996,** *14* (1), 33-38.
143. Mayne, C. G.; Saam, J.; Schulten, K.; Tajkhorshid, E.; Gumbart, J. C., Rapid parameterization of small molecules using the force field toolkit. *J. Comput. Chem.* **2013,** *34* (32), 2757-2770.
144. Frisch, M. J. T., G. W.; Schlegel, H. B.; Scuseria, G. E.; Robb, M. A.; Cheeseman, J. R. ; Scalmani, G.; Barone, V.; Mennucci, B.; Petersson, G. A.; et al., *Gaussian 09;* , Gaussian, Inc.: Wallingford, CT, USA, 2009.
145. Martínez, L.; Andrade, R.; Birgin, E. G.; Martínez, J. M., PACKMOL: A package for building initial configurations for molecular dynamics simulations. *J. Comput. Chem.* **2009,** *30* (13), 2157-2164.
146. Yan, Z.; Peng, Z.; Casillas, G.; Lin, J.; Xiang, C.; Zhou, H.; Yang, Y.; Ruan, G.; Raji, A.-R. O.; Samuel, E. L. G.*, et al.*, Rebar Graphene. *ACS Nano* **2014,** *8* (5), 5061-5068.
147. Ramesh, S.; Ericson, L. M.; Davis, V. A.; Saini, R. K.; Kittrell, C.; Pasquali, M.; Billups, W. E.; Adams, W. W.; Hauge, R. H.; Smalley, R. E., Dissolution of Pristine Single Walled Carbon Nanotubes in Superacids by Direct Protonation. *J. Phys. Chem. B* **2004,** *108* (26), 8794-8798.
148. Davis, V. A.; Parra-Vasquez, A. N. G.; Green, M. J.; Rai, P. K.; Behabtu, N.; Prieto, V.; Booker, R. D.; Schmidt, J.; Kesselman, E.; Zhou, W.*, et al.*, True solutions of single-walled carbon nanotubes for assembly into macroscopic materials. *Nat. Nanotechnol.* **2009,** *4*, 830.
149. Behabtu, N.; Lomeda, J. R.; Green, M. J.; Higginbotham, A. L.; Sinitskii, A.; Kosynkin, D. V.; Tsentalovich, D.; Parra-Vasquez, A. N. G.; Schmidt, J.; Kesselman, E.*, et al.*, Spontaneous high-concentration dispersions and liquid crystals of graphene. *Nat. Nanotechnol.* **2010,** *5*, 406.
150. Nair, R. R.; Blake, P.; Grigorenko, A. N.; Novoselov, K. S.; Booth, T. J.; Stauber, T.; Peres, N. M. R.; Geim, A. K., Fine Structure Constant Defines Visual Transparency of Graphene. *Science* **2008,** *320* (5881), 1308.
151. Ni, Z. H.; Wang, H. M.; Kasim, J.; Fan, H. M.; Yu, T.; Wu, Y. H.; Feng, Y. P.; Shen, Z. X., Graphene Thickness Determination Using Reflection and Contrast Spectroscopy. *Nano Lett.* **2007,** *7* (9), 2758-2763.
152. Suk, J. W.; Kitt, A.; Magnuson, C. W.; Hao, Y.; Ahmed, S.; An, J.; Swan, A. K.; Goldberg, B. B.; Ruoff, R. S., Transfer of CVD-Grown Monolayer Graphene onto Arbitrary Substrates. *ACS Nano* **2011,** *5* (9), 6916-6924.
153. Zhang, J.; Lin, L.; Sun, L.; Huang, Y.; Koh, A. L.; Dang, W.; Yin, J.; Wang, M.; Tan, C.; Li, T.*, et al.*, Clean Transfer of Large Graphene Single Crystals for High-Intactness Suspended Membranes and Liquid Cells. *Adv. Mater.* **2017,** *29* (26), 1700639.
154. Zhang, C.; Grass, M. E.; McDaniel, A. H.; DeCaluwe, S. C.; Gabaly, F. E.; Liu, Z.; McCarty, K. F.; Farrow, R. L.; Linne, M. A.; Hussain, Z.*, et al.*, Measuring fundamental properties in operating solid oxide electrochemical cells by using in situ X-ray photoelectron spectroscopy. *Nat. Mater.* **2010,** *9*, 944.

155. Hayes, R.; Borisenko, N.; Tam, M. K.; Howlett, P. C.; Endres, F.; Atkin, R., Double Layer Structure of Ionic Liquids at the Au(111) Electrode Interface: An Atomic Force Microscopy Investigation. *J. Phys. Chem. C* **2011,** *115* (14), 6855-6863.
156. Luo, H.-B.; Wang, P.; Wu, X.; Qu, H.; Ren, X.; Wang, Y., A One-Pot, Large-Scale Synthesis of Organic Color Center-Tailored Semiconducting Carbon Nanotubes. *ACS Nano* **2019**.
157. Piao, Y.; Meany, B.; Powell, L. R.; Valley, N.; Kwon, H.; Schatz, G. C.; Wang, Y., Brightening of carbon nanotube photoluminescence through the incorporation of sp3 defects. *Nat. Chem.* **2013,** *5*, 840.
158. He, X.; Gifford, B. J.; Hartmann, N. F.; Ihly, R.; Ma, X.; Kilina, S. V.; Luo, Y.; Shayan, K.; Strauf, S.; Blackburn, J. L.*, et al.*, Low-Temperature Single Carbon Nanotube Spectroscopy of sp3 Quantum Defects. *ACS Nano* **2017,** *11* (11), 10785-10796.
159. Shiraki, T.; Uchimura, S.; Shiraishi, T.; Onitsuka, H.; Nakashima, N., Near infrared photoluminescence modulation by defect site design using aryl isomers in locally functionalized single-walled carbon nanotubes. *Chem. Comm.* **2017,** *53* (93), 12544-12547.
160. Miyauchi, Y.; Iwamura, M.; Mouri, S.; Kawazoe, T.; Ohtsu, M.; Matsuda, K., Brightening of excitons in carbon nanotubes on dimensionality modification. *Nat. Photonics* **2013,** *7*, 715.
161. Wu, X.; Kim, M.; Kwon, H.; Wang, Y., Photochemical Creation of Fluorescent Quantum Defects in Semiconducting Carbon Nanotube Hosts. *Angewandte Chemie* **2018,** *130* (3), 656-661.
162. Kwon, H.; Furmanchuk, A. o.; Kim, M.; Meany, B.; Guo, Y.; Schatz, G. C.; Wang, Y., Molecularly Tunable Fluorescent Quantum Defects. *J. Am. Chem. Soc.* **2016,** *138* (21), 6878-6885.
163. He, X.; Hartmann, N. F.; Ma, X.; Kim, Y.; Ihly, R.; Blackburn, J. L.; Gao, W.; Kono, J.; Yomogida, Y.; Hirano, A.*, et al.*, Tunable room-temperature single-photon emission at telecom wavelengths from sp3 defects in carbon nanotubes. *Nat. Photonics* **2017,** *11*, 577.
164. Saha, A.; Gifford, B. J.; He, X.; Ao, G.; Zheng, M.; Kataura, H.; Htoon, H.; Kilina, S.; Tretiak, S.; Doorn, S. K., Narrow-band single-photon emission through selective aryl functionalization of zigzag carbon nanotubes. *Nat. Chem.* **2018,** *10* (11), 1089-1095.
165. Kwon, H.; Kim, M.; Meany, B.; Piao, Y.; Powell, L. R.; Wang, Y., Optical Probing of Local pH and Temperature in Complex Fluids with Covalently Functionalized, Semiconducting Carbon Nanotubes. *J. Phys. Chem. C* **2015,** *119* (7), 3733-3739.
166. Yildirimer, L.; Thanh, N. T.; Loizidou, M.; Seifalian, A. M., Toxicology and clinical potential of nanoparticles. *Nano Today* **2011,** *6* (6), 585-607.
167. Kwon, H. J.; Shin, K.; Soh, M.; Chang, H.; Kim, J.; Lee, J.; Ko, G.; Kim, B. H.; Kim, D.; Hyeon, T., Large-Scale Synthesis and Medical Applications of Uniform-Sized Metal Oxide Nanoparticles. *Adv. Mater.* **2018,** *30* (42), 1704290.
168. Efficient Isolation and Solubilization of Pristine SingleWalled Nanotubes in Bile Salt Micelles. *Adv. Funct. Mater.* **2004,** *14* (11), 1105-1112.

169. Islam, M. F.; Rojas, E.; Bergey, D. M.; Johnson, A. T.; Yodh, A. G., High Weight Fraction Surfactant Solubilization of Single-Wall Carbon Nanotubes in Water. *Nano Lett.* **2003,** *3* (2), 269-273.
170. Welsher, K.; Liu, Z.; Sherlock, S. P.; Robinson, J. T.; Chen, Z.; Daranciang, D.; Dai, H., A route to brightly fluorescent carbon nanotubes for near-infrared imaging in mice. *Nat. Nanotechnol.* **2009,** *4*, 773.
171. Aharonovich, I.; Englund, D.; Toth, M., Solid-state single-photon emitters. *Nat. Photonics* **2016,** *10*, 631.